

Recent Progress in Materials and Device Design for Semitransparent Photovoltaic Technologies

Pankaj Kumar,* Shujie You, and Alberto Vomiero*

Semitransparent photovoltaic (STPV) solar cells offer an immense opportunity to expand the scope of photovoltaics to special applications such as windows, facades, skylights, and so on. These new opportunities have encouraged researchers to develop STPVs using traditional thin-film solar cell technologies (amorphous-Si, CdTe, and CIGS or emerging solar cells (organic, perovskites, and dye-sensitized). There are considerable improvements in both power conversion efficiency (PCE) and semitransparency of these STPV devices. This review studies the device structure of state-of-the-art STPV devices and thereby analyzes the different approaches toward maximizing the product of PCE and average visible transmittance. The origins of PCE losses during the opaque-to-semitransparent transition in the different STPV technologies are discussed. In addition, critical practical aspects relevant to all STPV devices, such as compatibility of the top transparent electrode with the device structure, buffer layer optimization, light management engineering, scale-up, and stability, are also reported. This overview is expected to facilitate researchers across different technologies to identify and overcome the challenges toward achieving higher light utilization efficiencies in STPVs.

1. Introduction

Photovoltaics offer a clean and renewable alternative to fossil-based sources of electricity. It will continue to increase its share in global electricity production because of increased concerns about global warming and environmental pollution.^[1,2] Lab-level efficiencies of various solar cell technologies have improved considerably in the last few years with record power conversion efficiencies (PCEs) of 26.7% for mono-crystalline silicon,^[3] 24.4% for

multi-crystalline silicon,^[4] 10.3% for hydrogenated amorphous silicon (a-Si:H),^[5] 23.6% for Cu(In,Ga)Se₂ (CIGS),^[6] 22.3% for CdTe,^[6] 26.0% for perovskite solar cells (PSCs),^[6] 19.3% for organic solar cells (OSCs),^[7] and 14.2% for dye-sensitized solar cells (DSSCs).^[8] Currently, the well-established silicon-based PV occupies up to 95% of the total commercial production, which implies an opportunity to improve alternative PV technologies.^[9]

Commercial and residential buildings consume about 40% of total global energy production.^[1,10–13] Traditionally, opaque solar panels have been installed on limited areas of roof-tops and parking shades, generally categorized into “building-attached photovoltaics” (BAPV).^[13,14] As the number of skyscrapers is expected to rise continually, the windows, facades, and skylights will provide even larger unclaimed areas for solar


panel installations. However, opaque solar panels with rigid designs applied in BAPVs are generally not aesthetically attractive. On the other hand, semitransparent photovoltaics (STPVs) can potentially replace the glass windows/glazing systems, in addition to application in currently unexplored areas like awnings, curtain walls, ventilated/non-ventilated facades, canopies, and skylight sunroofs, greenhouses, windows of vehicles, and so on. These applications are categorized into “building-integrated photovoltaic” (BIPV) technologies.^[13] Apart from producing electricity, thermal insulation by reducing incident heat load and transparency modulation are additional features of emerging STPV technologies embedded in glass windows.^[15–17] The global BIPV market size was estimated at \$14.4 billion in 2020 and is expected to have a compound annual growth rate of 20.0% from 2021 to 2028 to reach \$59.5 billion by 2028.^[17]

Although BIPVs have been installed on commercial buildings to some extent, their widespread application is still missing.^[1,13,18] Among the many solar cell technologies suitable for STPV applications (such as CIGS, CdTe, DSSC, a-Si:H, PSCs, and OSCs), only a-Si:H has been commercialized with limited success.^[19] The limiting factors are many: cost, low efficiency, insufficient proven stability, lack of aesthetic appeal and awareness, and so on.^[13,20,21]

Transparency is one of the most critical factors for BIPV applications such as windows, skylights, and glass curtain walls. A simple method to assess the transparency of a solar cell is to

P. Kumar, S. You, A. Vomiero
Division of Materials Science
Department of Engineering Sciences and Mathematics
Luleå University of Technology
Luleå SE-971 87, Sweden
E-mail: pankaj.kumar@ltu.se; alberto.vomiero@ltu.se

A. Vomiero
Department of Molecular Sciences and Nanosystems
Ca' Foscari University of Venice
Via Torino 155, Venezia 30172, Mestre, Italy

 The ORCID identification number(s) for the author(s) of this article can be found under <https://doi.org/10.1002/aenm.202301555>

© 2023 The Authors. Advanced Energy Materials published by Wiley-VCH GmbH. This is an open access article under the terms of the Creative Commons Attribution License, which permits use, distribution and reproduction in any medium, provided the original work is properly cited.

DOI: 10.1002/aenm.202301555

calculate the average transmittance values in the visible range (usually taken as 380–740 nm). However, our visual perception (eye sensitivity) of light differs across the visible spectrum wavelengths. A parameter called average visible transmittance (AVT) was introduced to take eye sensitivity to different wavelengths into consideration. It is calculated as the average spectral transmittance of light in the visible wavelength weighted by the photopic response of a human eye and calculated using^[22,23]:

$$AVT = \frac{\int T(\lambda) \cdot V(\lambda) \cdot AM1.5G(\lambda) d\lambda}{\int V(\lambda) \cdot AM1.5G(\lambda) d\lambda} \quad (1)$$

where $T(\lambda)$ is the transmission spectrum and $V(\lambda)$ is the photopic response function. AM1.5G represents the global standard solar spectrum. The integration is performed in a sufficient wavelength range (or at least 380–740 nm). It is highly recommended to use Equation (1) to maintain consistency in reporting transparency of an STPV device. AVT is sometimes also called average photopic response (APT). AVT in residential windows can vary anywhere from 15% for highly tinted glasses up to 90% for clear glass.^[23] It is generally accepted that an AVT of >25% is required for window application.^[24]

PCE and AVT are usually inversely related, and therefore, a single compound parameter was necessary to reference the improvements across various STPV technologies. A new performance metric called light utilization efficiency (LUE) was introduced by Traverse et al.^[23]

$$LUE = PCE \times AVT \quad (2)$$

LUE allows an effective way to compare different STPV technologies against the theoretical limit of 20.6% for single junction and 37% for multi-junction STPVs.^[25]

Most of the STPV devices are not color-neutral since the spectral transmittance in the visible wavelength region is not uniform. Therefore, apart from PCE and transmittance, the color perception (aesthetics) of semitransparent solar cells is another parameter to consider when targeting BIPV applications such as glass windows. The International Lighting Commission (CIE) 1931 (x, y) chromaticity diagram is the industry standard used to quantify the color perceived by the human eye from a measured spectrum.^[26] The so-called “white point” or neutral color corresponds to the coordinates of (0.3333, 0.3333), and the standard solar spectrum used to characterize the PCE (AM 1.5G) has the color coordinates of (0.3202, 0.3324).^[27,28] Alternatively, chromaticity coordinates can be reported using CIE Lab color space, with three parameters a^* , b^* , and L .^[23,29] Moreover, aesthetics and color comfort are also important. Therefore, the additional figures of merit, such as color rendering index (CRI) and correlated color temperature (CCT), are evaluated.^[30] A high CRI value (close to 100) means little deviation of the color of the light transmitted through the solar cells versus the original reference light.^[31] At the same time, color temperature is a measure of bluish (cool) or yellowish (warm) appearance: cool color has a color temperature above 5000 K while the warm colors hold a temperature of 2700–3000 K.^[32]

Several reviews comparing different technologies of STPVs have been published in recent years (2016–2022). Saifullah et al. (2016)^[33] focused on device structure and material requirements

for fabricating ST dye-sensitized-, amorphous silicon (a-Si:H)-, and chalcopyrite-based solar cells. Sun and Jasieniak (2017)^[34] highlighted the advances across the key solar cell technologies (amorphous silicon-, kesterite-, chalcopyrite-, CdTe-, dye-sensitized-, organic-, and perovskite-based systems) with potential for semi-transparent BIPV applications. They focused on BIPV requirements, an overview of different STPV technologies, and the corresponding benefits and drawbacks. Tai and Yan (2017)^[35] reviewed the device design of semitransparent organic photovoltaics (STOPVs), DSSCs, and PSCs, focusing primarily on the top transparent electrode materials. Traverse et al. (2017)^[23] summarized the development and performance limits of STPV technologies (including transparent solar cells, luminescent solar concentrators (LSCs), and scattering solar concentrators) and discussed the requirements to enable their widespread adoption in buildings, windows, electronic device displays, and automobiles. Chang et al. (2018)^[36] provided an overall perspective on developing STPVs based on polymer photovoltaics (OPVs) and their potential applications. Their focus was primarily on polymer donors, small molecule acceptors, and top electrode materials. Husain et al. (2018)^[37] reported the recent developments in all the STPV devices with AVT > 20%. They focused on the device structure, processes, and pros and cons of each of these STPV technologies. Shin and Choi (2018)^[38] reviewed progress in materials fabrication, design of cell structure, and device engineering/characterization of high-performance STPVs based on organic and perovskite solar cells. Xue et al. (2018)^[39] reviewed the material selection, optical engineering, and device architecture design for high-performance semitransparent OPVs and PSCs. Within the discussion of STOPV and STPSC devices and their performance, they commented on some essential attributes of transport layers and transparent top electrodes. Lee et al. (2020)^[40] focused on neutral-colored STPVs based on c-Si or LSCs and outlined the practical criteria for evaluating the non-Si STPV technologies. Dong et al. (2022)^[41] reviewed the progress of active layer materials, TTEs, and strategies for performance enhancement of STOPVs and STPSCs while discussing the respective challenges. Apart from these reviews comparing multiple STPV technologies (types), targeted reviews focusing on one specific technology (OPVs, PSCs, etc.) have also been published.

In the last decade, third-generation solar cells (DSSCs, PSCs, and OPVs) have attracted massive attention because of attributes such as lightness, low cost, and intrinsic flexibility.^[42] Parallely, thanks to their easy bandgap or absorption spectrum tunability, STPV devices with record-high LUEs have progressively been reported based on these. The conventional semitransparent thin film solar cells (based on a-Si, CdTe, or CIGS) have not seen a comparable relative improvement in LUEs. Still, their maturity would provide helpful guidance while developing third-generation STPVs. Overall, there is quite a scope for applying the progress made in one type of solar cell to the other. Therefore, the device structures and strategies employed in these key STPV technologies to improve the LUEs have been discussed. This is followed by a summary of the main transparent conductive electrodes (TCEs), various transport and buffer layers, and light management techniques. The issues facing scalability and stability (especially in third-generation solar cells) have also been highlighted. This comprehensive progress report would inspire cross-technology innovations in STPV research.

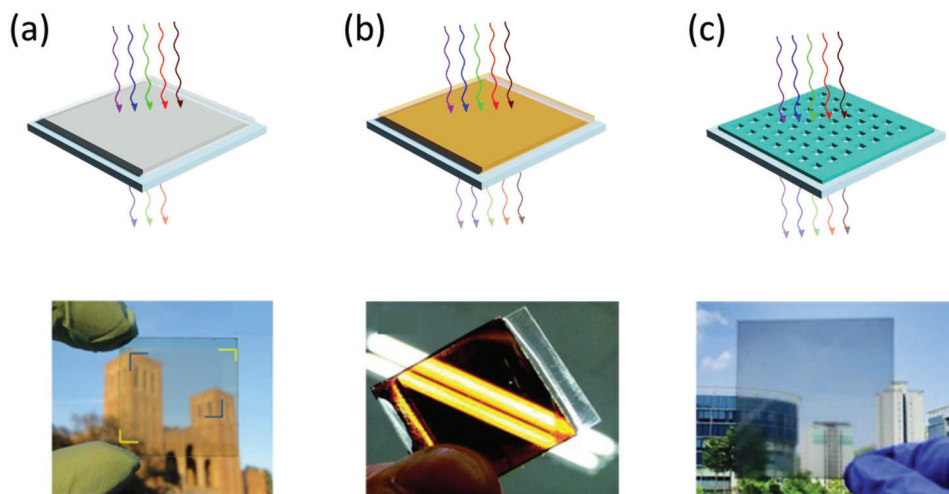


Figure 1. (Top row) Simplified schematic for types of semitransparent solar cells and (bottom row) photographs of corresponding solar cells reported in the literature. a) An organic semitransparent solar cell. Reproduced with permission.^[43] Copyright 2012, American Chemical Society. b) A perovskite solar cell. Reproduced with permission.^[44] Copyright 2015, Royal Society of Chemistry. c) A c-Si solar cell with through-hole transmission windows. Reproduced with permission.^[45] Copyright 2020, Elsevier.

2. Approaches toward STPVs

The device structures employed to achieve semitransparency can be categorized into three categories: (i) wavelength selective; (ii) non-wavelength selective; (iii) selective area transmission. Selecting a particular approach to achieve semitransparency determines the PCE, transparency, stability, color perception, and the overall cost of device fabrication.

2.1. Wavelength-Selective

Some absorber materials can be tuned to selectively absorb the wavelengths that do not fall in the visible region (Figure 1a).^[28,46–48] Wavelength selectivity can be utilized for an additional benefit, namely, the heat insulation function.^[49] In window applications, a solar cell can be applied to reflect the lower wavelength IR energy while absorbing UV and near-infrared spectrum (NIR) to keep the room temperature warm or cool depending on the way the reflector film is applied.^[49] Since wavelength-selective absorber material can selectively transmit visible light, it has the highest PCE retaining ratio (i.e., the ratio of PCE of STPV device vs PCE of the corresponding opaque device).^[50]

2.2. Non-Wavelength-Selective

These broadband absorbers rely on the trade-off between transparency and PCE; therefore, the efficiency decreases to 0% as AVT approaches 100%. Mature technologies like a-Si, CIGS, and CdTe solar cells can be thinned to hundreds of nanometers to achieve sufficient semitransparency (Figure 1b).

2.3. Selective Area Transmission

In selective area transmission (also referred to as aperture type or punch-through, or structurally transparent solar cell), some parts of the solar cells (without an absorber layer) let the light pass through. Thus, the transparency can be tuned by changing the relative area of holes versus the absorber layer (Figure 1c). In these solar cells, pass-through holes (in any desired pattern) are generally created using laser scribing^[51] or chemical etching.^[45] Alternatively, island-like shapes can be formed using controlled dewetting or nano-structuring methods.^[52–57] Laser scribing or etching processes are likely to damage the absorber layer, while the island design involves complicated fabrication processes to avoid shunting. Nevertheless, Kuk et al.^[51] have reported a promising optimized laser etching process in CIGS solar cells, thus inviting increased research toward this approach.

In terms of state-of-the-art, thinned-down versions of the already commercialized solar cell technologies such as CdTe (e.g., 12% to 6% PCE at 10% to 50% AVT with dimensions, 120 cm × 60 cm),^[58] and a-Si (e.g., PCE = 5.9%, AVT = 20% for 790 cm² module)^[59] have penetrated the STPV market. Wavelength-selective organic photovoltaics with tunable absorption spectrum has also been demonstrated in market-ready products—e.g., a PCE of 4.5% from 114.5 cm² module and AVT of ≈20% was demonstrated.^[60] On the other hand, selective area transmission-based semitransparent solar cell technologies are rare in the mainstream market, although some commercial silicon-based STPVs do exist, where semitransparency is achieved by leaving gaps between opaque cells (the cells are not inherently semitransparent). A crystalline silicon-based semitransparent PV module (≈2 m²) with 42% visible transmittance and 7% PCE was reported.^[61] They obtained transparency by dividing the traditional c-Si cells into strips and then reassembling them with the required gaps. Another commercially available c-Si-based

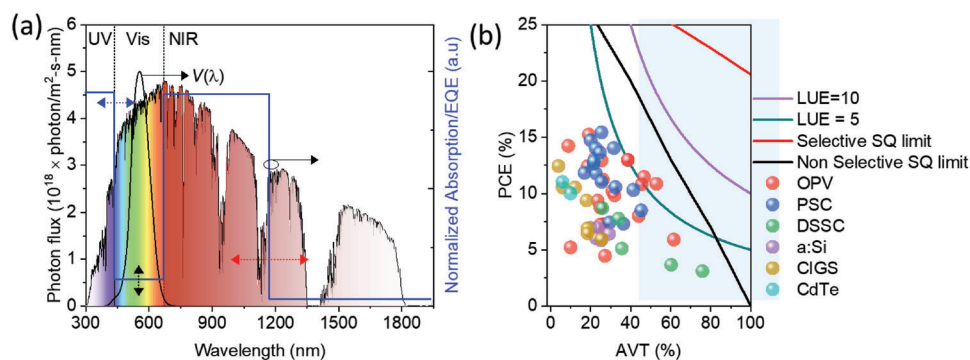


Figure 2. a) Solar photon flux for standard AM 1.5G irradiation (left axis) with the photopic response function (right axis) plotted versus wavelength. $V(\lambda)$ represents the photopic response function of the human eye. A wavelength-selective semitransparent device has peak absorption/external quantum efficiency (EQE) adjusted in the UV (blue arrows) and NIR (red arrows) portions of the spectrum, while the visible absorption can be tuned (black arrows) to achieve sufficient transparency. Integrated photon flux density: UV (300–435 nm) = 3.9%, vis (435–670 nm) = 22.6%, and NIR (670–3000 nm) = 73.5%. Vis region was selected corresponding to AVT > 99.5% and CRI > 95. b) The plot of the PCE versus AVT of some high LUE devices in recent literature (shaded region represents the region with AVT > 25%, the current benchmark for solar windows). References to the PCE and AVT data are listed in Table 1. The Shockley–Queisser (SQ) limits were adapted from Lunt.^[25]

semitransparent module ($\approx 1.9 \text{ m}^2$) comes in 10% AVT with PCE of $\approx 20\%$.^[58] For this review, the focus would be mainly on the first two approaches since they are “truly semitransparent” and more in line with the aesthetic requirements of BIPV.

3. Theoretical Potential and State of the Art of Semitransparent PV Technologies

Considering the photon flux distribution in UV (<435 nm), visible (435–670 nm), and NIR (>670 nm) regions of 3.9%, 22.6%, and 73.5%, respectively, there is a huge potential for improvements in AVT of STPVs if the cells can selectively harvest (high absorption or external quantum efficiency) UV and NIR regions (Figure 2a). Assuming the visible region from 435–670 nm (such that AVT > 99.5% and CRI > 95), Lunt^[25] calculated the thermodynamic limit of a single-junction single bandgap solar cell with varying degrees of AVT for wavelength selective (red plot line shown in Figure 2b) and non-wavelength-selective (black plot line in Figure 2b). Accordingly, even if we utilize $\approx 0\%$ of the visible region (100% AVT), the maximum PCE falls from 33.1% (0% AVT, opaque solar cells) to a modest 20.6% and the optimum optical bandgap changes from 1.36 eV (910 nm) to 1.12 eV (1100 nm). A nonselective semitransparent solar cell will always perform lower than the selective wavelength transmission-based solar cell in the normally accepted benchmark of >25% AVT.^[16]

In Figure 2b (data from Table 1), the LUEs of various top-performing STPV technologies are plotted, which gives an idea of the state of the art. STOPVs have exceptionally high LUE (with a record LUE of 5.35; PCE = 11.44% and AVT = 46.8%).^[62] STPSCs have slightly lower LUEs than STOPVs. Other STPV technologies are still lagging in terms of LUE (<3). However, the proven stability of thin-film technologies renders them comparatively more mature for commercialization.

4. Semitransparent Photovoltaic Technologies

4.1. Traditional Thin-Film Technologies

4.1.1. Amorphous Silicon

Amorphous silicon solar cells have an order of magnitude higher absorption coefficient than c-Si. Therefore, the thickness can be reduced to the sub μm range (in comparison silicon solar cells have thickness in the range of 100s of μm s) to tune the required transparency. However, due to short-range order, carrier diffusion lengths are short. Hence, hydrogen passivation (H in a-Si:H stands for hydrogenation) is a critical step. In turn, the bandgap can also be controlled by the amount of hydrogen.^[63] The higher bandgap of 1.9–2.0 eV results in higher transparency in the visible region at the expense of lower short circuit currents.

In generic semitransparent a-Si:H solar cells, p-type, intrinsic (i), and n-type amorphous silicon layers are deposited via plasma-enhanced chemical vapor deposition (PECVD) on a transparent conductive substrate. Finally, a top transparent conductive oxide (TCO) electrode is deposited through sputtering.^[64–66]

The highest LUE for a-Si:H based STPVs of 1.88 was reported by Yang et al.^[66] They used a p-type microcrystalline Si oxide ($\text{p-}\mu\text{c-SiO}_x\text{:H}$) as a wide bandgap window layer (instead of conventional p-type-a-Si:H layer) to reduce the parasitic absorption and enhance the conductivity. By reducing the energy level misalignment using an additional bilayer buffer, they achieved a PCE of 6.41% at an AVT of 29.3% (500–800 nm) (Figure 3a,b). In a-Si:H solar cells, a sharp decrease in efficiency is seen with thinning down of the active layer, since the fill factor (FF) drops significantly because of the creation of shunt paths, in addition to the loss in absorption (short circuit current density, J_{SC} loss).^[67,68] To overcome the shunt path and increase charge collection, Lim et al.^[67] used a resistive high bandgap layer. This high bandgap i-a-Si:H film was deposited by adjusting the hydrogen dilution ratio (R, the ratio of H_2 to SiH_4 flow rates). The resulting semitransparent solar cell had a PCE of 6.92% with AVT of 23.6% with

Table 1. List of top-performing STPVs.

Back contact	ETL/HTL/buffer layer	Absorber layer ^{a)}	HTL/ETL/buffer layer	Top electrode	PCE [%]	AVT [%]	LUE	Ref
a:Si								
GZO		p-i-n Si:H	—	GZO/Ag/OC(GZO)	6.36	23.5 [#]	1.49	[#0238]
FTO/GZO		p-i-n a-Si:H	—	GZO/Ag/Al ₂ O ₃ :TiO ₂ (3,1)	6.64	19.7 [#]	1.31	[#0064]
FTO	AZO	p- μ c-SiOx:H/p-a-SiOx:H/i-a-Si:H(buffer)/i-a-Si:H/n- μ c-SiOx:H	—	AZO	6.41	29.3 [#]	1.88	[#0066]
GZO		p-Si(buffer)/p-a-Si:H/i-a-Si:H/n-a-Si:H	—	GZO	5.83	25.4 [#]	1.48	[#0239]
GZO		p ⁺ -a-Si:H/i-a-Si:H(buffer \times 3)/i-a-Si:H/n-a-Si:H	—	GZO	6.92	23.6 [#]	1.63	[#0067]
FTO	—	p-nc-Si:H/p-SiO _x :H/i-a-Si:H/n-SiO _x :H	—	AZO	6.94	20.0 ^{###}	1.39	[#0372]
FTO	AZO	p-nc-SiC:H/i-a-Si:H/n-nc-Si:H	—	ITO	6.01	22.8	1.37	[#0070]
CIGS	AGS	CIGS	Cds/i-ZnO	ZnO:Al	5.94	25.5	1.51	[#0079]
FTO	—	CIGS	Cds/i-ZnO	ITO	10.5	12.3	1.29	[#0073]
FTO	—	CIGS	Cds/i-ZnO	ITO	6.89	18.5	1.28	[#0244]
FTO	—	CIGS	Cds/ZnO	ITO	6.46	18.6	1.20	[#0232]
ITO	—	CIGS	Cds/i-ZnO	ITO	10.54	6 ^{##}	0.63	[#0231]
ITO	—	CIGS	Zn(O,S)/ZnS/i-ZnO	ITO	12.41	4.00	0.50	[#0233]
ITO	—	CIGS	Cds/i-ZnO	AZO	9.38	18	1.69	[#0142]
CdTe	SnO ₂ /CdS	CdTe	—	Cu(0.9)/Au(20)	11	<6	0.66	[#0078]
FTO	SnO ₂ /CdS	CdTe	—	—	11.0	—	—	[#0075]
PSC	—	CdTe	—	—	10	10	1.00	[#0058]
ITO	NiO _x	CH ₃ NH ₃ Pb ₃	PCBM/Zr(acac) ₂	Ag(20)/CsF(15)	11.74	22.8	2.67	[#0256]
FTO	SnO ₂ /C ₆₀	C _{50,05} (FA _{0,85} MA _{0,15}) _{0,95}	VNPB	MoO _x (10)/Au(10)/MoO _x (35)	16.1	10.1	1.63	[#0257]
FTO	SnO ₂ /C ₆₀	Pb(1 _{0,85} Br _{0,15}) ₃	—	—	7.41	29.5	2.19	[#0257]
FTO	SnO ₂ /C ₆₀	C _{50,05} (FA _{0,85} MA _{0,15}) _{0,95}	VNPB	MoO _x (10)/Au(10)/MoO _x (35)	14.7	20.1	2.95	[#0178]
FTO	SnO ₂	Pb(1 _{0,85} Br _{0,15}) ₃	Spiro-OMeTAD	rGO/AgNWs/rGO	7.30	36.5	2.66	[#0258]
ITO	PEDOT:PSS	K _x Cs _{0,05} (FA _{0,85} MA _{0,15}) _{0,95}	—	—	14.0	22.6	3.16	[#0258]
ITO	PEDOT:PSS	Pb(1 _{0,85} Br _{0,15}) ₃	PCBM/PEI	p-AgNW	11.8	17	2.01	[#0259]
ITO	PEDOT:PSS	CH ₃ NH ₃ PbCl _{3-x}	PCBM/PEI	p-AgNW	11.0	25.6	2.82	[#0373]
ITO	NiO/DEA	CH ₃ NH ₃ PbCl _{3-x}	PCBM/AZO	SnO _x (20)/Ag(7)/SnO _x (20)	12.6	21.5	2.71	[#0373]
ITO	NiO/DEA	CH ₃ NH ₃ PbI ₃	PCBM	PNANI/Ag(10)	8.49	45.4	3.85	[#0327]
ITO	NiO/DEA	CH ₃ NH ₃ PbI ₃	PCBM	PNANI/Ag(14)	10.3	41.5	4.26	[#0327]
FTO	TiO ₂	CH ₃ NH ₃ PbI _{3-x} Cl _x (AAO scaffold)	Spiro-OMeTAD	MoO _x /ITO	10.53	32.5	3.42	[#0112]
FTO	TiO ₂	CH ₃ NH ₃ PbI _{3-x} Cl _x (AAO scaffold)	Spiro-OMeTAD	MoO _x (5)/IZO	13.61	24.7	3.35	[#0170]
ITO	SnO ₂	C _{50,05} FA _{0,83} MA _{0,12} PbB _{0,33} ^{1,2,67}	Spiro-OMeTAD	IZTO	15.4	25.5	3.93	[#0374]
ITO	NiO	(Cs _{0,175} FA _{0,825} Pb(1 _{0,875} Br _{0,125}) ₃)	PMMA:PCBM/ZnO	—	14.01	31.7	4.44	[#0113]
AgNW	PEDOT:PSS	C _{50,05} FA _{0,85} MA _{0,10} Pb(1 _{0,97} Br _{0,03}) ₃	PCBM/VO ₂	BCP(1)/Cu(1)/Au(7)	12.83	21.7	2.79	[#0143]
ITO	SnO ₂	CsPbI ₂ Br	PTAA	—	—	—	—	—
ITO	PTAA	(FA _{0,65} MA _{0,2} Cs _{0,15})Pb(1 _{0,8} Br _{0,2}) ₃	LiF/C60/PEIE	ITO	—	—	—	—

(Continued)

Table 1. (Continued).

OPVs	Back contact	ETL/HTL/buffer layer	Absorber layer ^{a)}	HTL/ETL/buffer layer	Top electrode	PCE [%]	AVT [%]	LUE	Ref
	ITO	SnO ₂	CH ₃ NH ₃ PbI ₃	Spiro-OMeTAD	ZnO (10)/Ag (10)/ZnO (35)	10	19.6	1.96	[#0280]
	ITO	PEDOT:PSS	PBD-TF:Y6-BTPC	PFN-Br	Ag (12)	13.1	22.3	2.93	[#0129]
	ITO	PEDOT:PSS	PM6:Y6	PDIN	Au (1)/Ag (20)	14.2	8.9	1.26	[#0375]
	ITO	PEDOT:PSS	PM6:Y6	PDIN	Au (1)/Ag (10)	12.4	18.6	2.30	[#0375]
	ITO	PEDOT:PSS	J71:PTB7-Th:IHIC	PDINO	Au (0.8)/Ag (15)/[MoO ₃ /LiF] ³	9.37	23.6	2.21	[#0124]
	ARC(SiO ₂ (130)/MgF ₂ (120))/ITO	ZnO/NSM	PCE-10:B-CiC:IT-FIC	MoO _x	Cu ₂ Ag (16)/OC(CBP(40)/MgF ₂ (100)/CBP(70)/MgF ₂ (40))/[DBR(SiN _x (120)/SiO ₂ (130))]12.5	8.0	44.2	3.54	[#0254]
	ITO	SnO ₂	PTB7-Th:IEICO-4F	MoO _x	Au (15)	7.26	26.3	1.91	[#0171]
	ITO	SnO ₂	PTB7-Th:IEICO-4F	MoO _x	Ag (15)	8.74	25.0	2.19	[#0171]
	ITO	SnO ₂	PBDB-T:IEICO-4F	MoO _x	Ag (15)	6.64	26.5	1.76	[#0171]
	ITO	SnO ₂	PBDB-T-2F:ITIC-4F	MoO _x	Ag (15)	11.2	26.2	2.94	[#0171]
	ITO	SnO ₂	PBDB-T-2F:Y6	MoO _x	Ag (15)	12.9	25.6	3.30	[#0171]
	ITO	SnO ₂	J71:IT-M	MoO _x	Ag (15)	7.23	25.0	1.81	[#0171]
	ITO	SnO ₂	J71:IEICO-4F	MoO _x	Ag (15)	4.45	27.3	1.21	[#0171]
	ITO	ZnO	PTB7-Th:IUIC	MoO _x	Au (1)/Ag (15)	10.2	31	3.16	[#0255]
	ITO	PEDOT:PSS	PBN-S:IT-4F	ZnO	Au (1)/Ag (20)	9.83	32	3.15	[#0328]
	ARC(SiO ₂ (130)/MgF ₂ (120))/ITO	ZnO	PCE-10:A078	MoO _x	Ag (16)/OC(CBP(45)/MgF ₂ (100)/CBP(70)/MgF ₂ (35))	10.8	45.7	5.0	[#0048]
	ITO	ITO	PM6:Y6-BO:2PACz	PNDIT-F3N	Ag (15)	15.2	19.2	2.91	[#0376]
	ITO	ITO	PM6:Y6-BO:2PACz	PNDIT-F3N	Au (0.1)/Ag (8)	12.0	28.1	3.37	[#0376]
	ITO	ZnO	PBTZT-stat-BDIT-8-PCBM	PEDOT:PSS	AgNW	5.2	10	0.52	[#0123]
	ITO	NiO/PEDOT:PSS	Tandem [FAPbBr _x Cl _{3-x} & PTB7-Th:6ITIC-4F]	PCBM/ZnO	ITO	10.83	52.9	5.7	[#0146]
	ITO	PEDOT:PSS	PTB7-Th:6ITIC-4F	ZnO	ITO	5.90	61.7	3.64	[#0146]
	ARC(LiF)/TeO ₂ /ITO	PEDOT:PSS	PM6:BTP-eC9:L8-BO	PDINN	Ag (12)/aperiodic [LiF/TeO ₂] ⁸ /LiF	11.44	46.8	5.35	[#0062]
	ITO	PEDOT:PSS	PBDB-TF:L8-BO:BTP-eC9	Bis-FIMG	Ag (13)/OC[TeO ₂ (45)]	12.95	38.7	5.0	[#0122]
DSSC	FTO	TiO ₂	N719	—	Pt/FTO	7.77	34	2.64	[#0046]
	FTO	TiO ₂	YKP-88	—	Pt/FTO	8.7	26	2.26	[#0137]
	FTO	TiO ₂	Y1+HSQ5	—	Pt	3.66	60.3	2.21	[#0136]
	FTO	TiO ₂ /Ga ₂ O ₃	VG20-C16 + CDCA	—	Pt	3.1	76	2.35	[#0047]
	FTO	TiO ₂	TTZ5	—	Pt	5.1	35.7	1.82	[#0311]

^{a)} The full names of absorber layers, especially for organic photovoltaics (OPVs) can be found in the corresponding references. Similarly, names of some organic HTLs and ETLs have been left unexpanded. Thicknesses (in nm) of thin metal and dielectric films are given in brackets, for example, Au(10). GZO: ZnO:Ga; AZO: ZnO:Al; # Average transmittance (500–800 nm); ## Average transmittance (400–800 nm); ### Average transmittance (380–780 nm); OC, outcoupling layer; ARC, antireflection coating; DBR, distributed Bragg reflector; AGA, sulfurized AgGa; DEA, diethanolamine; IZO, indium/zinc co-doped In₂O₃.

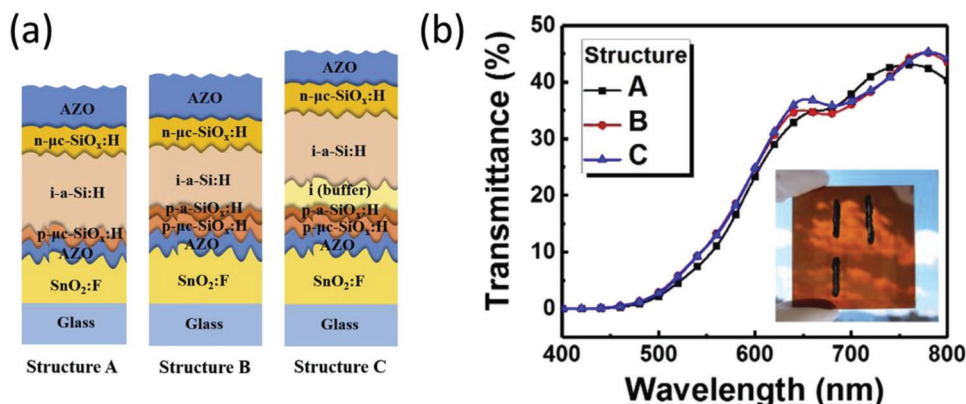


Figure 3. a) Schematics showing the device structure of semitransparent a-Si:H solar cells with p- $\mu\text{c-SiO}_x\text{:H}$ window layers. To further improve the device performance, structures B and C include additional single and dual buffers, respectively, at p/i interface. b) Transmittance spectrum of semitransparent solar cells of structures A–C in the visible region. Reproduced with permission.^[66] Copyright 2019, Elsevier.

a-Si:H absorber thickness of just 115 nm (structure C in Figure 3a). Structures A and B (Figure 3a) had PCEs of 5.4% and 6.00% and AVTs of 28.2% and 29.0%, respectively.

In a-Si:H solar cells, silicon is the main raw material, which is also non-toxic and in abundant supply. The process temperatures are relatively low at around 200 °C, and low-cost soda-lime glass substrates can be used.^[34] The most common deposition technique for a-Si, PECVD, is already in industrial-level production. The opaque thin film a-Si solar cells have proved stability and reliability for commercial applications.^[69] Also, because of the low-temperature coefficient, they perform better in high-temperature conditions.^[70] These attributes are attractive for large-scale adoption.

However, due to the large bandgap (1.75 eV) and insufficient absorption of longer wavelengths, the PCE of a-Si semitransparent solar cells has remained low ($\text{LUE} < 2$); therefore, the potential of this mature technology seems limited. Newer approaches, such as modifications in the absorber layer composition (e.g., alloying with Ge)^[71] or using μ -crystalline window/buffer layers to enhance absorption and reduce recombination losses,^[65,66] have also been explored. The lack of color tunability is still a limiting factor for specific aesthetic applications. However, secondary methods (like multilayered electrodes)^[72] for color tunability have also been applied. These secondary methods of light management (discussed in a separate section later), including antireflection coatings (ARCs), Bragg reflectors, and plasmonic nanoparticles, would be relevant to all the STPV technologies discussed in this review.

4.1.2. Chalcopyrite-Based

CdTe: Semitransparent CdTe thin-film solar cell is a well-established PV technology generally constituting an n-type CdS layer (30–100 nm) onto which the p-type CdTe is deposited commonly using close space sublimation, with a thickness of 250–400 nm, depending on the required transmittance.^[34] A TCO layer ($\text{SnO}_2\text{:F}$ [FTO], ZnO:Al [AZO], or $\text{In}_2\text{O}_3\text{:Sn}$ [ITO])^[73] is first deposited on the glass substrate, and the final transparent

contact (back contact) is usually a TCO (ITO, etc.) or ultrathin metallic layer (a few nanometers of Cu, Au, or Ag).^[74–77]

For CdTe solar cells with a slightly higher absorption coefficient than a-Si:H, it is possible to reach a saturation J_{SC} at the absorber thickness of just several micrometers.^[80] Kosyachenko et al.^[81] calculated the J_{SC} potential of CdTe thin-film solar cells. Accordingly, almost all photons ($\geq 99.9\%$) in CdTe in the $h\nu > E_g$ range will be absorbed in a layer thickness of more than 20–30 μm , while there is a mere 20% loss in J_{SC} when the thickness is 500 nm.

According to Jones et al.,^[82] the efficiency starts dropping sharply at thicknesses below 1 μm (similar to a-Si:H solar cells), suggesting that the cells are limited not only by optical losses but also by an increase in the interface defect density with thinner absorbers. In addition to J_{SC} reduction with the thickness (from 2 μm to 200 nm), the decrease in open circuit voltage (V_{OC}) and FF was found to be even sharper. A sharp decrease in V_{OC} was also observed by Gupta et al.,^[83] stressing the need for optimization of processing conditions.

However, some groups reported a J_{SC} -limited predictable decrease in PCE with decreasing thickness of the CdTe absorber layer in the sub μm range. In this case, J_{SC} loss due to insufficient absorption was the main contributor to the PCE loss, and efficiency followed the equation (dashed line in Figure 4a). Paudel et al.^[76] reported PCEs of 8% and 11% at thicknesses of 250 and 500 nm, respectively, with high-quality CdTe deposited via RF magnetron sputtering. Similarly, Plotnikov et al.^[77] prepared cells of thicknesses 1, 0.5, and 0.3 μm and yielded efficiencies of 12%, 9.7%, and 6.8%, respectively. Furthermore, commercial modules developed by Lucintech Inc. with PCE up to 12% using only 500 nm CdTe thick film have also been reported (Figure 4b).^[74,84]

In the most widely reported semitransparent CdTe solar modules, the optimum thickness of the CdTe layer is in the range of 200–500 nm; thus, it is more sensitive to the variations in thickness (compared to the normal opaque cell thickness of a few micrometers). Therefore, this ultrathin layer must be deposited with an extremely low density of pinholes, which becomes a challenge, especially over an area of 1 m^2 or larger. Sometimes a buffer layer (highly resistive transparent, HRT) such as SnO_2 or ZnO ,^[85] is introduced to reduce the effects of such pinholes/non-uniformities.

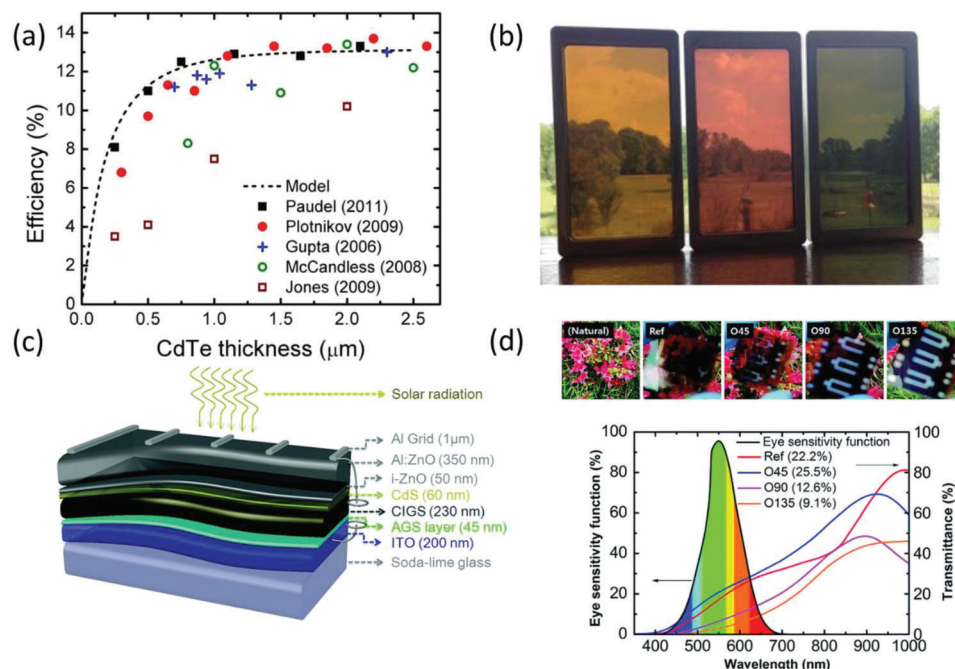


Figure 4. a) Efficiency of reported ultra-thin CdTe cells as a function of CdTe thickness. The dashed curve is the calculated efficiency based on 100% absorption. Reproduced with permission.^[78] Copyright 2011, IEEE. b) Photograph of 3" × 5" CdTe minimodules with transmitted color spectrum control—addition of light-absorbing and/or reflecting elements on naturally bronze module (on the left). Reproduced with permission.^[75] Copyright 2013, IEEE. c) The device structure of the semitransparent CIGS device based on 230 nm thick CIGS modified with the 45 nm thick sulfurized-AgGa (AGS) layer at the CIGS/ITO interface. d) Top: Photograph of Ref CIGS (without AGS layer and thickness of CIGS = 300 nm) and CIGS modified with AGS layers. Bottom: Human eye sensitivity response curve and transmittance spectrum for Ref and modified CIGS on ITO-glass. Averaged values of transmittance for each film (Ref: CIGS [300 nm], AGS [0 nm]; O45: CIGS [230 nm], AGS [45 nm]; O90: CIGS [400 nm], AGS [90 nm]; O135: AGS [45 nm]; O90) in the spectral range of 400 to 800 nm are enclosed in the brackets in the legend. For example, O45 represents a combination of 230 nm CIGS and 45 nm AGS layers, and has average transmittance of 25.5%. Reproduced with permission.^[79] Copyright 2016, Royal Society of Chemistry.

The scarcity of Te and toxicity of Cd might seem to be barriers to large-scale application. However, the scalability issue would not be a challenge for the BIPV CdTe modules where thicknesses remain lower than 500 nm (low material usage), and the toxicity of CdTe is 100 × lower than that of elemental Cd.^[85,86]

CdTe PV modules are comparable in price to a-Si modules, but the higher efficiency of CdTe PV technology makes it relatively more viable in BIPV applications.^[87] In the last 10 years, the PCEs of CdTe solar cells have increased sharply, mainly due to the addition of selenium to the CdTe absorber layer (forming a lower bandgap CdSe_xTe_{1-x} alloy).^[88] First Solar has achieved a record PCE of 22.1% in opaque cells (0.5 cm²), demonstrating PCE competitiveness. CdTe, therefore, leads the market among the three thin-film PV technologies (in opaque form). Additionally, CdTe performs better than c-Si photovoltaics in outdoor environments, especially at higher temperatures.^[89]

CIGS: In conventional opaque CIGS solar cells, an absorber layer of thickness 1.5–2 μm is deposited on metallic Mo rear contact, reaching record PCEs >23%.^[90] For reasonable semitransparency in CIGS solar cells, the thickness of the absorber layer should be around 300 nm (as is the case with CdTe solar cells), reducing both the consumption of costly indium metal and deposition time.^[73]

In the semitransparent counterpart, the bottom opaque Mo electrode is replaced by FTO, ITO, or AZO (Al-doped ZnO). The top contact consists of intrinsic ZnO and AZO, deposited

by sputtering, and the conventional opaque device processing can be replicated for these layers.^[91] Apart from thickness, tuning of bandgap by changing the ratio of component elements in the CIGS class of chalcopyrite is another way of controlling the transmittance of the absorber layer. The bandgap of Cu(In_(1-x)Ga_x)(S_ySe_(1-y))₂ absorber layer follows the equation:^[92]

$$E_g^{CIGSSe}(X, Y) = (1.00 + 0.13X^2 + 0.08X^2Y + 0.13XY + 0.55X + 0.54Y) \text{ eV} \quad (3)$$

where atomic ratio $X = \text{Ga}/(\text{Ga} + \text{In})$ and $Y = \text{S}/(\text{S} + \text{Se})$. $E_g^{CIGSSe}(X, Y)$, therefore, can lie between 1.00 eV ($X = 0, Y = 0$, or CISE) and 2.43 eV ($X = 1, Y = 1$, or CuGS₂).

The Mo layer has been the material of choice for rear contact in opaque CIGS solar cells because of its suitable properties such as inertness during deposition, favorable properties for the growth of large CIGS grains, and formation of ohmic contact and self-passivation with CIGS (with the formation of MoSe₂ layer).^[93–95] However, devices using TCOs (such as FTO, ITO, or AZO) need optimization of processing conditions or the introduction of additional buffer layers to passivate the TCO/CIGS interface, to achieve performance comparable with Mo electrode.^[96] These oxide films are susceptible to degradation of interface and can result in the formation of unwanted Ga₂O₃ layer at high-temperature processes >550 °C (in co-evaporation method^[97] or

two-step selenization process^[98]) used during CIGS layer deposition and post-deposition alkali treatments.^[99] This implies the need for modification in the deposition parameters^[100,91] or alternate deposition methods like low temperature (250 °C) pulsed electron deposition.^[101,102] To illustrate the influence of back electrodes on device performance, Mollica et al.^[96] fabricated bifacial semitransparent CIGS solar cells with FTO and AZO as the back contacts and reported PCEs of 9.8% and 8.2%, respectively. In comparison, the reference cell with Mo back contact achieved a PCE of 10.2%. The main reason is that the contact resistivity (Electrode/CIGS/Au) for Mo, FTO, and AZO was found to be 0.04, 0.9, and 2.3 $\Omega\text{-cm}^2$, respectively. Additionally, for both the TCOs, charge carrier recombination velocities (carrier recombination velocity: a parameter used to characterize recombination due to surface defects) were higher than that of Mo back contact, stressing the need for the passivation of back contact in TCO-based devices for applications in STCIGS solar cells.

In STCIGS cells with thinner absorber layers (with incomplete absorption of light), back contacts also influence the reflection/absorption at the contact surface and thus influence the J_{SC} of the solar cell.^[95,96] A remedial strategy was reported by Shin et al.^[73] wherein a textured PDMS layer with scattering and antireflection properties was attached to the rear contacts (textured FTO or flat ITO) as a low-cost light management technique. They achieved high PCEs of 10.5% with an AVT of 12.3%, with ITO as the transparent back electrode (absorber thickness = 322 nm).

Expectedly, the shunting paths are created when the thickness of the CIGS films is decreased in the sub-micron range.^[103] Saifullah et al.^[79] reduced the bulk and back surface recombination. They achieved high shunt resistance in an ST-CIGS solar cell with a 230 nm CIGS absorber layer with the introduction of a multifunctional AGS (sulfurized-AgGa) layer between the CIGS absorber and ITO back contact (Figure 4c,d). They reported a PCE of 5.94% with AVT over 25%, the highest LUE for STCIGS solar cells.

Because of the inherent chemical and photo stability of CIGS, semitransparent solar cells based on this technology present immense opportunities in BIPV applications.^[34] At the same time, the lack of commercially available STCIGS in the market means that the performance (both PCE and AVT) of this STPV technology needs further optimization.

Both CIGS and CdTe solar cells employ simpler processes compared to conventional crystalline silicon cells, and their PCEs are higher than a-Si solar cells. In addition to innovative BIPV applications, using a thinner absorber layer reduces the deposition time and material cost of rare-earth materials.

CIGS and CdTe represent the next most relevant PV technologies after c-Si solar cells for the overall photovoltaics market, in addition to the advantage of adaptability for STPV applications and curved/flexible substrates. Additional current enhancement strategies, such as the introduction of Bragg reflector^[104,105] or plasmon resonance structure^[104,106] on the back side (non-illuminating side), could increase the J_{SC} (these techniques are later discussed in detail in Section 5.3).

Thin-film solar cell devices perform better than crystalline silicon solar cells in high-temperature and low and diffuse light conditions. Nevertheless, material shortage and toxicity of materials used in CIGS and CdTe thin-film solar cells and low PCE of a-Si

technology have motivated increased research in emerging thin-film solar photovoltaics.

4.2. Emerging Third-Generation Semitransparent Photovoltaics

4.2.1. STPSCs

Semitransparent perovskites (STPSCs) have attracted attention due to high PCEs in opaque devices (>25%) and high LUEs for STPVs among the semitransparent solar cell technologies (Figure 2b).^[107–110,15] A typical semitransparent perovskite solar cell consists of a transparent conductive substrate, electron/hole transport layers (ETLs/HTLs) on either side of the perovskite layer, and a top transparent electrode such as a TCO (e.g., indium gallium zinc oxide, IGZO in Figure 5a,b) or ultrathin metal.^[111]

As illustrated by Lim et al.,^[111] certain PCE loss is inevitable when the traditional opaque electrode is replaced by a semitransparent top electrode. For instance, the STPSC device with a low-temperature processed IGZO electrode achieved a PCE of 15.6% (with an AVT of 10.5%), compared with 16.4% for an opaque evaporated Ag. The PCE loss would be more severe for devices with higher AVT, which require even thinner perovskite layers. One solution is to utilize a higher bandgap perovskite absorber layer so that high AVT (>20%) can be obtained without reducing thickness substantially. Wang et al.^[113] introduced a wide bandgap inorganic CsPbI₂Br perovskite film ($E_g = 1.9$ eV) to obtain a record LUE among STPSCs. A high-quality film was obtained via: a) intermediate adduct engineering to control the rate of crystallization and b) the introduction of a Schiff base additive. A STPSC with an optimized structure of ITO/SnO₂/CsPbI₂Br/(poly[bis(4-phenyl)(2,4,6-trimethylphenyl)amine]PTAA/BCP/Cu (1 nm)/Au (7 nm) showed a PCE of 14.01% at an AVT of 31.7% (a record LUE of 4.44).

Apart from achieving high LUE, the tunability of the color of STPV devices provides an additional customizable dimension for novel specialized applications.^[114,115] At the same time, for applications where neutral color is a prerequisite, a selected area transmission approach can be used to create islands of perovskite nanostructures that can retain some transparency even for thick perovskite layers.^[52–57] The transparency can be controlled by controlling the effective surface coverage area of the perovskite absorber—an alternative to thinning down the active layer. In such a device design, an interesting or rather counterintuitive observation was the good rectification behavior even with the discontinuous layers of perovskites, which was explained by the presence of a good diode behavior with a turn-on voltage of 0.7 V in areas with 0% perovskite coverage versus >1.0 V for 100% perovskite coverage.^[57] However, in cases where the recombination does take place due to direct contact of ETL and HTL, a passivation layer (such as polystyrene, PS) can be inserted as reported by Hyuck Heo et al.^[55] Zhu et al.^[112] demonstrated a moth-eye-inspired structure (MEIS) for highly efficient, neutral-colored ST perovskite solar cell with a high LUE of 3.42. The biomimetic microstructure of the device layers enhanced light-trapping and carrier collection at the interface. A PCE of 10.53% with an AVT of 32.5% was achieved as compared to 8.78% and 35% for the planar device, respectively (Figure 5c,d).

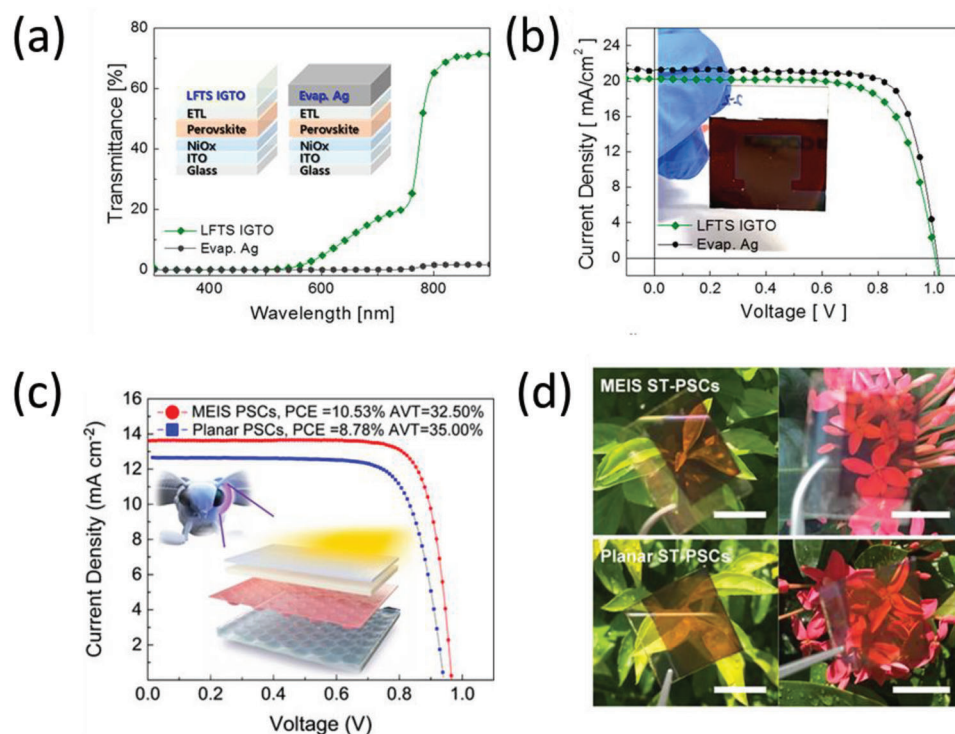


Figure 5. a) The optical transmittance and b) J - V characteristics comparison between the semitransparent PSCs with an IGTO top cathode and the opaque PSCs with an Ag top cathode. Reproduced with permission.^[111] Copyright 2021, American Chemical Society. c) J - V curves of the champion planar and MEIS ST-PSCs based on $\text{Cs}_{0.05}\text{FA}_{0.83}\text{MA}_{0.12}\text{PbBr}_{0.33}\text{I}_{2.67}$ under simulated AM1.5G illumination, with an active area of $\approx 0.03\text{ cm}^2$; inset: complete compound moth eyes and the moth-eye-inspired structure (MEIS) device structure diagram. d) The photographs of devices in (c) taken under outdoor sunlight (scale bars, 2 cm). Reproduced with permission.^[112] Copyright 2016, Wiley-VCH.

“Smart” semitransparent perovskites in windows have attracted attention due to their tunable transparency and power generation. Lin et al.^[116] demonstrated thermochromic solar effect for smart PV window applications utilizing the structural phase transitions in the inorganic halide perovskite absorber layer. The perovskite layer undergoes reversible transitions between a transparent non-perovskite phase (81.7% visible transparency) and a working perovskite phase (35.4% visible transparency) with high power output. Kim et al.^[117] reported a semitransparent perovskite solar cell with thermal mirror capability using a top transparent electrode (14 nm thick Ag) with high index dielectric layer capping (ZnS) to promote selective transmittance in the visible region and high reflectance in the near-infrared region. With the top electrode modification, a high NIR solar energy rejection ratio (NIR-SER) of 85.5% was reported with the most common perovskite solar cell structure with TiO_2 , spiro-OMeTAD, and MAPbI_3 as ETL, HTL, and perovskite layer, respectively. NIR-SER is relevant to the reduction of total energy load of the building. Similar dielectric/metal combinations have been applied in other reports of semitransparent perovskites^[118,119] and OPVs^[120,121] to enhance the transmittance and tune the visual appearance of the solar cells (also discussed in Section 5.3). These design possibilities in semitransparent perovskites make them attractive for a plethora of nonconventional applications.

Perovskites have favorable attributes such as low cost and easy processability, high PCE (and high LUE), bandgap, and color tun-

ability. However, several limitations hinder the widespread adoption of perovskites in BIPV applications. These include but are not limited to, J - V hysteresis, photo-oxidation of the active layer, low stability against oxygen, and moisture. In addition, the choice of an optimal top electrode is still under investigation because of the challenge to incorporate TCOs such as ITO as the top electrode without significant loss in PCE (due to damage during deposition) and higher degradation of stability compared to an opaque device.

4.2.2. STOPVs

Organic materials are abundant, non-toxic, lightweight, and mechanically flexible, with low material consumption, making them the cheapest source of electricity, potentially. A typical semitransparent organic solar cell consists of an electron transport layer deposited on TCO, an active layer (usually a combination of donor and acceptor polymers/small molecules) with a tunable absorption region, an HTL, and a semitransparent top electrode. The rapid increase in PCEs of OSCs in the last few years has been possible due to the emergence of a new class of narrow bandgap acceptor materials called non-fullerene acceptors (NFAs), in contrast to conventional acceptors based on fullerene derivatives. Non-fullerene acceptors can be easily tuned to match the required absorption region (can be carefully designed to achieve high AVT) and are less expensive.^[28] The top electrode,

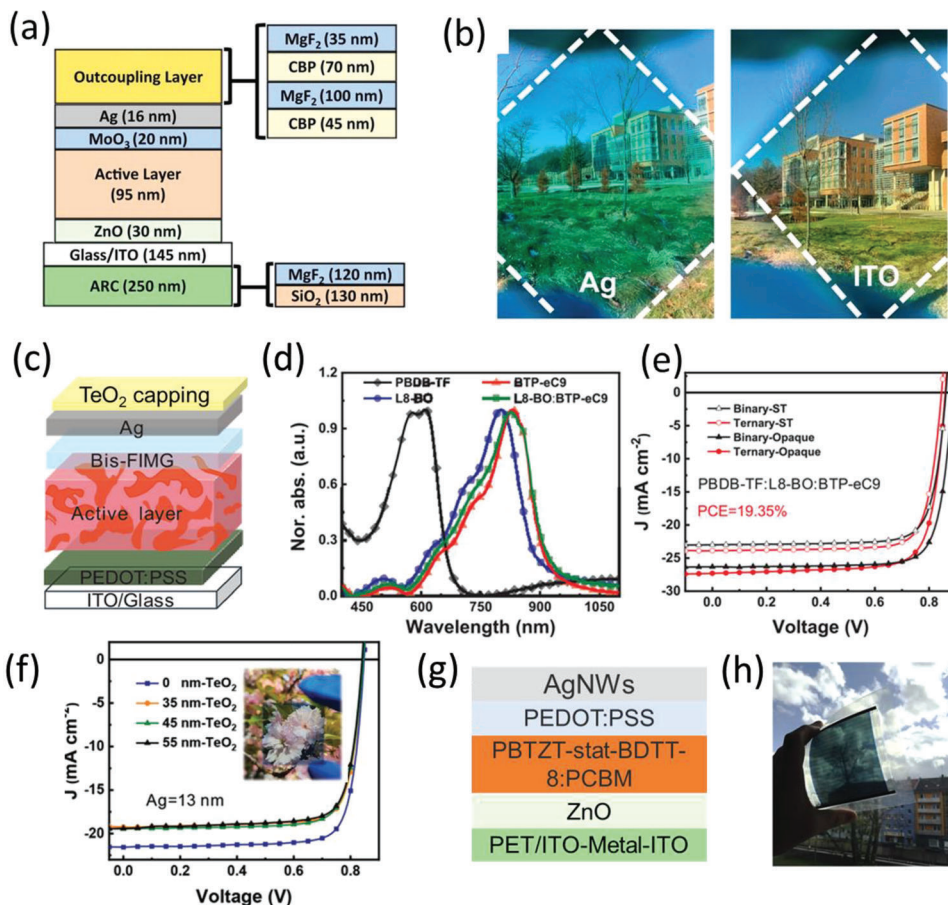


Figure 6. a) Schematic of the optimized semitransparent device, with detailed design of optical coupling (OC) and anti-reflection (AR) layers. b) Photograph of the appearance of outdoor through the (left) ultrathin Ag and (right) ITO electrode-based semitransparent device. Reproduced with permission.^[48] Copyright 2020, National Academy of Sciences. c) The device structure of a STOSC with a TeO₂ capping layer. d) UV-vis absorption spectra of polymer donor PBDB-TF and NFAs L8-BO, BTP-eC9, and L8-BO:BTP-eC9 films. They form the active layer in (c). e) *J*-*V* curves of the binary PBDB-TF:L8-BO and ternary PBDB-TF:L8-BO:BTP-eC9 opaque devices and the corresponding ST-OPVs. f) *J*-*V* curves ST-OPVs (Ag = 13 nm) with varied TeO₂ capping layer thicknesses of 0, 35, 45, and 55 nm. Inset shows the photograph and appearance of the optimized STOSC device. Reproduced with permission.^[122] Copyright 2022, Wiley-VCH GmbH. g) A typical device structure employing solution-processed silver nanowire (AgNW) top electrode in large area module fabrication and h) photograph of the corresponding module of 30 individual cells (cell size of 6.58 cm²) with a total active area of 197.40 cm². Reproduced with permission.^[123] Copyright 2017, Elsevier.

which is generally metal (Ag, Au, Al with thickness around 100 nm) in opaque structures, is replaced by a semitransparent electrode.^[42]

In the context of STPVs, OPVs (and DSSCs using organic dyes) have a unique advantage: structured narrow-band absorption with well-defined absorption maxima and minima. Therefore, a photoactive layer can be designed with donor and acceptor absorbing in UV and near-IR regions selectively or prominently. This results in high AVT and high PCE simultaneously.^[124,28] This unique advantage is particularly important in multifunctional STOPVs, where the power-generating windows also need to be aesthetically acceptable with neutral colors or where low-energy IR photons need to be reflected to enhance heat dissipation (quantified by infrared rejection rate, IRR).^[125–129] Furthermore, optical engineering (Bragg reflection layer,^[129] outcoupling [OC] layers [1D-phonic crystals],^[130,48] etc.) can also be employed to increase effective light absorption and tune color perception (discussed later in Section 5.3).

Recently, Li et al.^[48] reported a color-neutral semitransparent OPV with high LUE ($3.5 \pm 0.3\%$) using ITO as both cathode and anode (device structure and photograph are shown in Figure 6a,b, respectively) and optically engineered light management (OC layer and ARC) as shown in Figure 6a (right). At the same time, the devices were color neutral (Figure 6b) with CRI of 86, CCT of 4143 K, and chromaticity coordinates of (0.38, 0.39). Additionally, using thin Ag film as the anode, they reported high PCE ($10.8 \pm 0.5\%$) and high AVT ($45.7 \pm 2.1\%$)—one of the highest LUE (among all single junction semitransparent solar cells) of ($5.0 \pm 0.3\%$). Wang et al.^[129] achieved an excellent IRR of 90% (780–2500 nm), along with 23% AVT and over 12% PCE—a multifunctional device with power generation, visible transmittance, and low energy infrared reflection. They used a combination of two approaches to achieve excellent PCE, AVT, and IRR: a) a ternary blend of NIR acceptors in the active layer and b) a photonic reflector to match the peak transmittance (555 nm) to the photopic response of the human eye. Guan et al.^[122] performed

a comprehensive optimization to enhance invisible (UV and NIR) energy utilization and visible light transmission in a device structure ITO/PEDOT:PSS/active layer/bisfulleropyrrolidinium tris(methoxyethoxy)phenyl iodide/Ag/TeO₂ capping layer (Figure 6c). They used a ternary active layer blend with selective absorption in UV and NIR regions. Figure 6d shows the absorption spectrum and Figure 6e shows the *J*-*V* curves of binary and ternary OPV devices. Subsequently, upon optimizing the donor:acceptor ratio, thickness, and antireflection (via TeO₂ capping layer thickness variation), they obtained a high LUE of 5.01 (PCE = 12.95% and AVT = 38.67%). The *J*-*V* curves of STOSC devices with different capping layer thicknesses are shown in Figure 6f. A representative photograph of the device with 45 nm TeO₂ capping layer and 16 nm Ag electrode is also shown in the inset of Figure 6f. Among single-junction STOPVs, the current record LUE of 5.35% is held by Liu et al.^[62] They designed a superior transparent rear electrode in the form of an aperiodic band-pass filter (ABPF; alternating TeO₂ and LiF layers) to enhance visible transmittance and total reflection in the NIR region (700–900 nm). In addition, an ARC was also applied on the glass substrate, with the final device structure as (LiF/TeO₂)⁴/glass/ITO/PEDOT:PSS/PM6:BTP-eC9:L8-BO (0.8:1:0.2)/PDINN/Ag (12 nm)/(LiF/TeO₂)⁸/LiF. Although LUEs > 5 reported in recent years in STOPVs is quite attractive, it should be highlighted that they use complicated optical engineering (discussed in detail in Section 5.3), which would add to the cost of the final device. Therefore, STOSC with a high LUE of 5.01, reported by Hung et al.,^[131] is quite promising. They used a sequential deposition of donor and acceptor layers in the device structure of ITO/PEDOT:PSS (25 nm)/active layer (80–100 nm)/PDINO (20 nm)/Ag (15 nm)/MoO₃ (35 nm). Both light transmission and performance were optimized by tuning the donor and acceptor independently.

STOPVs can also benefit from inherent flexibility, promising niche applications along with potentially cheap roll-to-roll manufacturing. Lucera et al.^[123] fabricated a flexible STOPV module (69 cm²) with the device structure PET/IMI /ZnO/PBTZT-stat-BDIT-8:PCBM:PEDOT:PSS/AgNW (Figure 6 g,h), achieving PCEs of 4.8% (AVT = 10%).

Although semitransparent organic solar cells have unique features such as color tunability and multifunctional applications (BIPV, indoor photovoltaics, colorful solar cells, thermochromic functions, IRR, etc.), some specific challenges to this solar cell technology remain, such as a) use of toxic solvents, b) lower stability, c) complex material synthesis, thus expensive active layer materials, and d) unproven or limited scalability and stability.^[132,133,28]

4.2.3. STDSSCs

A semitransparent DSSC consists of a transparent conductive substrate (usually FTO or ITO) as front contact, a (typically screen printed) mesoporous TiO₂ photoanode, dye molecules as a sensitizer, an electrolyte redox couple in a salt solution, and a counter electrode (CE).^[134] The absorber in DSSC solar cells is typically a monolayer of dye molecules; therefore, tuning its absorption region away from the maxima of eye sensitivity (500–600 nm)

can impart sufficient semitransparency, similar to organic solar cells.^[135]

Zhang et al.^[136] reported STDSSCs exhibiting high AVT of 60.3% and PCE of 3.66%. They used a cocktail of UV and NIR dye to selectively absorb in the low eye-sensitivity region, thus achieving very high AVT (Figure 7a). Naim et al.^[47] reported a NIR selective (NIR-DSSC) solar cell with 3.1% power conversion efficiency, approaching an impressive AVT of 76%. They developed a NIR selective heptamethine cyanine dye (VG20-C₁₆) with sharp and intense absorption in the NIR region (with λ_{\max} at 834 nm) and a sharp fluorescence emission band at $\lambda_{\max} = 850$ nm (Figure 7b). In addition, they optimized the aesthetic performance of the devices by replacing the light yellowish I₃⁻/I⁻ redox couple (Figure 7c) with Co(bpy)₃^{3+/2+} redox couple, achieving a CRI of 92.1, CCT of 4223 K, and *x,y* chromaticity coordinates near-colorless region (*x* = 0.349, *y* = 0.360). Godfroy et al.^[137] recently reported a semitransparent minimodule (Figure 7d) with a promising PCE of 8.7% at AVT of 26%, using a benzothiadiazole-based molecule dye, YKP-88.

The counter electrode made with ≈1–2 nm thick Pt on FTO has been the traditional choice, but given the low transmittance Pt (71.6% at 1.6 nm for Pt, compared to >80% for FTO or ITO), thinner layers of ≈0.5 nm (≈76% at 0.5 nm) have also been used without appreciable loss in PCE.^[138] At the same time, very thin Pt coating is susceptible to corrosion within I⁻/I₃⁻ redox electrolyte. Also, given the scarcity and high cost of Pt, alternative counter electrodes with sufficient transparency, conductivity, and catalytic activity, such as silver nanowires (AgNWs), carbon nanotubes, graphene, or polymer electrodes, have been explored.^[42] These alternative electrodes are also compatible with STDSSCs but significant improvements are needed to increase the performance with these alternatives.^[139] These alternative electrodes and their advantages and shortcomings are discussed later in the section dedicated to TCEs.

The fabrication process of DSSC is quite insensitive to environmental conditions, and thus they can be prepared under ambient conditions without the need for high-level processing or expensive substrates. The device consists of nontoxic and cheap raw materials. DSSCs work particularly well in low-light conditions. Highly transparent photoanodes and counter electrodes enable highly transparent solar cells with dyes with tunable absorption.^[140] On the other hand, to realize the commercialization of this BIPV technology, it is important to improve device stability and PCE. The stability of dye and electrolyte is generally considered the most challenging aspect.

4.3. Selective Area Light Transmission

Selective UV- or NIR-absorbing semitransparent solar cells based on tunable organic absorbers/dyes can be made color neutral by design. However, they still suffer from stability issues, and the highest LUEs are still substantially lower than the theoretical maximum (PCE of 20.8% at AVT = 100%).^[25] An alternative approach is making use of conventional c-Si solar cells with 100s of microns thick absorber (or theoretically any type of PV) with micro-hole-shaped windows to allow a tunable amount of light to pass through (Figure 8a). Lee et al.^[45] reported such a semitransparent solar cell fabricated using c-Si substrate over an area of

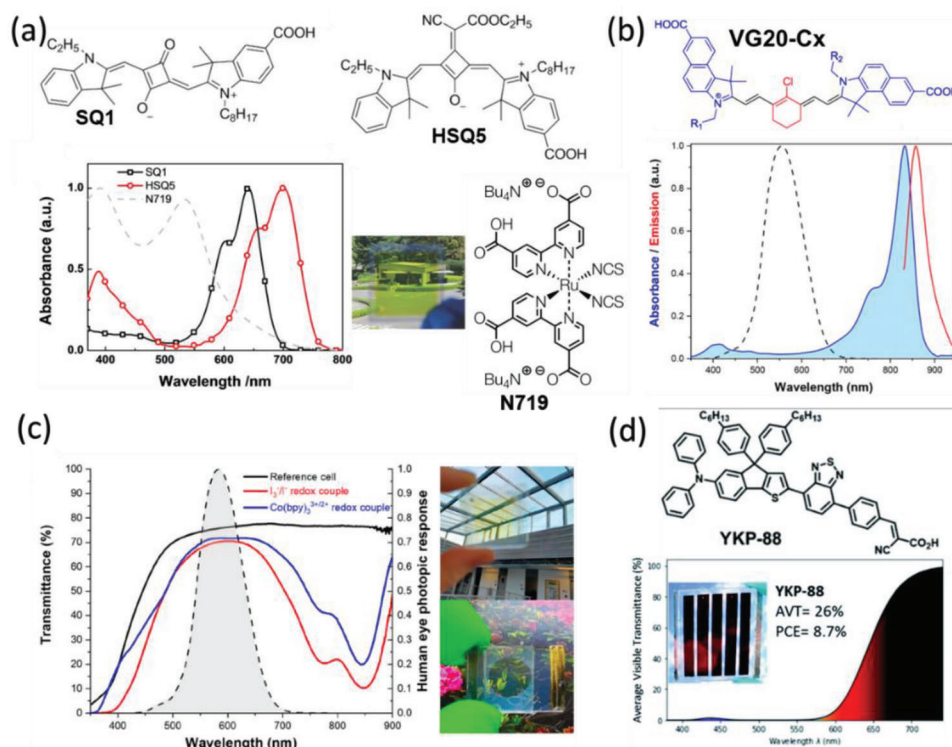


Figure 7. a) Chemical structure and absorption spectra of TiO_2 films sensitized with wavelength selective dyes: SQ1 and HSQ5 and well-known ruthenium dye, N719. Compared to N719 dye, SQ1, and HSQ5 absorb in the NIR region, thus, allowing high AVT. Reproduced with permission.^[136] Copyright 2014 Wiley-VCH. b) General chemical structure of VG20-Cx dye with $R_1 = R_2 = C_{16}H_{33}$, for VG20-C₁₆. Normalized UV–visible absorption spectrum of VG20-C₁₆ in solution (blue shaded curve) and steady-state photoluminescence (red curve) in 9/1 (v/v) ethanol/DMSO solvent mixture (dye concentration $100 \mu\text{mol L}^{-1}$, chenodeoxycholic acid [CDCA] concentration 50mmol L^{-1}). CDCA acts as a de-aggregating agent. VG20-C₁₆ in solution shows an absorption band maximum in NIR with $\lambda_{\text{max}} = 834 \text{nm}$. The fluorescence of VG20-C₁₆ exhibits a sharp emission band at $\lambda_{\text{max}} = 850 \text{nm}$. Human eye photopic response is shown as a black dashed line for comparison with peak eye sensitivity around 550 nm. c) Total cell transmittance of a reference cell without dye and with an optimized electrolyte based on I_3^-/I^- redox couple (black curve) and NIR-selective heptamethine cyanine dye (VG20-C₁₆)-based devices based on the I_3^-/I^- redox couple (red curve) and $Co(bpy)_3^{3+/2+}$ redox couple (blue curve). The human eye photopic response is shown for comparison. Photographs of the transparent NIR-DSSC are also shown: (top) with the I_3^-/I^- redox couple and (bottom) with the $Co(bpy)_3^{3+/2+}$ redox couple. Reproduced with permission.^[47] Copyright 2021, American Chemical Society. d) Transmittance spectrum of an individual cell from the mini-module, along with photographs and performances for the mini-module fabricated with benzothiadiazole-based molecule YKP-88 (the chemical structure is also shown). Reproduced with permission.^[137] Copyright 2021, Royal society of chemistry.

1cm^2 and achieved a high PCE of 12.2% (transmittance, 20%) corresponding to a J_{SC} of 29.2mA cm^{-2} , V_{OC} of 588 mV, and FF of 71.1%. In addition to achieving high LUE, this solar cell remains color neutral (Figure 8b,c) with a predictable PCE versus transmittance relation (Figure 8d). This STPV design with micrometer holes is aesthetically more appealing than stripes of opaque cells with width in millimeters or centimeters.

Jeong et al.^[142] reported a process to make apertures in CIGS thin films using a controlled see-through laser-scribing process. They optimized the fabrication process to demonstrate a monolithically integrated semitransparent CIGS thin-film module (5.25cm^2) with shunt-free apertures, leading to a PCE of 9.38% at an AVT of 18%.

As discussed above in the STPSC section, this approach of achieving transparency via selected area transmission has been applied to PSCs as well. Back in 2014, the Snaith group reported an interesting approach of dewetting perovskite to obtain microstructured arrays of perovskite “islands.” These islands are thick enough to absorb enough light, while the remaining perovskite-free areas transmit light to give a neutral color appearance.^[57]

They achieved PCEs of 8% and 3.5% at AVT of $\approx 7\%$ and $\approx 30\%$, respectively. Recently, Lee et al.^[143] used a “laser patterning approach” in organic–inorganic halide perovskites to control aperture ratios, to fabricate neutral-colored semitransparent PSCs. They achieved a PCE of 12.83% at an AVT of 21.74%. However, laser patterning and etching methods (via electrons or ions) are too harsh for soft absorber materials like perovskites and organic materials and complicate the fabrication process.^[52] Recently, Zhao et al.^[144] have reported a “nonthermal” femtosecond laser ablation approach to reduce ionization, heating, and vaporization damages. Their structured STPSC cell achieved a PCE of 17.5% at an AVT of 18.2%, while a minimodule of $5 \times 5 \text{cm}^2$ area delivered a PCE of 9.1% with an AVT of 37.7%. This approach can be applied to achieve aesthetic artificial patterned solar cells without additional complexity in fabrication.

Although semitransparency can be obtained by leaving gaps in the absorber layer in almost all PV technology, the aesthetic appeal is rather low (especially at close distances), which restricts certain application areas.^[39] Furthermore, adopting these device fabrication approaches adds additional fabrication costs,

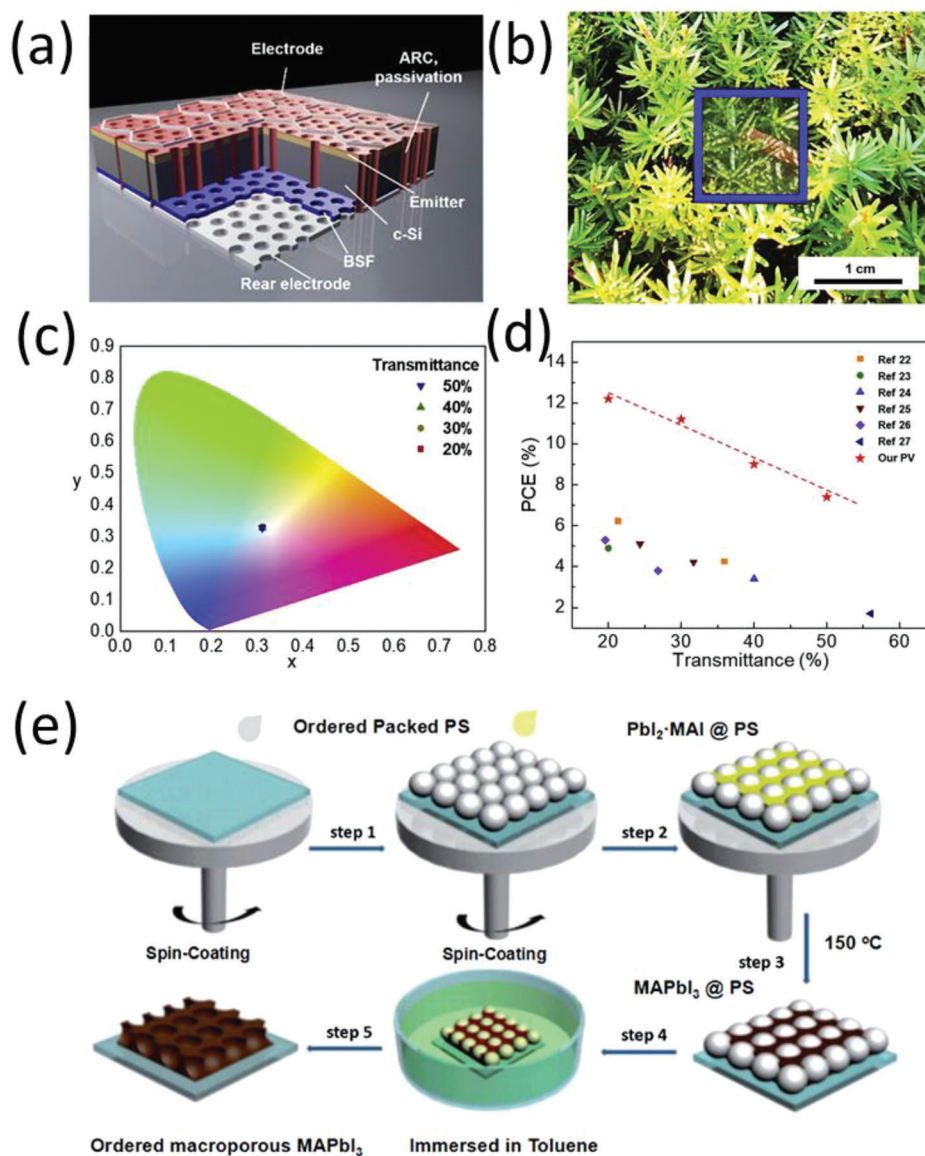


Figure 8. a) Schematic of broadband transparent c-Si solar cells. b) Photograph of the neutral-colored transparent c-Si solar cells (highlighted in a blue square) with a transmittance of 50%. c) CIE 1931 chromaticity color coordinates of the transparent c-Si solar cells with different transmittances. d) Benchmarking the performance (PCE vs AVT relationship) achieved in the study with previously reported neutral-colored transparent photovoltaics. Reproduced with permission.^[45] Copyright 2019, Elsevier. e) Schematic showing the preparation route for macroporous perovskite films on blocking TiO_2 by utilizing a sacrificial polystyrene (PS) template. Reproduced with permission.^[141] Copyright 2016, Elsevier.

which might limit the large-scale adaptation. More research in this area would validate this approach of achieving semitransparency while keeping the fabrication steps simpler.

4.4. STPVs in Tandem Photovoltaics

In tandem solar cells, two or more solar cells are connected in a 4-terminal (4T) or 2-terminal (2T) configuration to efficiently utilize a wider solar spectrum with a wide band top sub-cell and narrow bandgap bottom sub-cell (Figure 9a). The performance of the tandem device depends on the band gap of the top and bottom sub-cells. Figures 9b and 9c, respectively,

show the optimum bandgap combinations in 2T and 4T configurations for maximum theoretical double junction tandem PCEs.

In 4T configuration, the sub-cells are only optically coupled, and they can be optimized independently. At the same time, they utilize two separate substrates (increasing cost) and optical losses are inevitable at the TCE interfaces. In 2T configuration, both electrical (current matching) and optical coupling are important. They need a single substrate and are easy to install compared to 4T configuration. However, a 2T tandem (which is more relevant to STPVs) also needs careful optimization to match the current of the sub-cells, along with processing compatibility between them. Selecting an appropriate recombination layer or tunneling

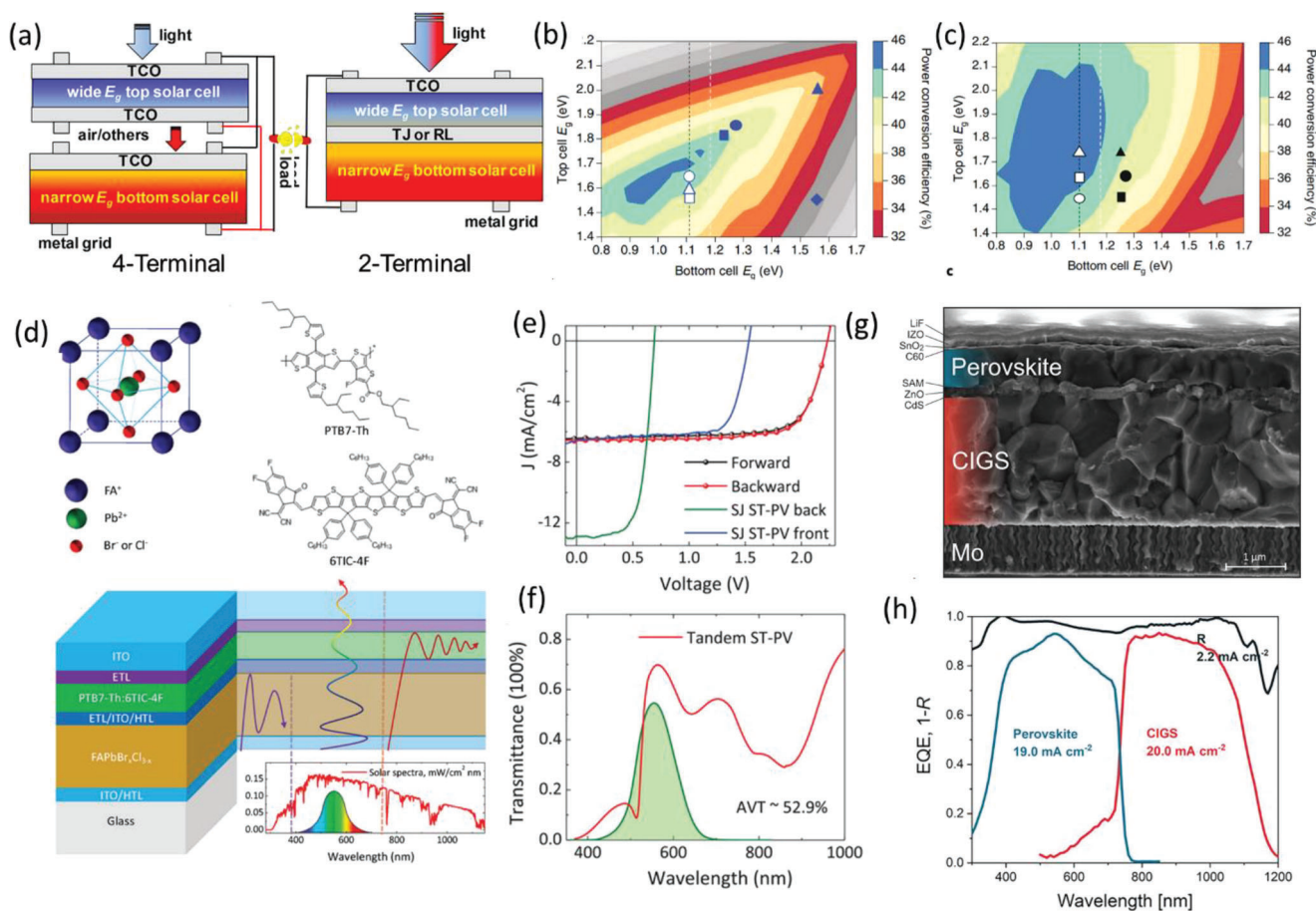


Figure 9. a) Schematic diagrams of 4T (left) and 2T (right) tandem solar cells. Reproduced with permission.^[149] Copyright 2020, American Chemical Society. Theoretical PCEs of 2T (b) and 4T (c) tandem solar cells. Reproduced with permission.^[145] Copyright 2018, Springer Nature. d) An organic-perovskite tandem STPV design, solar spectrum, and photopic response function. Perovskite absorbs lower wavelengths, and the remaining longer wavelengths are absorbed by the organic active layer. The crystal structure of perovskite and the chemical structure of polymer donor (PTB7-Th) and non-fullerene acceptor (6TIC-4F) are also shown. e) J - V curves of tandem STPV and single junction STPV are shown in (d) (blue curve: $\text{FAPbBr}_{3-x}\text{Cl}_x$ perovskite sub-cell; green curve: PTB7-Th:6TIC-4F organic sub-cell). f) Transmittance spectra of the tandem STPV shown in (d). The shaded region represents the human eye's photopic response function. Reproduced with permission.^[146] Copyright 2019, Wiley-VCH. g) Schematic of a monolithic 2T perovskite/CIGS tandem solar cell, superimposed on the cross-sectional SEM image. h) EQE and 1-R spectra for the fabricated tandem device in (g). J_{sc} obtained from the integration of the EQE spectra with AM1.5G spectrum, are also stated. Reproduced with permission.^[147] Copyright 2022, The Authors. Published by the American Chemical Society.

junction with low electrical resistance and low optical loss, is also critical.^[148]

STPVs can also be realized as a combination of different technologies with complementary absorption wavelength regions. An excellent example of this strategy in a series connected 2T tandem device was reported by Zuo et al.^[146] They used an ultra-large-bandgap perovskite layer ($\text{FAPbBr}_{2.43}\text{Cl}_{0.57}$, $E_g \approx 2.36$ eV) for selective absorption in the UV region in combination with a low-bandgap organic bulk-heterojunction layer (PTB7-Th:6TIC-4F, $E_g = 1.27$ eV) with selective absorption in the NIR region. The design of the tandem solar cell is shown in Figure 9d, along with the crystal structure of perovskite and the chemical structures of organic donors and acceptors. They achieved an average PCE of 10.7% (from forward and reverse scans) with an AVT of 52.91% (a record LUE of 5.66%). The LUE of the tandem device was higher than either of the single junction STPSC or STOSC, because of

the improved PCE in tandem without sacrificing too much visible transmittance.

Notably, most of the improvements in the STPV technologies (such as improvements in high-quality thinner absorber layers and TCEs, and so on) are also relevant to tandem solar cells focusing on maximizing the PCE in a double- and triple-junction solar cell.^[149] The SQ limit for single-junction solar cells with a bandgap of 1.34 eV is 33.7%, while those for two- or three-junction solar cells are 46% and 50%, respectively.^[150,151] Because of their large market share and record PCE of 26.7%, Si solar cells are the most suitable bottom cells in tandem solar cells for top absorber layers in combination with tunable and wider band gap (such as perovskites, OSCs, CIGS, or DSSCs).^[147,149,152–154] Furthermore, the absorber materials with tunable bandgap can act as both front and bottom sub-cells in a tandem configuration. For all perovskite (perovskite/perovskite) tandem solar cells, a

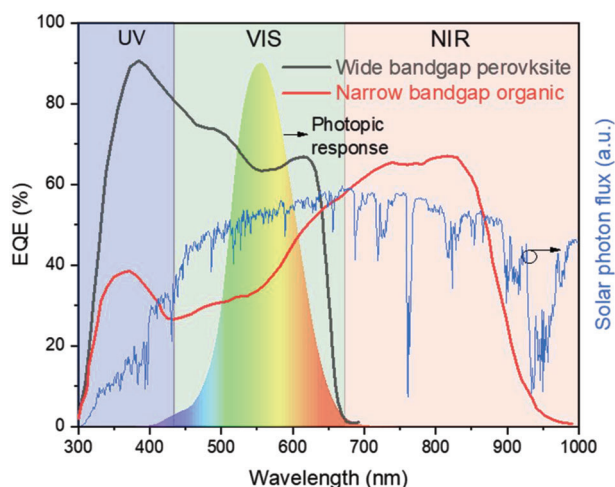


Figure 10. A comparison between typical absorber layers of STOSCs and STPSCs, the two STPV technologies with the highest LUEs. The EQE spectra for STOSC and STPSC were adapted from Huang et al.^[131] and Wang et al.^[113] STOSC spectrum: Reproduced with permission.^[131] Copyright 2022, The Royal Society of Chemistry. STPSC spectrum: Reproduced with permission.^[113] Copyright 2021, Wiley-VCH.

record-high PCE of 28.5%^[153] and for perovskite ($E_g = 1.79$ eV)/organic ($E_g = 1.79$ eV) 23.6%^[152] have been reported in the last couple of years. Jošt et al.^[147] demonstrated a monolithic 2T Perovskite (1.68 eV)/CIGS (1.1 eV) tandem device with a certified PCE of 24.2% with a potential to reach a PCE of 32% (the complete device structure is shown in Figure 9g). One aspect of improvement would be the current matching between the top and bottom sub-cell, which was currently limited by the perovskite top cell (Figure 9h).

The structure of a tandem STPV solar cell seems more complicated due to the optimization needed for the interconnection/tunneling layer between the sub-cells, but if the PCE is improved without losing the AVT, it seems a feasible strategy.^[148,155–157]

STPSCs have the highest LUEs among all single-junction STPV technologies (even though the record opaque cell PCE has barely reached 20%). It is therefore imperative to analyze the relative advantages of organic solar cells vis-à-vis other absorbers for STPV applications. It should only be fair to compare the absorption (EQE) region of a high LUE STOSC device with that of a high LUE STPSC device (STPSCs have the second highest LUE among all STPVs). Polymer donors and small molecule NFA are the necessary constituents of the organic absorber layer, and therefore, the absorption spectrum can be easily tuned to realize both narrow-bandgap donor and narrow-band acceptor, with absorption maxima in the NIR region. Usually, the polymer donor has more absorption in the visible region compared to the acceptor; thus, AVT can be further maximized by reducing the donor amount in the active layer. This results in a high EQE in the NIR and UV region and a low EQE in the visible region (as shown in Figure 10).^[122,131,158] On the other hand, perovskite is approximately a broadband absorber, and the visible wavelength absorption can only be minimized by reducing the thickness or increasing the bandgap.^[113] The gain in J_{SC} due to absorption in the NIR region overcompensates for the loss in V_{OC} due to a lower bandgap in STOSCs. STDSSCs, in principle,

can benefit from the tuned wavelength-selective absorption given their performance in traditional device structures is improved further to match those of OPVs. Moreover, a standard opaque high-performance perovskite solar cell (or even a-Si:H, CIGS, CdTe for that matter) utilizes a sub-micrometer thick (>300 nm) absorber while ≈ 100 nm is the typical thickness of active layer in high PCE OPV devices. This means the typical shunt losses (encountered due to pinhole-prone thinner absorber layers in STPSCs) are not usually a challenge in STPSCs. A typical STOSC device uses ≈ 70 – 80 nm thick absorber layer without significant loss in FF or V_{OC} (as reported elsewhere).^[122,131,158]

5. Device Engineering in STPVs

It is common in the literature to find a finite set of buffer/charge transport materials, passivation techniques, etc., which appears exclusive to a particular STPV technology. Since the STPV technology is not mature yet and none of the existing reports has found the “perfect” device architecture (combining low cost, high LUE, long-term stability, and visual appeal), researchers working on the development of STPVs to achieve high LUEs and the research community in the broader context would benefit from the incremental improvements in either of the STPV technologies. For example, a low-temperature buffer layer recipe would benefit both established thin-film technologies as well as organic and perovskite solar cells. Similarly, a Bragg reflector optical engineering could tune the color and reflectivity of any STPV technology. In this section, we focus on potential candidates for functional layers that would benefit the design of high-LUE STPV devices based on different technologies.

5.1. Transparent Conductive Electrodes

Transparent conductive electrodes (TCEs) are critical since they influence the PCE, AVT, CRI, stability, and cost of semitransparent solar cells. Several categories of materials, including TCOs, metals (including metal nanowires and grids), polymers, and carbon materials, have been used to replace the opaque electrodes (plots of optical transmittance and transmittance vs sheet resistance of these categories of TCEs are shown in Figure 11). To evaluate the performance of a transparent electrode, a figure of merit is often used, such as one used by Rowell and McGehee:^[159]

$$\frac{\sigma}{\alpha} = \frac{1}{R_{sh}} = -\frac{1}{R_{sh} \ln T} \quad (4)$$

where σ is the DC conductivity, α is the absorption coefficient, R_{sh} is the sheet resistance, t is the thickness, A is the absorbance, and T is the transmittance.

Transparency in the NIR region also becomes important in cases where the active layer utilizes the near NIR spectrum while transmitting visible light (case of wavelength-selective semitransparent solar cells). Furthermore, work function mismatch between the transparent electrode and semiconductor functional layers can result in Schottky contact, which leads to high series resistance and lower efficiency.^[161]

Additional considerations while selecting a TCE are related to the processing compatibility with the STPV technology. These

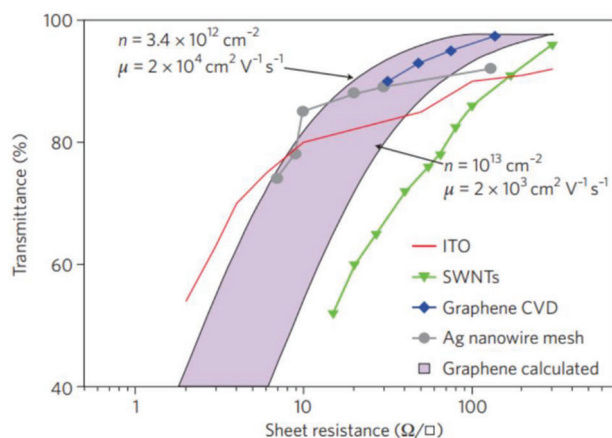


Figure 11. Transmittance versus sheet resistance for different transparent conductor materials. Reproduced with permission.^[160] Copyright 2010, Nature Publishing Group.

include suitable processing temperature, inertness, interface formation with the adjacent layer, and stability during device fabrication.^[162] Therefore, a certain transparent electrode would not apply universally to all the STPVs, although it has a high figure of merit. For example, limited post-processing is possible on conductive polymer electrodes because of low thermal and chemical stability. Hence, they are used as top electrodes in most applications.

5.1.1. Transparent Conductive Oxides

ITO, deposited primarily via sputtering, is the most widely used transparent conductive oxide and is even used in commercial devices.^[163] However, high cost, degradation at processing temperatures >500 °C, and chemical instability have increased research interest in its alternatives such as FTO, AZO, and gallium-doped zinc oxide.

When TCOs are not used as substrates (glass/FTO or glass/ITO) but as the top layers, their deposition can damage the underlying layers because of the ion bombardment or high temperature, especially when the underlying layer is organic.^[164,165] In STOSCs, an inorganic buffer layer (such as MoO_x or Ag thin-film) can be deposited before the TCO sputtering.^[165,166] Furthermore, some alternative ways of reducing the sputtering damage (such as by reducing the sputtering power and changing the geometry) have also been reported.^[167,168]

Although TCOs are generally attractive as the semitransparent electrode at the laboratory level, they would add immensely to the production cost, particularly for vacuum-deposited ones.^[169] However, some promising results have been reported with amorphous TCO electrodes. Lim et al.^[111] reported a room-temperature processed amorphous InGaTiO (IGTO) electrode prepared by modified sputtering geometry (linear facing target sputtering). The electrode showed high transmittance of 87.5% and low sheet resistance of $9.9 \Omega \text{ sq}^{-1}$. The modified geometry also avoided the plasma damage which is common during sputtering. With an IGTO electrode, a PCE of 15.6% with an AVT of 10.5% was obtained for an optimized $\text{Cs}_{0.175}\text{FA}_{0.825}\text{Pb}(\text{I}_{0.875}\text{Br}_{0.125})_3$ perovskite, compared to a PCE of

16.4% for the opaque thermally evaporated Ag electrode. Furthermore, a “two-step facing target sputtering” method was used to deposit indium/zinc co-doped In_2O_3 (IZTO) top electrode in a low-temperature plasma-damage-free deposition. An impressive LUE of 3.36 (PCE = 13.26%, AVT = 24.7%) was reported. Meanwhile, the sputtered ITO electrode showed poor performance (PCE = 3.43%).^[170]

5.1.2. Ultrathin Metals

Thin metallic films (≈ 60 – 100 nm) are commonly used in OSCs and PSCs as top electrodes. In traditional thin film solar cells (a-Si:H, CdTe, CIGS), they are usually the current collectors patterned in grid form. In semitransparent solar cells, ultrathin metals (mostly Ag, Au, or Cu) of thickness <20 nm can be deposited through physical vapor deposition to work as semitransparent electrodes. This approach offers the simplest transition from opaque to semitransparent devices because the deposition conditions and interfaces remain essentially the same. Bai et al.^[171] used thermally evaporated 15 nm Ag or Au and reported one the highest LUEs among the STOPVs (PCE of 12.88% with AVT of 25.60% and CRI of 97.6). Ultrathin metals have been applied in STPSCs too.^[163,172,173]

There exists a significant trade-off between transparency and conductivity for thin metal films. Therefore, light management techniques can be used in combination with the ultrathin metal electrodes to enhance the absorption or transmission region in the absorber layer. Dielectric-metal-dielectric (DMD) is such an improved application of ultrathin metal electrodes, which enhances the stability, transmission, and infrared reflectance.^[107] For example, a multilayered anode structure ($\text{MoO}_3/\text{Ag}/\text{MoO}_3$) can be used as the hole-collecting electrode. The inner MoO_3 layer acts as a hole transport/buffer layer to improve hole collection and the outer MoO_3 layer serves as a light OC layer to enhance the transmittance of the device.^[174] Additionally, this multilayered structure solves the wetting issue encountered while depositing an ultrathin metal layer, and therefore, no seed layer is required. A DMD anode can tune the aesthetics (color coordinates, CRI, and CCT) of the STPV device.^[124] The light management engineering approach to modulate reflection and transmission wavelength regions is discussed later in this review.

High conductivity, ductility, and easy scalability favor metal electrodes. However, the high cost of material (especially for Au) and vacuum-based deposition method to control the precise thickness hinder their widespread commercial application.

5.1.3. Metal Nanowires and Grids

Metal nanowires (especially silver nanowires, AgNWs), due to their high conductivity, transparency (sheet resistance below $\approx 10 \Omega \text{ sq}^{-1}$ while transmittance reaching 80%, similar to ITO),^[175] flexibility, and easy solution-processability, would be a good choice for transparent electrodes.^[24] Particularly, solution-processability makes them attractive as cost-effective alternatives to ultrathin metal films.

AgNWs are typically synthesized by the reduction of silver nitrate precursor dissolved in ethylene glycol containing halide ions

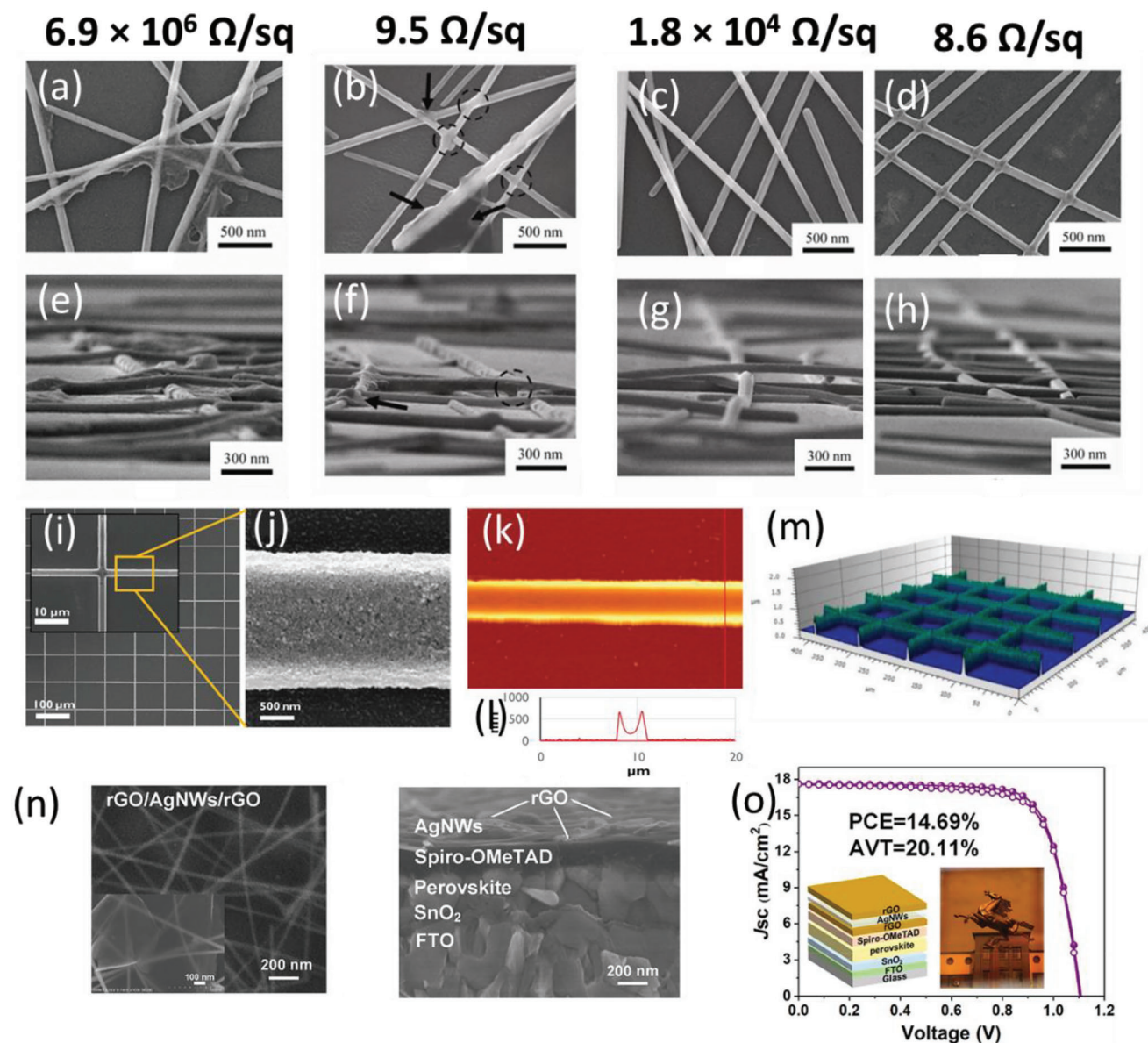


Figure 12. SEM images of AgNWs with various treatment conditions: a,e) Air-dried (sheet resistance of $6.9 \times 10^6 \Omega \text{ sq}^{-1}$). The AgNWs fabricated by polyol method were dispersed in ethanol and drop coated on glass. Residual polyvinylpyrrolidone (PVP) from synthesis at the junctions between AgNWs and therefore weak connections between the AgNWs can be seen. b,f) Air-dried and heated at 200°C for 20 min (sheet resistance of $9.5 \Omega \text{ sq}^{-1}$). Melting and fusion of AgNWs can be observed along with residual PVP. Residual PVP did not burn away but nearly melted. c,g) Air dried and water-ethanol rinsed (sheet resistance of $1.8 \times 10^4 \Omega \text{ sq}^{-1}$). No PVP residues after rinsing in water and ethanol (instead of heat treatment at 200°C) and weak connections of the AgNWs can be observed. (d,h) Air-dried, water-ethanol rinsed, and pressed at 25 MPa for 5 s (sheet resistance of $8.6 \Omega \text{ sq}^{-1}$). No PVP residues and tightly connected AgNWs with smooth surfaces can be observed. Reproduced with permission.^[176] Copyright 2019, Wiley-VCH. Panels (i) and (j) show the SEM of the printed grid after hotplate sintering. AFM image of the same is shown in (k) along with the cross-sectional (l). Also, a 3D projection of the Ag grid is shown in (m). Reproduced with permission.^[177] Copyright 2011, Tsinghua University Press and Springer-Verlag Berlin Heidelberg. n) SEM top view of rGO/AgNWs/rGO based devices (left) and corresponding cross-section morphologies (right). o) Photograph of the semitransparent perovskite solar cell and J - V curves of the optimal device for the STPSCs using rGO/AgNWs/rGO as the top electrode. Reproduced with permission.^[178] Copyright 2020, Elsevier.

(Cl^- , Br^-). Polyvinylpyrrolidone (PVP) is used as the stabilizing agent.^[179–181] AgNWs have diameters in the range of $\approx 100 \text{ nm}$ and lengths in the range of tens of μm . The net resistance of AgNW electrodes depends on the length, diameter, wire density, and junction resistance (at the intersection of nanowires).^[182] The effect of junction weld between the wires was illustrated by

Tokuno et al.^[176] and can be visualized in **Figure 12a–h**. The sheet resistance of the AgNW electrodes decreased by several orders of magnitude by selecting an appropriate post-deposition treatment: thermal annealing, rinsing in ethanol, or mechanical pressure. These modifications are aimed at improving the connectivity between the wires and the removal of organic impurities.

Sometimes metal nanoparticles are printed in a mesh/grid pattern (using lithography or printing techniques) with tunable transparency and conductivity.^[183] For example, a scalable printed grid electrode using silver nanoparticles with a sheet resistance of $43 \Omega \text{ sq}^{-1}$ and average transmittance of 93% was reported by Abbasi et al. (dimensions are shown in Figure 12i–m).^[177] Saive et al.^[184] designed 3D microscale grid fingers with triangular cross-sections to achieve transparency up to 99.9% and very low sheet resistance of $4.8 \Omega \text{ sq}^{-1}$.

Guo et al.^[185] used AgNWs to fabricate semitransparent perovskite cells with an efficiency of 8.49% and AVT of 21.5% (compared to 9.19% for reference devices with opaque reflective electrodes). Gahlmann et al.^[186] used AgNWs as top electrodes in semitransparent perovskite solar cells to obtain an AVT of 16% and a PCE of 17.4%, a record for semitransparent p-i-n PSCs with an AgNW top electrode. Another high LUE (PCE = 14.69% and AVT = 20.11%) device was reported by Dou et al.^[178] using a sandwich structure top electrode (reduced graphene oxide (r-GO)/AgNW/r-GO). The top view and cross-section SEM of the composite electrode are shown in Figure 12n, and the photograph of the STPSC device, along with the J - V curve, is shown in Figure 12o.

Margulis et al.^[187] used a spray-deposited AgNW electrode in combination with spin-coated PEDOT:PSS [poly(3,4-ethylenedioxythiophene):poly(styrenesulfonate)] as the semitransparent counter electrode (transparency >90% in the visible region) in solid state-DSSC. With this solution-processed composite electrode, they reported similar efficiencies compared to an evaporated top electrode: 3.6% for AgNW-based and 3.7% for 200 nm Ag electrode. However, AVT was not mentioned in the work.

With continued improvements in the processing of AgNW electrodes, they have reached the threshold of $\approx 90\%$ transmittance at 550 nm and sheet resistance $< 20 \Omega \text{ sq}^{-1}$ (comparable to commercial ITO or FTO electrodes).^[185] Sun et al.^[188] replaced bottom ITO and top Ag contacts with AgNWs and achieved excellent performance of 11.9% in a fully solution-processed device, compared with 15.2% for the reference ITO/Ag-based devices.

Although metal nanowires and grids represent solution-processed alternatives to the traditional TCO electrodes, incompatibility with the underlying interfacial layers, poor adhesion, and high roughness limit their widespread implementation in STPVs.^[189,190]

Furthermore, degradation in the performance of devices using AgNW electrodes over time under the influence of light and humidity and increased chemical reactivity call for more studies on its long-term stability.^[189] There has indeed been considerable focus on overcoming the roughness, stability, and compatibility issues (like wetting, mechanical flexibility, etc.) via a composite strategy with metal oxide nanoparticles,^[185,191,192] polymers,^[193,194] MXene/graphene,^[195–197] and so on. The high cost of Ag also calls for research into alternatives such as CuNWs, but the issue of severe oxidation remains a challenge.^[198,199]

5.1.4. Conductive Polymers

Although an order of magnitude lower in conductivity than the thin metal films, the most common conductive polymer elec-

trode, PEDOT:PSS, offers easy solution-processability and mechanical flexibility. Hu et al.^[200] used PEDOT:PSS as the top electrode to achieve an impressive PCE of 12.5% (with 30.6% AVT) compared to 20.6% with opaque metal electrodes.

Many reports have been published related to the research on enhancing the conductivity of PEDOT:PSS by post-treatment.^[203–205] An impressive conductivity of $>4000 \text{ S cm}^{-1}$ was reported by Kim et al.,^[201] achieved simply via H_2SO_4 treatment. The treatment also modified the surface adhesion properties, which allowed an easy “pick-and-place” transfer to any substrate (including glass, silicon wafer, Cu foil, Kapton tape, or PET) using elastomeric carrier stamps (like polydimethylsiloxane, PDMS). A simplified scheme is shown in Figure 13a.

Another promising hybrid electrode, polymer:Ag (PA), consists of an ultrathin Ag layer covered by PEDOT:PSS. PEDOT:PSS also acts as an anti-reflection layer. Polyethyleneimine (PEI) is coated on the substrate as a nucleation inducer to prevent island formation in Ag ultrathin film (refer to Figure 13b for scheme).^[202] The performance of OSC with this composite electrode (PCE = 8.6%) was at par with that of ITO (PCE = 8.9%) in opaque devices. Furthermore, this PA electrode was used as the bottom transparent conductive electrode along with H_2SO_4 -treated PEDOT:PSS (H-PEDOT) as the top electrode in a flexible STOSC (device structure shown in Figure 13c). They reported a PCE of 4.9% with an AVT of 38%. In addition, both these electrodes (PA and H-PEDOT) exhibited excellent mechanical durability compared to the rigid and brittle ITO electrodes (Figure 13d). Recently, Park et al.^[204] demonstrated all solution-processed STOPV devices with a PEDOT:PSS/ionic liquid (IL) composite as a top electrode to fabricate an efficient STOSC with a PCE of 6.32% at an AVT of 35.4%. A “conductivity and flexibility enhancer” (CFE), zinc di[bis(trifluoromethylsulfonyl) imide] ($\text{Zn}(\text{TFSI})_2$) was used to enhance the conductivity and bendability of PEDOT:PSS:CFE electrode (sheet resistance of $22 \Omega \text{ sq}^{-1}$ vs $10 \Omega \text{ sq}^{-1}$ for ITO).^[200] In a flexible STPSC, using PEDOT:PSS:CFE as both bottom and top electrodes, they obtained a PCE of 9.7% with AVT of 30.6%.

In DSSCs, glass/Pt has been exclusively used as the counter electrode because of its excellent electroactivity for the I_3^-/I^- redox couple, although the Pt electrode accounts for as high as 40% of the cost of the whole device and also suffers from high reflectivity.^[138,206] Conductive polymers are seen as promising alternatives; conductive polyaniline (PANI), with emerald greenish appearance and transparency (transmittance 74% at 510 nm wavelength for a 250 nm thin PANI film), is among the most studied ones and is promising for STDSSCs.^[207] Park et al.^[208] reported a DSSC solar cell using porous polyaniline nanotubes (PPNT-1) as a counter electrode and achieved a higher PCE of 5.57% versus the usual Pt counter electrode (PCE = 5.20%). PPNT-1 showed lower charge transfer and higher electrocatalytic activity compared to Pt. Wang et al.^[209] used an oriented polyaniline random network cathode to increase the PCE of DSSC solar cell up to 8.24% (J_{SC} of 15.09 mA cm^{-2} , V_{OC} of 0.78 V, and FF of 0.70), even higher than the efficiency (6.78% with $J_{\text{SC}} = 13.11 \text{ mA cm}^{-2}$, $V_{\text{OC}} = 0.76 \text{ V}$, FF = 0.68) of the DSSC with the Pt cathode. The PANI nanowires array displayed higher electrocatalytic activity (lower charge transfer resistance, R_{ct}) on the Co(iii)/Co(ii) redox couple than random PANI network or even Pt electrode, and thus higher J_{SC} and FF. Even in thin PANI film,

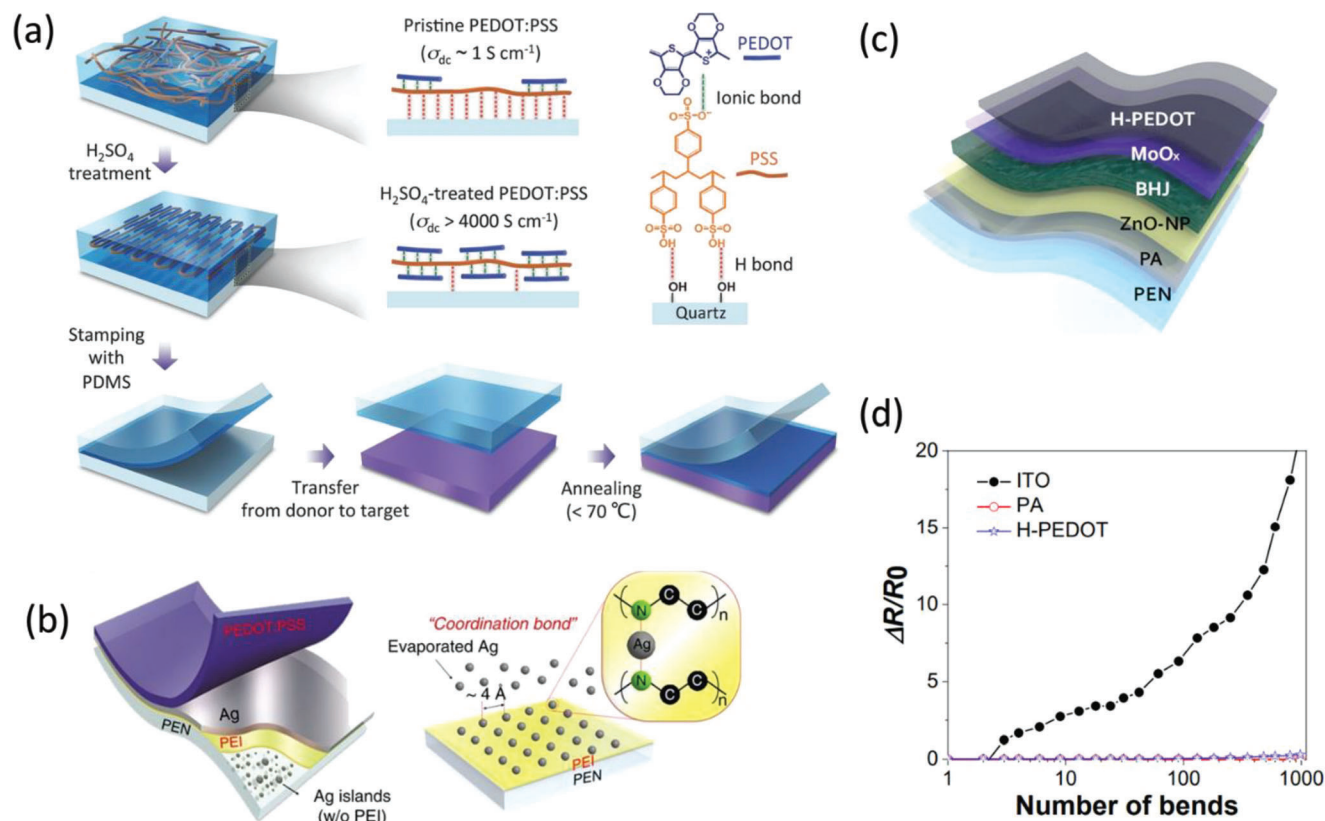


Figure 13. a) Schematic illustration of the procedure for the transfer printing of transparent H_2SO_4 -treated PEDOT:PSS film from a donor quartz substrate to another target substrate. Reproduced with permission.^[201] Copyright 2015, Wiley-VCH. b) Conceptual diagram for the growth mechanism of the Ag film with the PEI nucleation inducer. Reproduced with permission.^[202] Copyright 2015, The authors. c) Schematic illustration of the flexible semitransparent OPV architecture. d) Resistance change as a function of the number of bending cycles for ITO, PA, and H-PEDOT flexible electrodes with a bending radius of 5 mm. Reprinted with permission.^[203] Copyright 2020, American Chemical Society.

which was in situ polymerized on FTO, the porosity of PANI was quite high, resulting in higher electrocatalytic activity than the Pt counterpart in a semitransparent DSSC device.^[210] Nevertheless, the AVT values for these DSSC devices were not reported, so the LUEs of cells with PANI or Pt electrodes could not be directly compared.

Conductive polymer electrodes are compatible with low-cost solution-based roll-to-roll processing on flexible substrates.^[211] However, thermal and chemical stability of these electrodes are questionable, thus limiting their use to low lifetime or indoor applications. PEDOT:PSS might degrade by moisture absorption, or even the underlying layers could be corroded by acidic PEDOT.^[161]

5.1.5. Carbon-Based Electrodes

Carbon-based electrodes, specifically graphene and carbon nanotubes (CNTs), have favorable properties such as high chemical stability, low cost, high transparency, and mechanical flexibility. Graphene is a 2D material ($\approx 0.34 \text{ nm}$ thick) composed of sp^2 -carbon with high electron mobility in the order of $10^5 \text{ cm}^2 \text{ V}^{-1} \text{ s}^{-1}$ with high transmittance of $>97\%$ for a single layer (electronic band structure is shown in **Figure 14a–c**).^[212,213] The de-

tailed description of the optoelectronic properties can be found elsewhere.²⁰²

CNTs are 1D materials (diameters of 0.7–20 nm) formed by winding graphene sheets to form single-walled CNTs (SWCNTs), double-walled CNTs (DWCNTs), or multi-walled CNTs (MWCNTs) (**Figure 14e,f**). SWCNTs can display metallic or semiconducting properties based on the chiral vector, $C_n = na_1 + ma_2$ where a_1 and a_2 are unit cell vectors of the graphene lattice, and n and m are integers (**Figure 14d**).^[214] The chemical structure and simplified description of graphene and CNTs are shown in **Figure 14a–f**.

The most common methods for the fabrication of graphene conducting films include mechanical exfoliation, epitaxial growth, chemical vapor deposition (CVD), reduction of graphene oxide.^[216] Large-area uniform graphene films can be prepared by CVD or PECVD.^[217]

Song et al.^[218] demonstrated a semitransparent organic solar cell with a graphene electrode as the anode, cathode, or both (ITO/PEDOT:PSS/ZnO/PDTPDFBT:PCBM/ MoO_3 /graphene or Al). Replacing the bottom cathode ITO with graphene resulted in comparable performance (5.9% vs 5.8%, respectively). At the same time, replacing the top anode Al with graphene resulted in slightly lower PCE (4.2%), mainly due to lower J_{SC} because of the loss of the reflected light from the Al electrode. Finally,

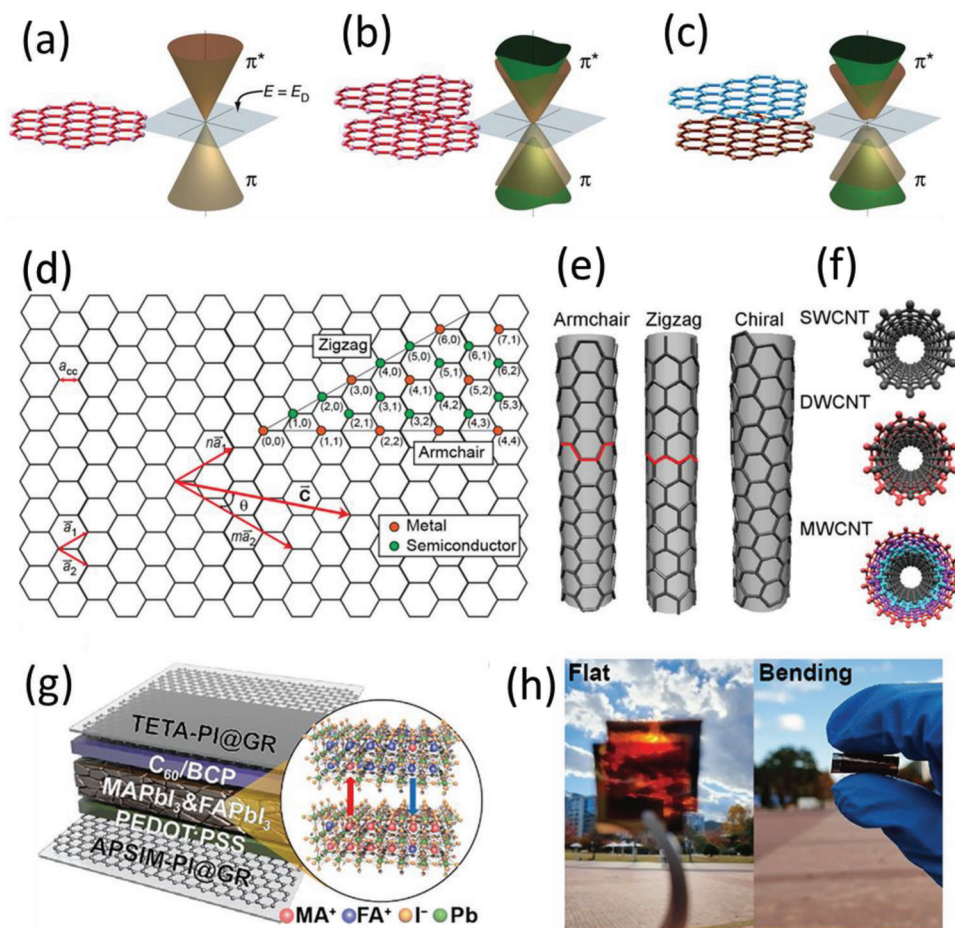


Figure 14. Electronic band structures of graphene in a) single, b) symmetrically double, and c) unsymmetrically double layer forms. Reproduced with permission.^[212] Copyright 2006, The American Association for the Advancement of Science. d) Unrolled SWCNT describing the chiral vector C ; values of the integers n and m determine the metallic/semi-metallic nature. e) Illustration depicting the direction of the chiral vector, which affects the appearance of the nanotube. (4,4): armchair shape, (6,0): zigzag shape, and (5, 3): chiral shape; and f) “Ball and Stick” model of single-walled CNT (SWCNT), double-walled CNT (DWCNT), and multi-walled CNT (MWCNT). Reproduced with permission.^[214] Copyright 2016, American Chemical Society. g) Schematic image and h) digital image of the device based on polyimide-integrated graphene electrodes ((PI@GR)-based ST-bifacial cation-exchanged PSCs). Reproduced with permission.^[215] Copyright 2022, American Chemical Society.

STOSC devices using graphene cathode-graphene anode yielded a PCE of 4.0% at an impressive AVT of 54%. Liu et al.^[219] reported a STOSC with graphene transparent electrodes as both cathode and anode with PCE up to 3.4% from both sides. It has average transmittance of $\approx 40\%$ in the visible region with a neutral color appearance. Neutral-colored STOPVs are quite attractive for power-generating windows.

Tran et al.^[220] replaced the bottom electrode of a semitransparent perovskite solar cell with graphene (PES/graphene/ NiO_x /MAPbI₃/PCBM/AZO/Ag/AZO) and achieved a PCE of 14.2% with a transmittance of $\approx 26\%$ at 700 nm (AVT of 13.7%). Polyimide-integrated graphene (PI@GR) electrodes have also shown high performance in flexible STPSC with AVT of 18% and PCE of 15.1%. In an unconventional device fabrication method, two half-cells containing perovskite (MAPbI₃ and FAPbI₃) films, both on PI@GR electrodes, were laminated to obtain high-quality and stable α -phase FAPbI₃ (Figure 14g,h). You et al.^[221] laminated a transparent graphene electrode on the top of a semitransparent perovskite solar cell

(average transmittance = 5.84%) and achieved PCEs close to that with the Au electrodes (12.02 ± 0.32 vs $13.62 \pm 1.00\%$ for graphene and Au electrodes, respectively). Notably, when illuminated from the graphene side, the devices still showed a high PCE of $11.65\% \pm 0.35\%$.

Graphene as a nanolayer electrode has also been applied in CIGS and CdTe solar cells, though mostly in opaque solar cells.^[222–224]

The most common fabrication methods for CNTs are plasma arc discharge, pulsed laser evaporation, and CVD. These processes typically use a carbon source and a metal catalyst, and the growth conditions dictate the property distribution of the SWCNTs. Also, during growth, additional nanotube layers might encapsulate the existing SWCNT to form MWCNTs. It is also important to note that the optoelectronic properties of MWCNTs are a combination of the properties of the constituent SWCNTs and given the variability in the optoelectronic properties of SWCNTs produced by most synthesis techniques, it necessitates either a) growing single-chirality SWCNTs or b) using purification

methods to separate the SWCNTs by electronic type (metallic or semiconducting), dimension, or chirality. Besides, as a result of the fabrication methods, the as-synthesized CNTs often exist as aggregates or bundles.^[225] For application in solar cells as either transparent conductive electrodes or even HTLs, CNTs are dispersed in a suitable solution using dispersing agents.^[214,222,226,227]

Jeon et al.^[228] used SWCNTs synthesized via CVD as the top electrode in an organic solar cell (ITO/ZnO/PTB7:PCBM/MoO_x/CNT) and achieved a PCE of 1.8% as compared to the opaque reference device 7.8%. To reduce such a significant loss, they p-doped the SWCNTs using concentrated HNO₃ to increase the efficiency to 3.7%, with AVT close to 30%.

Contreras et al.^[229] used a thin film of a randomly distributed network of SWCNTs (spray-coated from an SWCNT ink dispersion) as the transparent top contact in CIGS solar cells with device structure Mo/CIGS/CdS/i-ZnO/SWCNT. Using the SWCNT top electrode, they achieved a PCE of 12.98% ($V_{OC} = 0.674$ V, $J_{SC} = 31.21$ mA cm⁻², FF = 61.66%), while PCE of the reference solar cell (Mo/CIGS/CdS/i-ZnO/ZnO:Al) was 19.5% ($V_{OC} = 0.694$ V, $J_{SC} = 35.34$ mA cm⁻², FF = 79.4%). Although SWCNT film offers sufficient semitransparency, its porous nature and high surface roughness introduces a shunt path between the metal grid and the layer beneath SWCNT film, thus, lowering the FFs. Barnes et al.^[230] used the SWCNT networks in CdTe solar cells as a replacement for ITO top electrode and achieved a PCE of 12.4% with 40–50% transmission in the range 800–1500 nm. The used device structure was Glass/Cd₂SnO₄/ZnSnO_x/CdS:O/CdTe/Cu_xTe/SWCNT or ITO, with the reference ITO device reaching a PCE of 13.9% and similar transparency. Although both the devices discussed above did not qualify as STPV, it is possible to reduce the thickness of the absorber layer in combination with transparent bottom contact to tune the transparency, as reported elsewhere.^[231–233,73,75]

Carbon-based electrodes have positive attributes such as environmental stability, hydrophobicity, and suitable work function (they can also work as a hole-selective layer).^[227] However, the high processing cost to obtain high-purity (low-yield) defect-free CNTs make them unviable for large-scale implementation.^[226] Similar complexity exists in processing devices with graphene electrodes.^[218] FFs using graphene and CNT electrodes are lower than those with the TCO counterparts such as ITO. Because of the roughness and discontinuity/voids, all the interfaces with these electrodes impact the device performance and need smoothing/passivation strategies to reduce shunt losses. To this end, surface modification of graphene has indeed shown promising results.^[234] Xu et al.^[235] modified the graphene surface using ethylene glycol (EG) to endow active sites for the subsequent atomic layer deposition (ALD) of ZnO ETL. Thus, they improved the performance of a perovskite solar cell by 134% compared to the bare graphene electrode. More importantly, scaling up these electrodes while maintaining uniform conductivity has been quite challenging.

Transparent conductive oxides (TCOs) have the optimum balance between optical transparency, conductivity, and stability. However, high deposition costs and raw material scarcity (in the case of ITO) limit their widespread application. Damage to underlying layers during high-impact processes like sputtering is also a concern for soft absorber materials like polymers and per-

ovskites. Ultrathin metal films lead to significant losses in J_{SC} due to high absorption in the visible region. They also employ costly vacuum-based deposition methods. At the same time, their application is quite straightforward by reducing the thickness of the opaque top electrode. Solution-processed metal nanowires have excellent tunable transmittance/conductivity, but they suffer from roughness and adhesion issues. Thus, they need additional surface modification steps. Furthermore, the chemical stability of nanowires (especially, AgNWs) has been a matter of concern. Metal meshes and grid patterns require complex preparation processes involving photo- or nanoimprint-lithography and do have similar stability and roughness issues as metal nanowires. Graphene and CNTs have the potential to be the TCE of choice if the conductivity is further enhanced and coating methods are standardized. Polymer electrodes are famously unstable at high temperatures and humidity but are quite competitive for flexible, low-cost, or indoor photovoltaics. In summary, each of these TCEs is unique in its optoelectronic properties, processing complexities, stability, application flexibility, and so on. The device structure, fabrication conditions, and end-use would dictate whether a TCE is suitable for a specific STPV device.

5.2. Carrier Transport Layers and Buffer Layers

A solar cell consists of several layers apart from the absorber and contacts to enhance the charge collection efficiency once the free carriers have been generated by photoexcitation. These additional layers are generally called buffer layers or charge transport layers, depending on the convention of the respective PV technology. A perovskite solar cell, for example, adopts an n-i-p (or p-i-n) architecture, where n, i, and p represent an n-type layer, intrinsic perovskite absorber layer with low doping density, and a p-type layer, respectively. **Figure 15** shows the simplified device structures of the six types of STPV technologies discussed in this review.

It is not straightforward to generalize the role of electron and hole transport/buffer layers used in different solar cell technologies, though some parameters can be generalized. ETL (an n-type material) should possess: 1) high electron mobility, 2) wide bandgap, and 3) ideal band alignment with the conduction band of the adjacent layers. Similarly, an HTL (p-type material) should be able to transport holes (and/or block electrons) to the counter electrode with desirable properties such as: 1) matched valence band level and 2) high hole mobility, along with 3) stability and compatibility with the underlying layers. Moreover, the parasitic absorption in the charge transport or buffer layers should be minimized. For example, wide bandgap metal oxides (TiO₂, ZnO, MoO_x, etc.) are quite transparent in the visible region. At the same time, the most common HTL in perovskite (spiro-OMeTAD) has an absorption peak at 400 nm and therefore contributes to significant J_{SC} loss.^[236]

ST-amorphous silicon solar cells consist of a p-i-n a:Si:H structure (which forms the p-n junction diode) sandwiched between two transparent conductive oxides. These oxides are usually aluminum-doped ZnO (AZO)^[237,66] or Gallium doped ZnO (GZO)^[238,239,64,67] deposited by sputtering.

A typical STCdTe solar cell uses a CdS buffer layer to form the p-n junction, while the transparent electrode layers can be formed out of FTO, AZO, or ITO as the top and the bottom

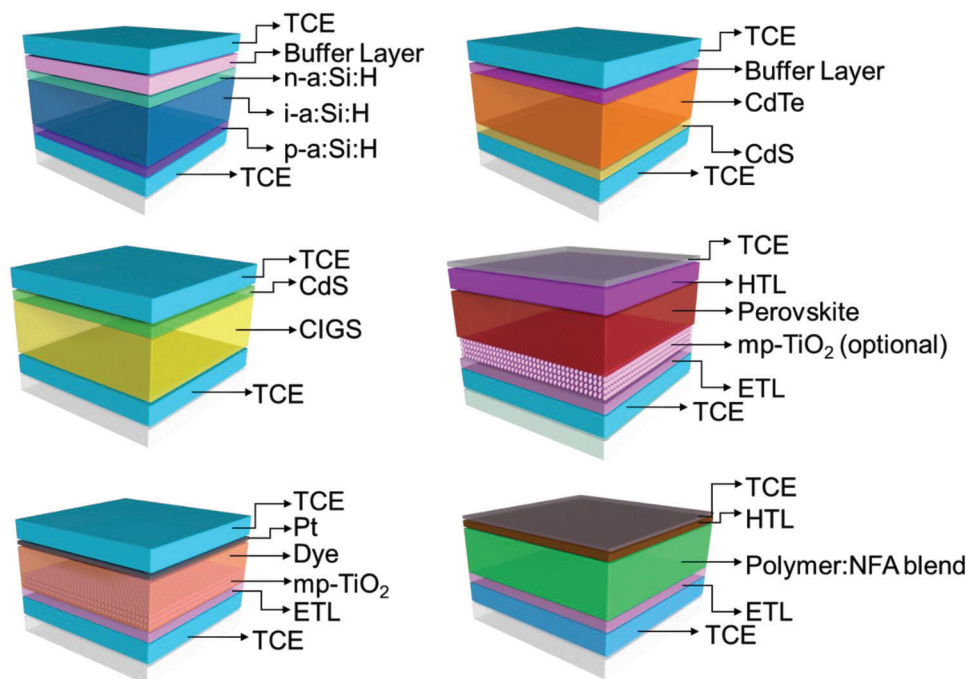


Figure 15. Typical device architectures of semitransparent solar cell technologies. TCE, transparent conductive oxide; HTL, hole transport layer; ETL, electron transport layer; NFA, non-fullerene acceptor; mp-TiO₂, mesoporous TiO₂.

contact layer.^[240,75,77,85] State-of-the-art CdTe solar cells utilize CdS:O^[241] or Mg_xZn_{1-x}O^[242] for electron selective buffer and ZnTe:Cu^[243] for hole selective interface layer to improve charge injection and reduce recombination loss. These improvements are yet to be applied in semitransparent devices since the literature reports are rare. In CIGS-based semitransparent solar cells, the device structure is similar to CdTe.^[232,244,73,79] An intrinsic buffer layer (i-ZnO) can be inserted between the CdS layer and the top contact.^[232] To introduce semitransparency in optimized opaque devices, the commonly used molybdenum (Mo) back contact is replaced by a TCO thin film. Both these technologies (STCdTe and STCIGS) have traditionally used CdS buffer layers which limit their commercialization since CdS is considered toxic. Major commercial production has shifted focus on Cd-free buffer layers like ZnS, In₂S₃, Zn_{1-x}Mg_xO, and Zn_xTi_{1-x}O.^[90]

STDSSCs are usually composed of a semitransparent photoanode made of a mesoporous TiO₂ layer on FTO glass and an ultrathin Pt counter electrode on the glass to provide sufficient transparency.^[137,245] The TiO₂ layer is kept at a few microns thickness with particles in the 15–20 nm range to keep the transparency high (>75% in the visible region). A thicker TiO₂ layer would contribute more to the J_{SC} due to diffuse scattering, albeit with a loss in transparency. To avoid the high temperature (500 °C) sintering step in TiO₂-based devices, alternative photoanodes have also been explored (such as ZnO,^[246,247] Nb₂O₅,^[248] SnO₂,^[249] WO₃,^[250] and so on), but the PCE of DSSCs based on these photoanodes are usually lower than that with TiO₂.^[251] The use of liquid electrolytes also presents leakage issues prompting investigations into alternative solid-state hole transport materials: 2,2',7,7'-tetrakis-(N,N-dimethoxyphenylamine)-9,9'-spirobifluorene (spiro-OMeTAD), polyfluorenes, PEDOT, CuSCN, NiO, and so on. Among these,

Spiro-OMeTAD performs the best, though it is costly and has limited stability.^[252]

In semitransparent organic solar cells, ETLs and HTLs facilitate the charge transport to the respective electrodes. The bottom contact is usually ITO coated on glass or plastic substrates, and the top contact is made of ultrathin metals, metal nanowires, conductive polymers, or TCOs.^[129,171,253–255,48]

Semitransparent perovskite solar cells have a similar structure as organic solar cells, though the physical characteristics of ETL and HTL might be slightly different.^[178,256–259] For instance, mesoporous TiO₂ (several μm thick) on a compact TiO₂ layer, often acts as electron contact in perovskite solar cells, while planar smooth ultrathin ZnO (≈30–50 nm) has been predominantly used in OPVs. Generally, conductive metal oxides (TiO₂, SnO₂, ZnO, etc.)^[260] can be used as ETLs, and Spiro-OMeTAD, PTAA, CuSCN, MoO_x, or NiO_x are the preferred HTL materials in both STOPVs and STPSCs.^[261] STOPVs and STPSCs have the potential to be roll-to-roll processed. To that end, the transport layers need to be solution-processed, preferably in the ambient atmosphere. ETLs have traditionally been solution processed in high-performance OPV and PSC devices. Solution-processed inorganic HTLs have also been reported (MoO_x,^[262,263] VO_x,^[264] WO_x,^[265,266] NiO_x,^[267] and so on), but the vacuum-thermal-evaporated MoO_x and inert-ambient-processed Spiro-OMeTAD have been the HTLs of choice in top performing OPVs and PSCs, respectively.

5.3. Light Management Engineering

There exists a trade-off between active layer thickness and transparency since none of the absorber layers are completely

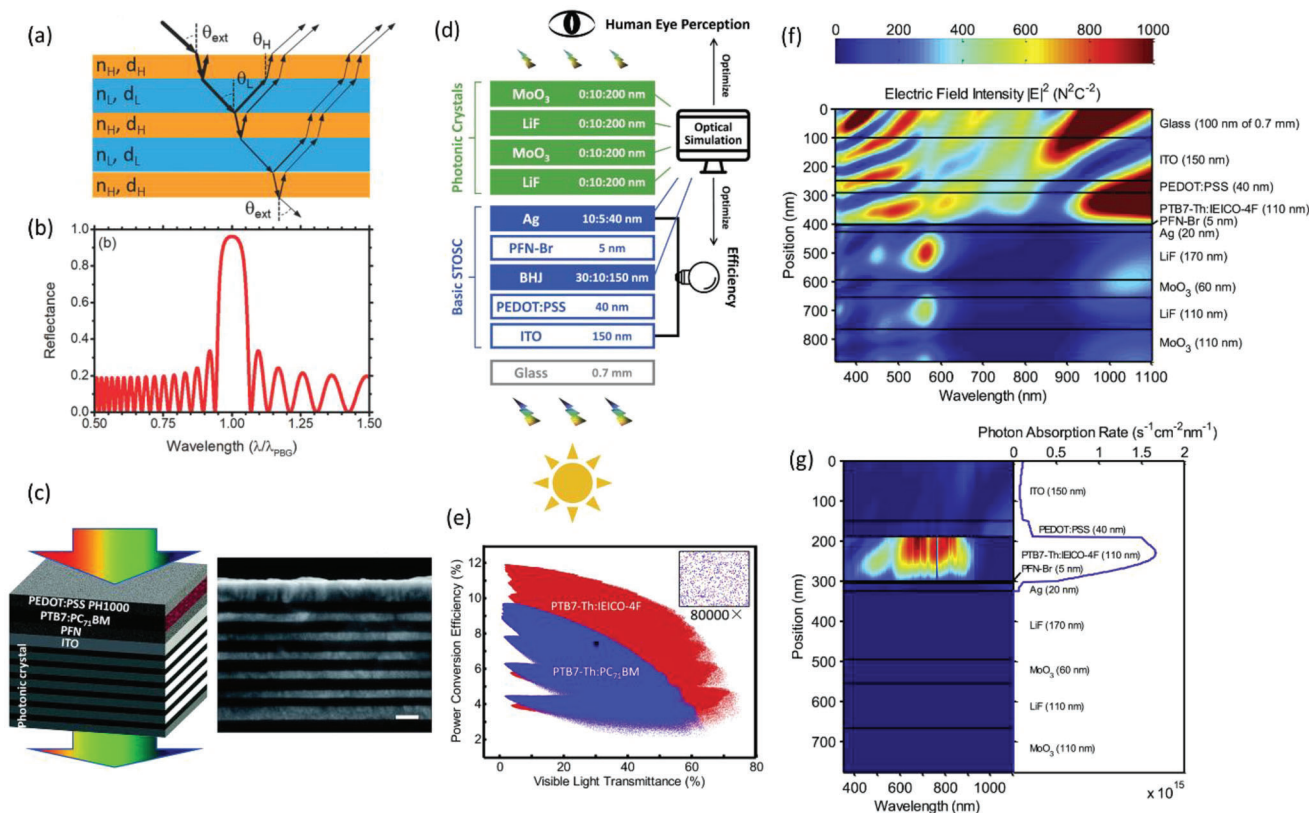


Figure 16. a) Reflection, refraction, and transmission in a distributed Bragg reflector (DBR) with refractive index $n_H > n_L$. b) Reflectance spectrum of a DBR consisting of 15 periods of transparent layers with $n_H = 1.69$ and $n_L = 1.46$. Reproduced according to the terms of the CC BY license.^[271] Copyright 2018, The Authors, published by Wiley-VCH. c) Schematic of a device structure of the STOSC utilizing 1D photonic crystal (cross-sectional SEM images of 1DPC [SEM bar = 200 nm] are shown to the right of device structure). Reproduced with permission.^[272] Copyright 2016, Royal Society of Chemistry. d) Device structure and layer thicknesses used for STOSC device optimization. e) Simulated PCE-VLT coordinates for STOSC devices in (d) for two different active layers. The insert is the magnification at the black point. f) Simulated optical electric field $\|E\|^2$ distribution and g) simulated photon absorption rate distribution and its integral over wavelength, for one device with active layer PTB7-Th:IEICO-4F. The thicknesses of each layer are given in the plot. Reproduced with permission.^[50] Copyright 2019, Elsevier Inc.

transparent in the visible region (400–700 nm). Also there exists an optimal thickness below/above which PCE starts decreasing, especially for low mobility absorbers like organics. STPV, therefore, can benefit from a wide range of optical managements techniques that tune the optical electric field inside the device due to interference effects.^[268–270] These are embedded into STPVs to minimize the efficiency loss without significantly affecting the transmission of visible light while reflecting the ultraviolet and infrared light. Often, they are used to tune the color appearance of the device.

5.3.1. 1D Photonic Crystals

Photonic crystals are optimized dielectric structures that redistribute the energy band structure of photons inside the STPV.^[271,273,274] Distributed Bragg reflectors (DBRs) are the simplest photonic crystals made of N alternate layers of two thin transparent films of thicknesses d_H and d_L , and refractive indices n_H and n_L . The incident light is partly reflected, refracted, and transmitted at each interface (Figure 16a). The thicknesses and refractive indices of these layers determine whether the reflective

and transmitted waves interfere constructively or destructively. This leads to a photonic band structure with a certain photonic bandgap (PBG) (Figure 16b). The condition that maximizes the reflectance is given as:^[271,275]

$$n_L d_L = n_H d_H = \frac{\lambda_0}{4} \quad (5)$$

where λ_0 corresponds to the reflection center wavelength. The peak reflectivity in this condition is given by

$$R_{PBG} = 1 - 4 \left(\frac{n_L}{n_H} \right)^N \quad (6)$$

The photonic band gap width ($\Delta\omega$) is given by^[271,275]

$$\frac{\Delta\omega}{\omega} = \frac{4 n_H - n_L}{\pi n_H - n_L} \quad (7)$$

One can see from the equations above that the reflection can be maximized by increasing the number of layers. The width of the reflecting wavelength range is essentially determined by the refractive index contrast (high n_H/n_L ratio).

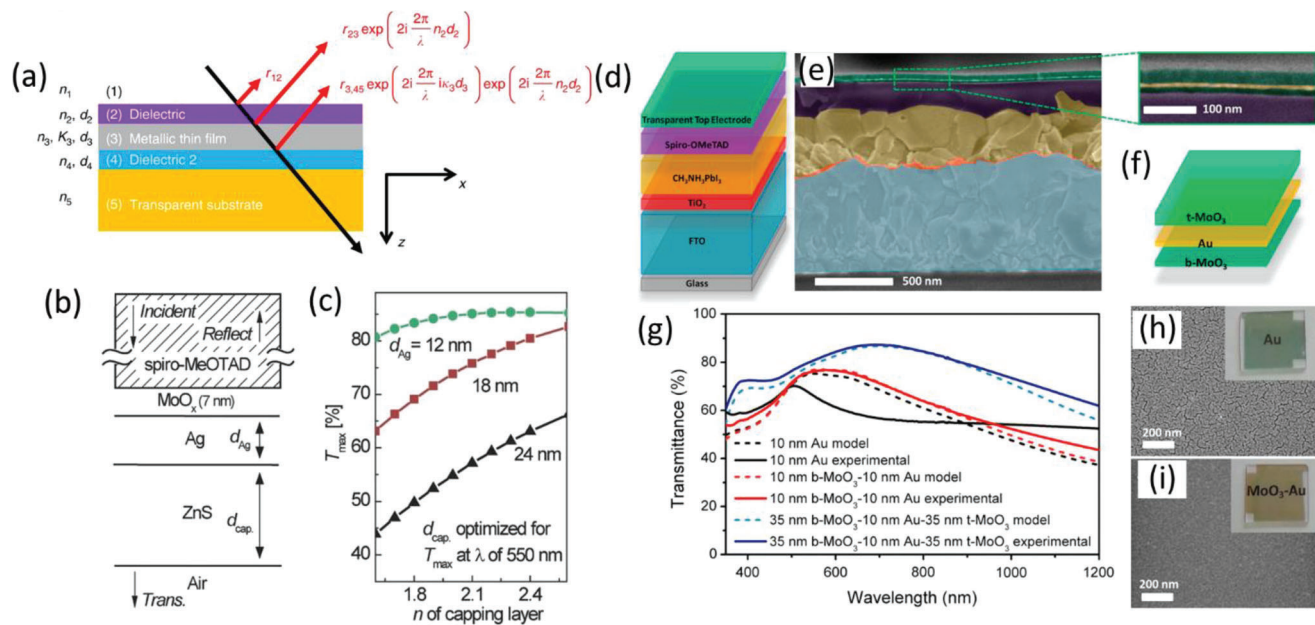


Figure 17. a) Design parameters and reflection waves at various interfaces of a dielectric-metal-dielectric (DMD) transparent electrode. Reproduced according to the terms of the CC BY license.^[276] Copyright 2020, The Author(s), published by Springer Nature. b) Schematic configuration of a dielectric-capped metal thin electrode: MoO_x (7 nm)/Ag (d_{Ag})/ZnS (d_{cap}) grown on spiro-MeOTAD. (c) A graph showing maximum transmittance (T_{max} ; at $\lambda = 550$ nm) of MoO_x (7 nm)/Ag ($d_{Ag} = 12, 18,$ or 24 nm)/capping layer (d_{cap}) as a function of the refractive index (n) of its capping layer. d_{cap} is optimized for maximal transmittance at λ of 550 nm in each case. In (b) and (c), spiro-MeOTAD, from which light is incident, is assumed to fill the half-infinite space for this calculation. Reproduced with permission.^[117] Copyright 2016, Wiley-VCH. d) Schematic illustration of the cell architecture and e) SEM image of the cross-section of a complete STPSC device utilizing DMD top electrode. f) Enlarged view of the MoO₃/Au/MoO₃ multilayer top electrode and schematic of its structure. g) Simulations (shaded dashed lines) and experimental data (solid lines) showing the transmittance of Au (black), bottom-MoO₃/Au (red), and bottom-MoO₃/Au/top-MoO₃ (blue). h) SEM image of the Au film and i) bottom-MoO₃/Au film. The insets show photos of the two samples. Reproduced with permission.^[119] Copyright 2015, Elsevier Ltd.

Zhang et al.^[272] reported a STOSC device using a polymer (PE-DOT:PSS) top electrode and 1DPC on the bottom ITO contact. Device structure of complete device and cross section SEM of 1DPC is shown in Figure 16c. They reported a PCE of 5.20% with a good AVT of 23.24%. In comparison, STOSC device without 1DPC obtained lower PCE (4.27%) but higher AVT (39%). The opaque reference device (with Al electrode instead of ITO) showed a PCE of 6.52%.

A similar approach is employed in aperiodic dielectric reflectors (also called ABPF),^[62] which consist of multiple ultrathin-dielectric layers of different indexes of refraction with different thicknesses in alternating layers. Similarly, Yip et al.^[50] used the transfer matrix method (TMM) to numerically analyze the light propagation in thin film stacks. A high-throughput optical model was used to investigate the optical properties of 1DPC-enhanced STOSCs by simulating millions of device configurations with varying thicknesses of active layer, ultrathin Ag electrode and thickness of 1D photonic crystals (device structure and simulation output are shown in Figure 16d,e). Briefly, TMM model calculates the optical electric field $|E|^2$ distribution at each position of the multilayered structure and the corresponding photon absorption rate (G) is calculated using^[50]

$$G = \frac{2\pi\epsilon_0 nk I_{1.5G}}{h} |E|^2 \quad (8)$$

where ϵ_0 and h represent permittivity of free space and plank constant, n and k are optical constants of the active layer, and $I_{1.5G}$ represents the spectral light intensity distribution of AM1.5G. Figure 16f shows the simulated $|E|^2$ distribution of one such device and Figure 16g shows corresponding simulated photon absorption rate and its integral over wavelength. Guided by the results of the simulation, they fabricated a STOSC (active layer: PTB7-Th:IEICO-4F) with a high PCE (10.8%) and AVT (29.5%), which agreed well with the model predictions.

5.3.2. DMD Electrode Structure

A dielectric-metal-dielectric (DMD)-based transparent electrode consists of a thin metallic film sandwiched between two antireflection dielectrics to obtain high transparency, while maintaining reasonable conductivity (sheet resistance (R_s) $< 20 \Omega \text{ sq}^{-1}$). Interference of the reflected lights at each of the interfaces can be tuned to reduce the reflection from the metal thin film in the visible range.^[276,277] As shown in Figure 17a, a DMD electrode needs optimization of seven parameters (refractive indices and thicknesses of the two dielectric layers and the metallic layer). In a typical optimization process: (1) a suitable electrode material with highest conductivity and low loss (n_k) in the visible range is selected. The thickness (lowest possible) is selected to achieve a certain

minimum electrical conductivity. (2) highest possible refractive index material is selected for Dielectric 2. The thickness of Dielectric 2 is found using the Equation (3); the refractive index of Dielectric 1 is optimized for optimum transmittance. The typical range of refractive index falls between 1.38 and 2.6.^[276] In most of the cases, the material and thickness of one of the dielectrics in the DMD electrode is fixed since they act as electron/hole transport layer. Therefore, the optimization of metal thickness and outer dielectric can be done relatively easily.^[278] Kim et al. have optimized the thickness of Ag (d_{Ag}), thickness of the capping layer dielectric ZnS (d_{ZnS}), and dielectric constant n of the capping layer in a DMD like top electrode for STPSC application with spiro-OMeTAD as HTL (Figure 17b). The thickness of the first interfacial dielectric, MoO_x , was kept at 7 nm (as thin as possible to maximize NIR reflection as per the design criteria). From the optimization curve for various thicknesses of Ag (12, 18, and 24 nm), it was confirmed that the capping layer should have as high refractive index (n) as possible to maximize the transmittance (Figure 17c). Notably, for dielectric capping layer with high n of 2.4, T_{max} of 65% can be achieved even with 24 nm thick Ag layers.

Della Gaspera et al.^[119] reported an STPSC using a DMD transparent electrode (MoO_3 -Au- MoO_3) to obtain a record PCE of 5.5% at an AVT of 31% in STPSC (Figure 17d–f). They observed a low transmittance for a neat 10 nm thick Au film due to its high reflectance. On the other hand, when the thin Au film is sandwiched between the two MoO_3 dielectric layers, a destructive interference in the visible range can be achieved via a simple tuning of the MoO_3 layer thicknesses to provide an increase in transparency (Figure 17g). Moreover, a more continuous Au film was obtained on MoO_3 compared to the Au film grown on glass substrate or spiro-OMeTAD (Figure 17 h,i). Çetinkaya et al.^[278] optimized the thickness of the $MoO_3/Ag/MoO_3$ layer (dielectric/metal/dielectric or DMD) using the TMM to maximize the AVT of the STOPV device. The optimized device structure maintained 88% of the opaque device PCE while also obtaining an AVT of 37%. However, the optimization of the thickness of each layer becomes increasingly complex with increasing number of layers.^[279]

It should be noted that the thickness of dielectrics in the DMD structure is normally in the range of tens of nanometers. This raises a concern about the processing methods and the list of materials that can be uniformly coated with precise thickness control. Therefore, in addition to thermal evaporation which has been predominantly used for dielectric deposition (MoO_3 , WO_3 , etc.), ALD would be better suited for better uniformity. He et al.^[280] used ALD ZnO in a DMD electrode ($ZnO(10\text{ nm})/Ag(10\text{ nm})/ZnO(35\text{ nm})$) with ultra-low sheet resistance ($2.6\ \Omega\ sq^{-1}$) in STPSC and obtained 10% PCE with 19.6% AVT.

5.3.3. Optical Resonance Cavity Effect

Enhancing the performance of thin film solar cells using light-trapping approach has been quite attractive. In the devices with two reflecting electrodes (or even DMs), the incoming light can be made to interfere constructively to obtain a resonance condition within the active layer region.^[281,282] In a microcavity struc-

ture, the incident light makes round trip between two cavity mirrors (Figure 18a,b) and the optical resonance condition can be described by the equation^[281]

$$\frac{4\pi \sum n_i d_i}{\lambda} + \Psi_1 + \Psi_2 = 2m\pi \quad (9)$$

where n_i and d_i represent the refractive index and thicknesses of the absorber layer and transport layers (all the layers between the two electrodes), respectively; and Ψ_1 and Ψ_2 are the reflection phase shift of input mirror and output mirror; λ is the wavelength of the incident light; m is the mode number. Effectively, the left term of equation X represents the round-trip phase shift of the microcavity. The resonance effect induced by microcavity structure is stronger in solar cells with absorber layer thickness less than or comparable to the incident wavelength. Therefore, this design is expected to be quite effective in semitransparent solar cells with reduced thickness of the absorber layer.^[281,283] It should be highlighted that a multilayered structure of STPV with electron/hole buffer/transport layers will affect the condition of resonance inside the device and should be taken into account during optical modeling.^[282] These layers can in fact act as optical spacers and can be managed to tune the spectral and spatial distribution of electric field inside the device.^[282]

Zhong et al.^[281] reported a semitransparent microcavity in a device structure where the active layer is sandwiched between $WO_3/Ag/WO_3$ multilayer electrode and thin Ag electrode capped by 1DPC. This structure demonstrates an efficient light trapping capability. The improvement in optical absorption can be visualized in Figure 18c (with microcavity) and Figure 18d (without microcavity). The optical electrical field in the wavelength range 610–780 is significantly enhanced in device with microcavity. With the inclusion of microcavity design, PCE was improved by 14% and AVT was improved by 8%. Han et al.^[284] used a microcavity electrode ($Ag/MgF_2/Ag$) as a spectral selective transmissive electrode to tune the color in STOSC devices (Figure 18e,f). By adjusting MgF_2 dielectric thickness, colorful OSCs were realized while maintaining decent PCEs relative to opaque device ($Ag = 100\text{ nm}$) and PCEs similar to device without microcavity ($Ag = 35\text{ nm}$) (Figure 18g). Blue, green, and red STOSC devices are shown in Figure 18h.

5.3.4. Outcoupling Layer

An OC layer can be applied at the exit surface to tune the appearance and transparency of STPV without altering the electrical characteristics of the devices.^[254,279,285,48] It simulates a combined effect of light trapping inside the active layer and reflection at desired respective wavelengths. They consist of a capping layer of single dielectric layer^[285–287] or alternative dielectric bi-layers with different refractive indices and thicknesses.^[288,48] A transfer matrix model is used similar to that used in 1DPC-based STPVs (Figure 16f) or microcavity resonance effects (Figure 18c,d), to optimize the layer thicknesses for a particular low/high dielectric material combination.

Li et al.^[279] simulated the relative improvements with the addition of OC layers in combination with BDR and anti-reflection coating (Figure 19a) for a STOPV device with maximum

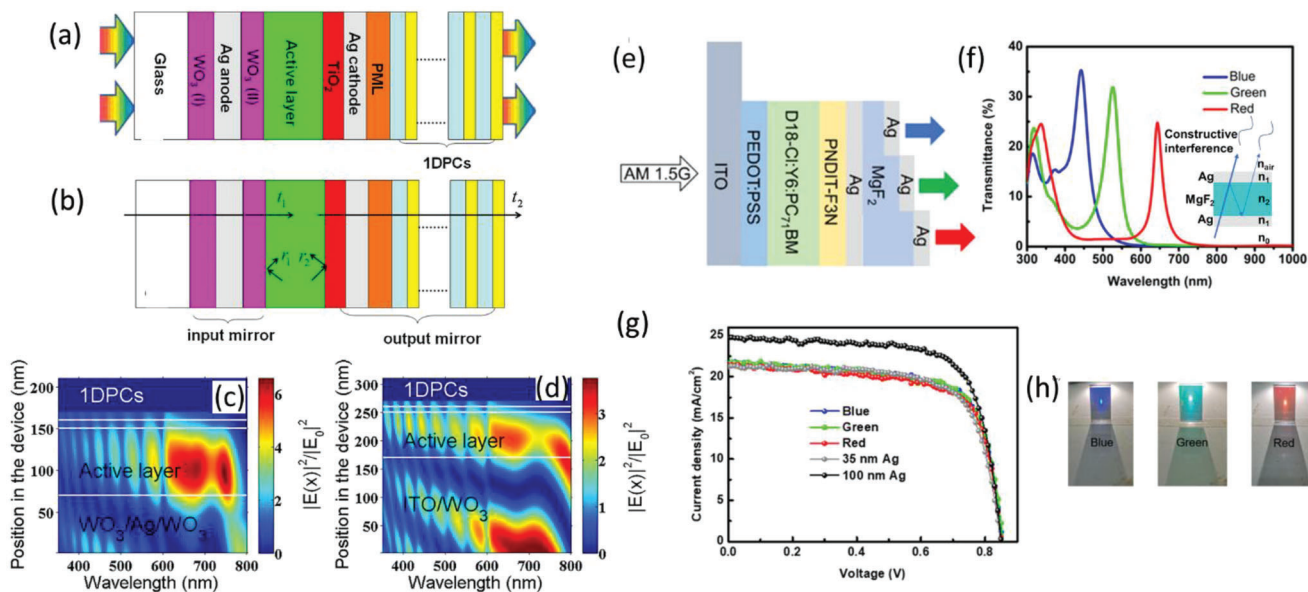


Figure 18. a) Structure of 1DPC-based STOSCs with a microcavity structure; b) structure of the microcavity within the device (a). t_1 and t_2 , respectively, denote the transmission coefficient of input and output mirrors; r_1 and r_2 , respectively, denote the reflection coefficient of input and output mirrors. Optical electric field in device with (c) and in device without (d) optical microcavity. In device without microcavity, the $\text{WO}_3(\text{I})/\text{Ag}$ anode in STOSC device structure shown in (a) is replaced by ITO. $|E|^2$ is optical electric field intensity within devices and $|E_0|^2$ denotes the optical electric field intensity of incident light. Reproduced with permission.^[281] Copyright 2018, Elsevier. (e) Device structure of colorful semitransparent OSCs using $\text{Ag}/\text{MgF}_2/\text{Ag}$ microcavity. (f) Transmittance spectra of semitransparent and colorful OSCs based on the device structure in (e). Inset shows the schematic diagram of the microcavity (n : refractive index) (g) J-V characteristics of opaque and colorful OSCs shown in (e). (h) Seeing-through photographs of the colorful OSCs achieved by varying MgF_2 thickness. Reproduced with permission.^[284] Copyright 2022, Wiley VCH.

PCE = 10% in the opaque device. The LUE space plot highlights the importance of BDR, OC, and ARCs toward achieving high PCE and high AVT (APT) simultaneously. Li et al.^[254] used a combination of optical OC and ARC to improve visible light transmittance and enhance reflection in the NIR to improve the LUE (Figure 19b–d). A high LUE of $3.56 \pm 0.11\%$ was reported for STOSC device with OC and anti-reflection layer compared to the control device with LUE of $2.07 \pm 0.06\%$. Huang et al.^[288] utilized a four-layer OC structure comprising ZnS (30 nm)/ MgF_2 (100 nm)/4,4'-bis(N-carbazolyl)-1,1'-biphenyl (CBP) (90 nm)/ MgF_2 (10 nm) at the top electrode improving AVT. The OC structure significantly increases AVT from $20.0 \pm 1.0\%$ to $38.1 \pm 1.1\%$, while maintaining a PCE = $7.3 \pm 0.1\%$.

5.3.5. Antireflection Coating

ARCs are coated on the external surface of the semitransparent substrates to reduce the reflection losses. It can be applied in a relatively simple fabrication process as a single-layer or multi-layer ARC coating. To reduce reflection at a particular wavelength λ_0 , the thickness and refractive index of the ARC layer are determined by^[289]

$$n_{\text{ARC}} = \sqrt{n_{\text{sub}} \cdot n_{\text{in}}} \quad (10)$$

$$d_{\text{ARC}} = \frac{\lambda_0}{4 \times n_{\text{ARC}}} \quad (11)$$

where n_{sub} is the refractive index of the substrate (glass in most of the cases) and n_{in} is the refractive index of adjacent incidence medium (air). In most cases, a single ARC layer is not sufficient to reduce reflection in wide wavelength range. A double layer ARC is applied to reduce the reflection further and the optimum refractive indices of the materials are obtained by^[290,291]

$$n_1 = \sqrt[3]{n_{\text{in}}^2 \cdot n_{\text{sub}}} \quad (12)$$

and

$$n_2 = \sqrt[3]{n_{\text{in}} \cdot n_{\text{sub}}^2} \quad (13)$$

where n_1 and n_2 correspond to the two ARC materials forming the ARC, from top to bottom. For more than two-layered ARC, the values of refractive indices can be found using suitable equations.^[289–291]

Liu et al.^[62] obtained up to 60% enhancement in AVT using a combination of a) an ABPF (consisting of aperiodic $[\text{LiF}/\text{TeO}_2]^8/\text{LiF}$) and b) an antireflection coating (ARC) glass substrate (LiF/TeO_2)⁴. Pastorelli et al.^[292] used a multilayer dielectric structure and anti-reflective coating in a semitransparent device (AVT = 21.4%) and obtained 90% of the PCE of the corresponding opaque solar cell (5.3% vs 5.9%, respectively).

Most of the light management techniques have mostly been employed in high LUE STOPVs and STPSCs but are expected to be a common feature in other STPV technologies as well. It is important to highlight the importance of optical simulations to

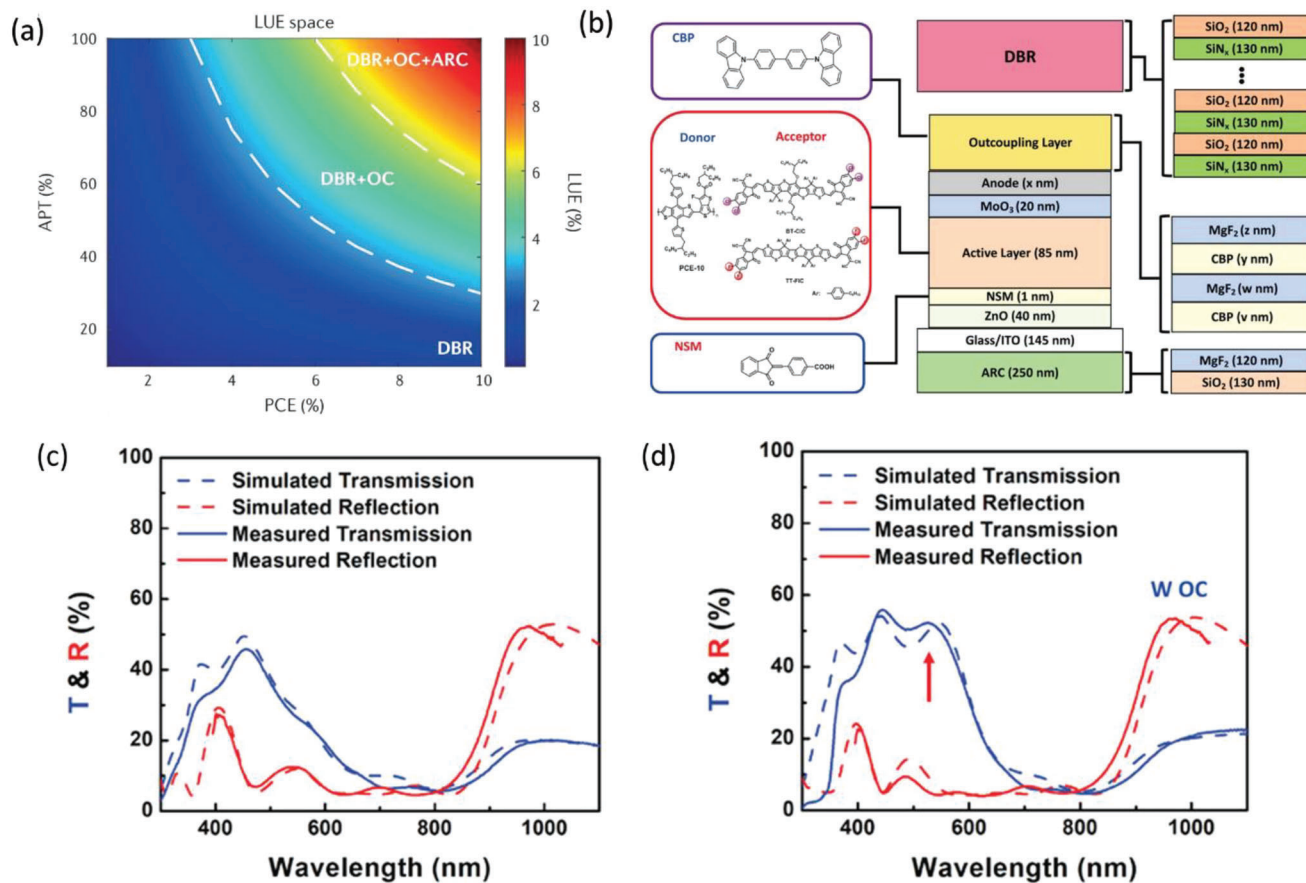


Figure 19. a) LUE space for a STOPV device showing the trade-off between the PCE and the APT (same as AVT), a PCE of 10% at APT = 0%. Adding DBR yields a high PCE but does not enhance the APT. An optical outcoupling layer alone improves only the APT. The use of both a DBR and an optical outcoupling layer yields both a high PCE and a high APT, and thus a high LUE. The use of an ARC, a DBR, and an optical outcoupling structure leads to the best LUE value. Dashed lines represent constant LUE. Reproduced with permission.^[279] Copyright 2022, Springer Nature Limited. b) Schematic of an optically efficient STOPV device showing detailed layer structures of outcoupling layer, ARC, and DBR. Simulated and measured transmittance and reflectance without (c) and with (d) outcoupling coatings. Reproduced with permission.^[254] Copyright 2019, Wiley-VCH.

optimize the optical and electrical characteristics of a STPV.^[41] TMM model^[293] and finite-difference time domain^[171,294] methods are two of the most common methods to simulate the transmission/reflection spectrum of the complete device including the additional layers for light management discussed above. These methods use simple input parameters: thicknesses (d_j where $j = 1, 2, \dots, m$) and complex refractive indices, $n_j + ik_j$ (n and k are the refractive index and absorption coefficient of the material) of each layer and should prove to be a useful tool for all STPV research.^[41]

6. Scale-up, Stability, and Cost Analysis

Some commercial solar window products do exist in the market. Transparent see-through cadmium telluride (CdTe) solar panels from Polysolar, semitransparent OPVs from Solar Window Inc., and amorphous Si semitransparent products from Onyx Solar, to name a few.^{13,17,9} Given the nascent level of progress of STPVs, there are scaling and stability challenges that are generally overlooked in the literature reports of high LUE STPV devices.

6.1. Large Scale Scaling

In order to achieve practical voltages and currents from STPV devices, they need to be connected in series or parallel configuration. The interconnection types can be loosely categorized into: a) wafer-level interconnection (like that in silicon solar cells) (Figure 20a); b) monolithic interconnection (P1P2P3 type shown in Figure 20b); c) DSSC module designs with the two electrodes joined together by a sealant in Z or W configuration (Figure 20c). In modules, a significant area is consumed by the cell interconnections (termed as dead area). This reduces the geometric fill factor (GFF), which is defined as the ratio of active area to the total area of module.

Traditional thin film solar cell (CdTe, CIGS, a-Si:H) solar modules are typically fabricated in a monolithic design on a substrate with slight variations.^[297] In monolithic integration (Figure 20b), a total of three scribes are done to isolate and interconnect the solar cells in series. The first scribe P1 is done on the first transparent conductive electrode (TCE1). Then, the subsequent layers including absorber and transport/buffer layers are deposited. A second scribe P2 is done on the deposited layers till the TCE.

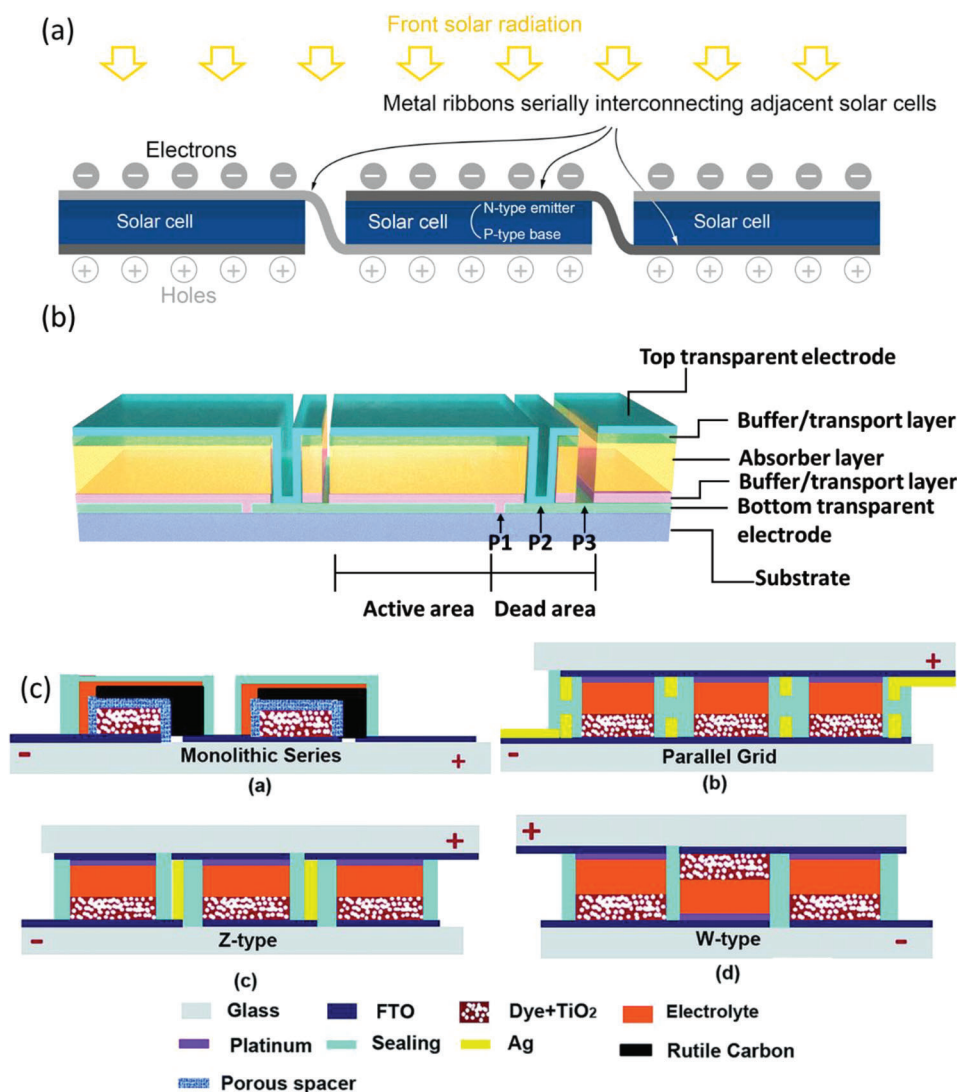


Figure 20. Module integration types: a) Wafer-level interconnection of conventional planar silicon solar modules. Reproduced with permission.^[295] Copyright 2020, Elsevier B.V. b) P1P2P3 monolithic integration, and c) DSSC module integration: monolithic, parallel, Z-type, and W-type. Reproduced with permission.^[296] Copyright 2014, Royal Society of Chemistry.

Subsequently, the second TCE is deposited such that it connects to the bottom contact of the next cell. Finally, the third scribe P3 is done to separate the second TCE into separate stripes leading to series connected cells. A DSSC module is fabricated in a slightly different design due to unique physical characteristics of the constituent layers. For example, the top TCE needs to have catalytic properties in addition to transparency. Also, the liquid electrolyte should be injected into the cell and should be separated via a sealant (Figure 20c).

Loss in PCE is inevitable as the area of the solar cell is increased.^[298] Even in conventional crystalline silicon photovoltaics, there exists a cell-to-module efficiency gap of 10–15%.^[299] In STPVs, this scaling loss adds up due to the series resistance (R_s) of the transparent electrode, which increases almost linearly with the area. For perspective, Galagan et al.^[300] calculated the optimum width of the sub-cells in the perovskite module (with 100 nm opaque Au top electrode) to be in the range

of 0.3–0.4 cm if the sheet resistance of the TCO (the bottom electrode) is around $40 \Omega \text{ sq}^{-1}$. This limitation will be more severe in the case of semitransparent solar cells where both the electrodes are essentially semitransparent and less conductive (than 100 nm metal electrode)—an additional loss because of more resistive transparent top contact. Scaling issues are more critical to third-generation PV technologies since they are mostly unproven technologies. Most of the reported high LUE devices have areas of less than 1 cm^2 .

Large area modules have indeed been reported, though mostly in opaque OPV form. An opaque OPV module with an area of 204 cm^2 and an efficiency of 11.7% was reported by Distler et al. using blade coating.^[301] Deng et al.^[302] reported a large area, blade-coated perovskite module with an efficiency of 16.9% with an aperture area of 63.7 cm^2 . Notably, the small area device (0.08 cm^2) had an efficiency of 21.3%, thus, a scaling gap of $\approx 21\%$. High-performance minimodules (19.3 cm^2) for both

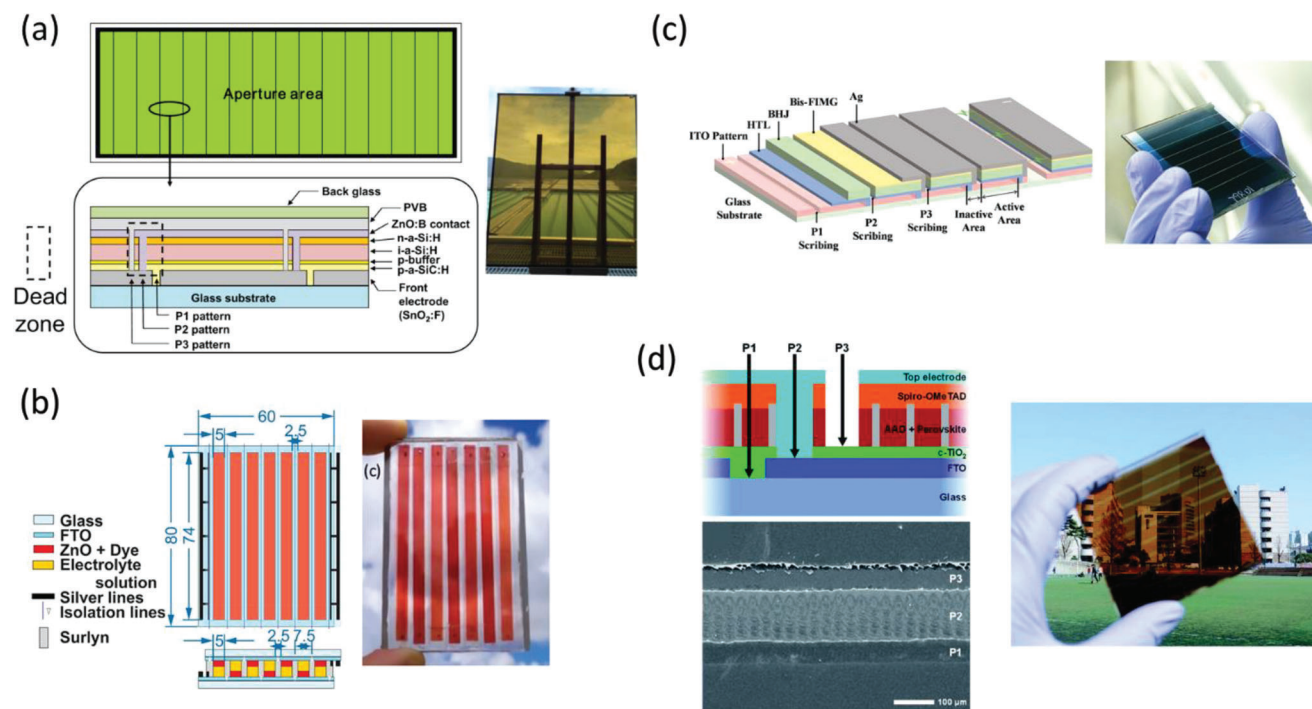


Figure 21. a) Structure of the fabricated a-Si:H semi-transparent PV modules. A photograph image of the fabricated a-Si:H semi-transparent module (1.43 m^2) is shown on the right. Reproduced with permission.^[307] Copyright 2015, Elsevier B.V. b) Design and configuration of the minimodules with 7-strips series connected DSSC. The numbers in blue are dimensions in millimeters. The photograph on the right shows the assembled minimodule. Reproduced with permission.^[308] Copyright 2022, The Authors, American Chemical Society. c) Structure of an organic solar module (19.73 cm^2). Photograph of the fabricated organic solar module is shown on the right. Reproduced with permission.^[303] Copyright 2022, Wiley-VCH. d) Schematic of anodized aluminum oxide (AAO) template-based perovskite solar module. (Bottom) The surface SEM image of the three etching steps (P1, P2, and P3) for monolithic integration of the module is shown. Photograph of the semitransparent solar module (40.8 cm^2). Reproduced with permission.^[15] Copyright 2020, Royal Society of Chemistry.

perovskite (average PCE = 21.4%) and OPV (average PCE = 14.5%) have been reported by Microquanta and their collaborators.^[299,303] Other promising large-area OPV modules have been reported elsewhere: 14.7% at 5.4 cm^2 ,^[304] 14.3% at 36 cm^2 area,^[305] 12.6% on 26 cm^2 , and 13.25% for 19.34 cm^2 area.^[306]

Some examples of STPV modules with their module designs are shown in Figure 21a–d.^[303,307,308,53] Apart from these, several other example STPV modules have been reported. STOPV module with over 30 cm^2 area was reported with PCE of 7.2% and AVT of 22.3%.^[309] It is notable that the small area device (0.04 cm^2) achieved a PCE of 12.5%. This translates to a scaling gap of 42% from cell to module for semitransparent devices. The semitransparent OPV mini-module (19.3 cm^2) reported by Wang et al.^[310] had a PCE of 11.28% with excellent features for power window applications—IRR of 0.90, AVT of 32.07%, and CRI of 90. Vesce et al.^[311] have recently reported a large area STDSSC module (400 cm^2) with an impressive AVT of 35.7% and a PCE of 5.1%, using a scalable screen printing technique.

In summary, the conventional thin film STPVs (a-Si, CdTe, CIGS, and derivatives) enjoy existing proven scaling technologies while the emerging third-generation STPV technologies are still under development, and thus the cell-to-module gap is usually high for modules larger than 100 cm^2 .^[300,312] For comparison, the commercial thin-film modules (CdTe, CIGS, a-Si:H) are usually more than 1 m^2 in area. Therefore, these

emerging STPV modules (STOPVs, STPSCs, and STDSSCs) need more attention toward optimization and standardization of module fabrication technologies to minimize the large area scaling gap.

6.2. Stability

Long-term stability is the key to commercialization. Commercial PV for outdoor use requires a long-term life of more than 25 years.^[313] IEC61215 states the minimum requirement that solar cell technologies must guarantee to be used commercially.^[314,315] This standard includes a damp heat test of 1000 h at $85 \text{ }^\circ\text{C}$ at 85% RH, along with other tests such as outdoor exposure test, hot spot endurance test, thermal cycling test, mechanical tests, and so on.^[315] However, most of the lab-level stability tests focus on one or two (or a subset) of these recommended tests and therefore overestimate the real-life reliability. Additionally, most of the stability tests in the literature were done on opaque solar cells, and extrapolating the same to the semitransparent counterpart (with different contacts and associated interfaces) would be misleading.^[107]

Semitransparent CdTe^[58] and a-Si^[316] solar cells have proven stability and have been commercialized to some extent. Stability issues for the opaque a-Si solar cells, like light-induced degradation (LID) by the Staebler–Wronski effect, have long been a

challenge for a-Si solar cells but have been solved to a large extent.^[317–319]

DSSC solar cells in outdoor testing could last just 4 years in one study.^[320] Several degradation mechanisms are responsible: dye desorption, decrease in ion concentration of electrolyte, degradation at electrodes, effect of ultraviolet light and moisture, sealing issues, and so on.^[135,139] Different approaches targeting specific degradation mechanisms have been tried with promising success: using solid-state hole transport material replacing liquid I^-/I_3^- electrolyte,^[321,322] alternative counter electrodes,^[135,323–325] and so on.^[134,139,326]

Although semitransparent organic and perovskite solar cells have the highest LUEs among all the semitransparent solar cells, they use active layers that are inherently unstable in light and under other environmental stresses. The issue of stability is further complicated as most high LUE devices utilize organic materials as buffer/interface layers (spiro-OMeTAD,^[327] PCBM,^[258] PEDOT:PSS,^[328] etc.). For perovskites, there is: a) intrinsic instability of absorber layers (defects in bulk, morphology, phase change, ion migration, etc.),^[329–332] b) instability of the hole transport layers: organic layers with low thermal stability and low crystallinity of inorganic materials, c) photo-instability of ETL layers (particularly TiO_2), d) diffusion and corrosion of electrodes, and e) presence of chemically active and delamination prone interfaces.^[314,333] Most of these degradation pathways are also seen in OPVs. Inorganic perovskite solar cells have been explored for better stability, though the PCE is slightly lower than the organic-inorganic hybrid perovskites.^[148,157–160] Additionally, to improve stability, solar cells based on all inorganic layers (including the hole transport layer) have also attracted attention. Nevertheless, the most efficient perovskite solar cells are based on unstable organic HTMs (like Spiro-OMeTAD).^[336] Several encapsulation techniques have been used such as barrier foil encapsulation (metal foil, ultrathin glass, polymers etc.)^[337] or thin-film encapsulation (via CVD, ALD, sputtering, plasma-enhanced molecular layer deposition (PEMLD), etc.),^[338–340] but they are still in the research phase and need further optimization and proof-of-concept on large modules.

The key material, the active layer in OPVs, is organic and susceptible to water and oxygen, causing photo-oxidation in bulk and at interfaces.^[341–343] At the same time, not all OPV devices have the same rates of degradation. Burlingame et al.^[344] reported a promising stable organic solar cell with DBP:C70 active layer and TPBi:C70 cathode buffer layer (average PCE of 6.5%) when subjected to high temperatures and very high illumination intensities. It showed a long extrapolated operational lifetime of over 10000 h. The solar cells used vacuum-evaporated small molecules as active layers, which are usually more stable and have higher purity than polymer-based active layers but have slightly lower efficiencies currently (15.34% for all small molecule^[345] vs 19.3% for polymer: non-fullerene acceptor [NFA] blend).^[7] A significant achievement for polymer:NFA blend as the active layer was reported by Xu et al.,^[346] who used self-assembled fullerene monolayer (C60-SAM) modification of ETL for OSC based on PTB7-Th:IEICO-4F blend to achieve both high efficiency and stability. They reported an extrapolated operational lifetime of 34 000 h, or 22 years, using the T_{80} standard. It is important to note that the devices (in both reports) were encapsulated and maintained

at room temperature (no thermal stress) during the photoaging test.

Most of the stability reports for perovskites and organic solar cells were performed on opaque small-area lab-based solar cells. The semitransparent counterparts have modified or different top electrodes, and hence the degradation mechanisms would be quite different and need additional detailed investigations. Moreover, series resistance and uniformity issues start dominating large-area devices, increasing the chances of device failure. Notably, degradation mechanisms in third-generation solar cell technologies (such as organic and perovskite solar cells) are still under investigation, given the infancy of these PV technologies.

6.3. Cost

To assess the feasibility of commercialization of a PV technology, efficiency (or LUE in the case of STPV), stability, and cost need to be considered simultaneously. For established PV technologies, the total module cost calculation is relatively straightforward and is done using a minimum sustainable price (MSP) model.^[347] Silicon PV with module PCE above 21–23% and lifetime more than 25 years costs less than $\$0.245\text{ W}^{-1}$ (module PCE of 20.5%, 15% gross margin). The module cost for CdTe is similar to that of c-Si ($\$0.28\text{ W}^{-1}$, for module PCE of 18%, 15% gross margin) while CIGS cost almost twice due to higher processing cost ($\$0.48\text{ W}^{-1}$, for module PCE of 16%, 15% gross margin).^[348] On the other hand, for third-generation PV technologies with roll-to-roll solution processing potential, the cost is projected to be lower than the traditional thin film technologies, particularly due to low CapEx for manufacturing equipment and facilities.^[349–351] Nevertheless, due to differing assumptions in the absence of standardization (or widespread pilot scale implementation), the projected module cost will vary significantly (e.g., $\$0.20$ to 1.2 W^{-1} for OPV module with PCEs ranging 5–10%).^[10]

When transitioning from opaque to semitransparent modules, the cost of TCE would be one of the most consequential parameters toward the overall module cost. For example, using the most common electrode ITO increases the cost of OPV module up to 30 times compared to a PEDOT+ silver grid electrode.^[352] Additionally, light management layers would be added to improve the AVT of the STPV devices, thus increasing processing steps and overall cost. For a 10% STOPV module on PET/ITO substrate with GFF = 70%, Lee et al. calculated the cost at $\$0.68\text{ W}^{-1}$ ($\$1.6\text{ W}^{-1}$ with the microinverter) with the realistic possibility of further reduction to $\$0.47\text{ W}^{-1}$ with simplified active material synthesis, PCE of 15% and GFF = 90%, and lower inverter cost.^[10]

A better index to compare the market competitiveness of different STPV technologies is the levelized cost of energy (LCOE). It is defined as the average net present cost of energy generation for a PV technology over its lifetime (LCOE = sum of costs over lifetime/sum of electrical energy over lifetime).^[353] In other words, a STPV technology should not only be evaluated on the basis of LUE but also on the cost related to manufacturing, installation, and stability of performance over time. Since LCOE is nearly inversely proportional to lifetime, it becomes an important metric for a fair comparison of STOPVs and STPSCs with the competing STPVs. Additionally, a high-performing STOPV might use complicated processes, expensive active layers, charge

transport/buffer layers, and electrodes, thus increasing the LCOE of the system.^[350,353,354] Moreover, in contrast to established thin film technologies, the determination LCOE is quite challenging for emerging STPV technologies due to the lack of performance or lifetime studies on standard size modules (module area > 1 m²).^[355] Nevertheless, with reasonable assumptions, several reports have estimated the LCOE of STOPVs and STPSCs to be in the same range or lower than that of traditional silicon PVs (LCOE of c-Si or CdTe PV technology = \$0.04–0.06 kWh⁻¹).^[355–361] For example, Song et al.^[347] estimated an LCOE of \$0.049–0.079 kWh⁻¹ with a perovskite module system with lifetime of 30 years at PCE of 16%.

7. Conclusions and Outlook

High LUEs of the state-of-the-art third-generation STPV devices (especially those based on perovskites, OSCs) at the laboratory scale show immense potential for widespread adoption in BIPV applications. They are potentially cheaper to manufacture at a large scale and can be processed at low temperatures. However, the issue of stability of these solar cells is still unresolved compared to the mature traditional thin film solar cells (a-Si, CIGS, CdTe). Nonetheless, one can still see their potential in niche markets, such as indoor and portable devices, where the degrading factors are minimal.

Thin film STPVs: The toxicity of Cd in CdTe-based STPVs is concerning and would need exceptional encapsulation and recycling plans for large-scale deployment. To a large extent, the use of the CdS buffer layer can be eliminated without loss in currents, as demonstrated consistently by Solar Frontier.^[368] Although the scarcity of Te might pose some scaling challenges, it should not be a serious concern until they reach installations up to 2 TWp.^[297] Similarly, indium in STCIGS photovoltaics causes major material availability concerns. For ST-a-Si:H devices, it would take some breakthrough improvements in PCEs or the identification of a unique application to compete with the alternatives.

STOPVs: STOPVs offers a unique advantage over other STPV technologies—tunable wavelength-selective absorption (or color neutrality). Combined with immense flexibility in color engineering, they have the highest LUE.^[369,370] Stability challenges arise from morphology and intrinsic instability. There are some exceptionally stable solar cell devices with extrapolated lifetimes of

10–20 years but almost none with real-life data. At the same time, there exists a large discrepancy in testing protocols for OPV stability, thus resulting in poorly defined lifetimes.^[312,371] Moreover, the scaling gap between cells to modules is more than 30% in OPVs,^[312] which remains the main hurdle for commercialization.

STPSCs: There are several attractive attributes of perovskites that make them as attractive as STPV technology: low-cost raw materials and processing, compatibility with flexible substrates, bandgap tunability, and so on. The record PCE of opaque PSC is at par with the already commercialized technologies, but they suffer from similar instability issues as the OPVs. Also, the module efficiencies have not reached close to the level of commercialization. Like OPVs, there exists a scaling gap of over 30% from lab to the medium-sized module. Furthermore, since majority of the STPSC devices reported till date were based on lead-based perovskites, exploration of non-toxic lead-free STPSCs would be quite significant.

STDSSCs: While DSSCs were expected to be the cheapest solar cell technology with wavelength-selective organic dyes, the low efficiency and intrinsic instability issues have prevented them from the widespread real-life application.

Device Engineering: Evaluating based on sheet resistance and transparency, several electrodes qualify as good candidates for TCEs. It is the device processing conditions, together with chemical compatibility and energy level matching with the adjacent layers, that will determine if a TCE is compatible with the device. The merits and drawbacks of a TCE, therefore, depend on the device architecture of the STPV device. Buffer or carrier transport layers perform integral role of enhancing the charge collection efficiency. Simultaneous researches in different technologies have resulted in several candidates for both n-type and p-type buffer/transport layers. For STPV applications, transmittance and compatibility with the transparent electrodes become the main selection criteria. Light management techniques (dielectric–metal–dielectric electrodes, periodic 1D dielectric mirrors, optical microcavity design, OC layers, and antireflection coatings) enhance the optical properties of solar cells at the expense of added cost and processing times. Given the potential of these light trapping techniques, it is imperative that these approaches are mainstreamed in the design of an STPV device and are not limited only to STOPV or STPSC.

Table 2. A comparison table of different STPV technologies.

	a-Si	CdTe	CIGS	PSC	OSC	DSSC
Record PCE ^{a)}	14.0 ^[362]	22.3 ^[6]	23.6 ^[6]	26.0 ^[6]	19.3 ^[7]	14.2 ^[8]
Stability [%/year]	0.87 ^[363]	0.40 ^[363]	0.96 ^[363]	10 ^[364]	10 ^[365]	10 ^[366]
Highest LUE	1.88 ^[66]	1.00 ^[58]	1.69 ^[142]	4.44 ^[113]	5.0 ^[122] /5.7 [#] ^[146]	2.64 ^[46]
Material abundance ^{b)}	High	Te-limited	In-limited	High	High	High
Module price [\$ W ⁻¹] ^{c)}	0.115 ^[367]	0.28, ^[348] 0.40 ^[361]	0.48 ^[348]	0.38, ^[348] 0.115–0.23, ^[367] 0.41, ^[347] 0.38 ^[349]	0.2–1.2 ^[10]	0.46, ^[367] 0.18 ^[361]
Aesthetics ^{d)}	Limited	Limited	Limited	Medium	Very high	High

^{a)} In opaque devices; ^{b)} Cost considers material abundance and processing cost; ^{c)} MSP (with 15% gross margin assumed) of standard opaque modules; ^{d)} tunability of parameters like CRI and CCT. [#] Tandem with PSC.

Scale-up, Stability, and Cost: The scaling gap and stability issues (especially for the third-generation technologies) will need breakthrough improvements to compete with traditional semi-transparent thin film solar cells. However, niche applications such as indoor and low-power photovoltaics would not demand high standards of stability tests, and a good encapsulation would be enough in many cases. Nevertheless, when the LUE values reach the acceptable threshold on large area devices/modules, comparison between different STPV technologies should be based on several other parameters included in LCOE, such as energy consumption during device/module processing and the cost of the materials.

In summary, LUE, stability, scalability, and cost are the principal aspects that should be satisfied simultaneously to reach the commercialization stage. LUEs for emerging STPVs (STOPVs, STPSCs, and STDSSCs) are higher than conventional thin-film solar cells and meet the requirements for BIPV applications (Figure 2b and Table 2). However, the current benchmark for reliability is based on commercial silicon solar modules with lifetimes over 25 years at low cost of $< \$0.25 \text{ W}^{-1}$. Silicon solar cells never faced inherent material degradation issues under outdoor operational conditions in contrast to the absorbers used in third-generation STPVs. Therefore, stability standards could be relaxed for third-generation STPV technologies (say, 10 years of T_{80} lifetime in real-life conditions instead of 25), because they offer niche applications on currently unexplored areas (such as windows, facades, and so on). Finally, even if LUE and stability reach satisfactory levels, the challenges in large-area scaling at module levels ($> 1 \text{ m}^2$) cannot be extrapolated based on small-area lab-scale devices. Considerable research efforts are being put toward reducing the scalability gap in opaque solar modules. At the current stage, research on STPVs should focus on achieving the highest LUEs possible (theoretical maximum LUE = 21),^[25] while adding minimum complexity (additional steps) compared to the opaque counterparts. Lab-to-fab transition of these STPV technologies will follow their progress in the opaque form.

Acknowledgements

A.V. acknowledges the Knut & Alice Wallenberg Foundation and the Kempe Foundation for financial support.

Conflict of Interest

The authors declare no conflict of interest.

Keywords

building integrated photovoltaics, semitransparent solar cells, transparent conductive electrodes, visible light transmittance

Received: May 22, 2023

Revised: July 10, 2023

Published online: September 5, 2023

[1] T. E. Kuhn, C. Erban, M. Heinrich, J. Eisenlohr, F. Ensslen, D. H. Neuhaus, *Energy Build.* **2021**, *231*, 110381.

- [2] P. J. Verlinden, *J. Renewable Sustainable Energy* **2020**, *12*, 053505.
- [3] K. Yoshikawa, H. Kawasaki, W. Yoshida, T. Irie, K. Konishi, K. Nakano, T. Uto, D. Adachi, M. Kanematsu, H. Uzu, K. Yamamoto, *Nat. Energy* **2017**, *2*, 17032.
- [4] M. Green, E. Dunlop, J. Hohl-Ebinger, M. Yoshita, N. Kopidakis, X. Hao, *Prog. Photovoltaics* **2021**, *29*, 3.
- [5] T. Matsui, A. Bidiville, K. Maejima, H. Sai, T. Koida, T. Suezaki, M. Matsumoto, K. Saito, I. Yoshida, M. Kondo, *Appl. Phys. Lett.* **2015**, *106*, 053901.
- [6] M. A. Green, E. D. Dunlop, M. Yoshita, N. Kopidakis, K. Bothe, G. Siefer, X. Hao, *Prog. Photovoltaics* **2023**, *31*, 3.
- [7] L. Zhu, M. Zhang, J. Xu, C. Li, J. Yan, G. Zhou, W. Zhong, T. Hao, J. Song, X. Xue, Z. Zhou, R. Zeng, H. Zhu, C.-C. Chen, R. C. I. MacKenzie, Y. Zou, J. Nelson, Y. Zhang, Y. Sun, F. Liu, *Nat. Mater.* **2022**, *21*, 656.
- [8] J.-M. Ji, H. Zhou, Y. K. Eom, C. H. Kim, H. K. Kim, *Adv. Energy Mater.* **2020**, *10*, 2000124.
- [9] F. Ise, Photovoltaics Report – Fraunhofer ISE, <https://www.ise.fraunhofer.de/en/publications/studies/photovoltaics-report.html> (accessed: July 2021).
- [10] B. Lee, L. Lahann, Y. Li, S. R. Forrest, *Sustainable Energy Fuels* **2020**, *4*, 5765.
- [11] M. Lu, J. H. K. Lai, *Energy Procedia* **2019**, *158*, 3633.
- [12] L. Belussi, B. Barozzi, A. Bellazzi, L. Danza, A. Devitofrancesco, C. Fanciulli, M. Ghellere, G. Guazzi, I. Meroni, F. Salamone, F. Scamoni, C. Scrosati, *J. Build. Eng.* **2019**, *25*, 100772.
- [13] A. Ghosh, *J. Cleaner Prod.* **2020**, *276*, 123343.
- [14] A. Scognamiglio, H. N. Røstvik, *Prog. Photovoltaics* **2013**, *21*, 1319.
- [15] B. Shi, L. Duan, Y. Zhao, J. Luo, X. Zhang, *Adv. Mater.* **2020**, *32*, 1806474.
- [16] M. Batmunkh, Y. L. Zhong, H. Zhao, *Adv. Mater.* **2020**, *32*, 2000631.
- [17] Building-integrated Photovoltaics Market Report, 2021–2028, <https://www.grandviewresearch.com/industry-analysis/building-integrated-photovoltaics-bipv-market> (accessed: July 2021).
- [18] E. Biyik, M. Araz, A. Hepbasli, M. Shahrestani, R. Yao, L. Shao, E. Essah, A. C. Oliveira, T. del Caño, E. Rico, J. L. Lechón, L. Andrade, A. Mendes, Y. B. Atli, *Eng. Sci. Technol. Int. J.* **2017**, *20*, 833.
- [19] B. Petter Jelle, C. Breivik, H. D. Røkenes, *Sol. Energy Mater. Sol. Cells* **2012**, *100*, 69.
- [20] C. Ballif, L.-E. Perret-Aebi, S. Lufkin, E. Rey, *Nat. Energy* **2018**, *3*, 438.
- [21] M. R. Cibi, S. Manikandan, *IOP Conf. Ser.: Mater. Sci. Eng.* **2021**, *1130*, 012033.
- [22] Z. Li, T. Ma, H. Yang, L. Lu, R. Wang, *Sol. RRL* **2021**, *5*, 2000614.
- [23] C. J. Traverse, R. Pandey, M. C. Barr, R. R. Lunt, *Nat. Energy* **2017**, *2*, 849.
- [24] S. Han, Y. Deng, W. Han, G. Ren, Z. Song, C. Liu, W. Guo, *Sol. Energy* **2021**, *225*, 97.
- [25] R. R. Lunt, *Appl. Phys. Lett.* **2012**, *101*, 043902.
- [26] S. Westland, in *Handbook of Visual Display Technology* (Eds: J. Chen, W. Cranton, M. Fihn), Springer, Berlin, Heidelberg **2012**, pp. 139.
- [27] E. P.-S. José, A. Sánchez-Díaz, M. Stella, E. Martínez-Ferrero, M. I. Alonso, M. Campoy-Quiles, *Sci. Technol. Adv. Mater.* **2018**, *19*, 823.
- [28] Z. Hu, J. Wang, X. Ma, J. Gao, C. Xu, K. Yang, Z. Wang, J. Zhang, F. Zhang, *Nano Energy* **2020**, *78*, 105376.
- [29] A. Røyset, T. Kolås, B. P. Jelle, *Energy Build.* **2020**, *208*, 109623.
- [30] A. Roy, A. Ghosh, S. Bhandari, P. Selvaraj, S. Sundaram, T. K. Mallick, *J. Phys. Chem. C* **2019**, *123*, 23834.
- [31] N. Lynn, L. Mohanty, S. Wittkopf, *Build. Environ.* **2012**, *54*, 148.
- [32] C. S. McCamy, *Color Res. Appl.* **1992**, *17*, 142.
- [33] M. Saifullah, J. Gwak, J. H. Yun, *J. Mater. Chem. A* **2016**, *4*, 8512.
- [34] J. Sun, J. J. Jasieniak, *J. Phys. D: Appl. Phys.* **2017**, *50*, 093001.
- [35] Q. Tai, F. Yan, *Adv. Mater.* **2017**, *29*, 1700192.
- [36] S.-Y. Chang, P. Cheng, G. Li, Y. Yang, *Joule* **2018**, *2*, 1039.

- [37] A. A. F. Husain, W. Z. W. Hasan, S. Shafie, M. N. Hamidon, S. S. Pandey, *Renewable Sustainable Energy Rev.* **2018**, *94*, 779.
- [38] D. H. Shin, S.-H. Choi, *Coatings* **2018**, *8*, 329.
- [39] Q. Xue, R. Xia, C. J. Brabec, H.-L. Yip, *Energy Environ. Sci.* **2018**, *11*, 1688.
- [40] K. Lee, H.-D. Um, D. Choi, J. Park, N. Kim, H. Kim, K. Seo, *Cell Rep. Phys. Sci.* **2020**, *1*, 100143.
- [41] Y. Dong, H. Gao, R. Yu, Y. Gong, Z. Ma, Z. Tan, *Phys. Status Solidi A* **2022**, *219*, 2100731.
- [42] L. Liu, K. Cao, S. Chen, W. Huang, *Adv. Opt. Mater.* **2020**, *8*, 2001122.
- [43] C.-C. Chen, L. Dou, R. Zhu, C.-H. Chung, T.-B. Song, Y. B. Zheng, S. Hawks, G. Li, P. S. Weiss, Y. Yang, *ACS Nano* **2012**, *6*, 7185.
- [44] J. H. Heo, H. J. Han, M. Lee, M. Song, D. H. Kim, S. H. Im, *Energy Environ. Sci.* **2015**, *8*, 2922.
- [45] K. Lee, N. Kim, K. Kim, H.-D. Um, W. Jin, D. Choi, J. Park, K. J. Park, S. Lee, K. Seo, *Joule* **2020**, *4*, 235.
- [46] D. A. Chalkias, C. Charalampopoulos, A. K. Andreopoulou, A. Karavioti, E. Stathatos, *J. Power Sources* **2021**, *496*, 229842.
- [47] W. Naim, V. Novelli, I. Nikolinakos, N. Barbero, I. Dzeba, F. Grifoni, Y. Ren, T. Alnasser, A. Velardo, R. Borrelli, S. Haacke, S. M. Zakeeruddin, M. Graetzel, C. Barolo, F. Sauvage, *JACS Au* **2021**, *1*, 409.
- [48] Y. Li, X. Guo, Z. Peng, B. Qu, H. Yan, H. Ade, M. Zhang, S. R. Forrest, *Proc Natl Acad Sci U S A* **2020**, *117*, 21147.
- [49] C. Sun, R. Xia, H. Shi, H. Yao, X. Liu, J. Hou, F. Huang, H.-L. Yip, Y. Cao, *Joule* **2018**, *2*, 1816.
- [50] R. Xia, C. J. Brabec, H.-L. Yip, Y. Cao, *Joule* **2019**, *3*, 2241.
- [51] S. Kuk, Z. Wang, H. Yu, C.-Y. Nam, J. Jeong, D. Hwang, *Prog. Photovoltaics* **2020**, *28*, 135.
- [52] K. Wang, G. Xing, Q. Song, S. Xiao, *Adv. Mater.* **2021**, *33*, 2000306.
- [53] H.-C. Kwon, S. Ma, S.-C. Yun, G. Jang, H. Yang, J. Moon, *J. Mater. Chem. A* **2020**, *8*, 1457.
- [54] M. Rai, S. Rahmany, S. S. Lim, S. Magdassi, L. H. Wong, L. Etgar, *J. Mater. Chem. A* **2018**, *6*, 23787.
- [55] J. H. Heo, M. H. Jang, M. H. Lee, H. J. Han, M. G. Kang, M. L. Lee, S. H. Im, *J. Mater. Chem. A* **2016**, *4*, 16324.
- [56] M. T. Hörantner, W. Zhang, M. Saliba, K. Wojciechowski, H. J. Snaith, *Energy Environ. Sci.* **2015**, *8*, 2041.
- [57] G. E. Eperon, V. M. Burlakov, A. Gorieli, H. J. Snaith, *ACS Nano* **2014**, *8*, 591.
- [58] Domestic Glass Specifications, https://www.polysolar.co.uk/technology/_domestic-info-specifications
- [59] W. Zhang, L. Lu, J. Peng, A. Song, *Energy Build.* **2016**, *128*, 511.
- [60] S. Berny, N. Blouin, A. Distler, H.-J. Egelhaaf, M. Krompiec, A. Lohr, O. R. Lozman, G. E. Morse, L. Nanson, A. Pron, T. Sauermann, N. Seidler, S. Tierney, P. Tiwana, M. Wagner, H. Wilson, *Adv. Sci.* **2016**, *3*, 1500342.
- [61] J. Peng, D. C. Curcija, A. Thanachareonkit, E. S. Lee, H. Goudey, S. E. Selkowitz, *Appl. Energy* **2019**, *242*, 854.
- [62] X. Liu, Z. Zhong, R. Zhu, J. Yu, G. Li, *Joule* **2022**, *6*, 1918.
- [63] K. Fukutani, M. Kanbe, W. Futako, B. Kaplan, T. Kamiya, C. M. Fortmann, I. Shimizu, *J. Non-Cryst. Solids* **1998**, *227–230*, 63.
- [64] J. Kim, J. W. Lim, G. Kim, M. Shin, *ACS Appl. Mater. Interfaces* **2021**, *13*, 4968.
- [65] J.-S. Cho, Y. H. Seo, B.-H. Choi, A. Lee, M. J. Shin, A. Cho, S. Ahn, J. Yoo, J. H. Park, K. Kim, D. Shin, S. Lee, S. Ahn, *ACS Appl. Mater. Interfaces* **2020**, *12*, 29194.
- [66] J. Yang, H. Jo, S.-W. Choi, D.-W. Kang, J.-D. Kwon, *J. Mater. Sci. Technol.* **2019**, *35*, 1563.
- [67] J. Wook Lim, M. Shin, D. J. Lee, S. Hyun Lee, S. Jin Yun, *Sol. Energy Mater. Sol. Cells* **2014**, *128*, 301.
- [68] L.-M. Huang, C.-W. Hu, H.-C. Liu, C.-Y. Hsu, C.-H. Chen, K.-C. Ho, *Sol. Energy Mater. Sol. Cells* **2012**, *99*, 154.
- [69] H. Maurus, M. Schmid, B. Bleresch, P. Lechner, H. Schade, *Refocus* **2004**, *5*, 22.
- [70] J.-S. Cho, Y. H. Seo, B.-H. Choi, A. Cho, A. Lee, M. J. Shin, K. Kim, S. K. Ahn, J. H. Park, J. Yoo, D. Shin, I. Jeong, J. Gwak, *Sol. Energy Mater. Sol. Cells* **2019**, *202*, 110078.
- [71] J. W. Lim, S. H. Lee, D. J. Lee, Y. J. Lee, S. J. Yun, *Thin Solid Films* **2013**, *547*, 212.
- [72] G. Kim, J. W. Lim, M. Shin, S. J. Yun, *Sol. Energy* **2018**, *159*, 465.
- [73] M. J. Shin, A. Lee, A. Cho, K. Kim, S. K. Ahn, J. H. Park, J. Yoo, J. H. Yun, J. Gwak, D. Shin, I. Jeong, J.-S. Cho, *Nano Energy* **2021**, *82*, 105729.
- [74] V. V. Plotnikov, C. W. Carter, J. M. Stayancho, A. D. Compaan, *US2014000690A1*, **2014**.
- [75] V. V. Plotnikov, C. W. Carter, J. M. Stayancho, N. R. Paudel, H. Mahabaduge, D. Kwon, C. R. Grice, A. D. Compaan, in *2013 IEEE 39th Photovoltaic Specialists Conference (PVSC)*, IEEE, Piscataway, NJ **2013**, pp. 0405–0408.
- [76] N. R. Paudel, K. A. Wieland, A. D. Compaan, *Sol. Energy Mater. Sol. Cells* **2012**, *105*, 109.
- [77] V. Plotnikov, X. Liu, N. Paudel, D. Kwon, K. A. Wieland, A. D. Compaan, *Thin Solid Films* **2011**, *519*, 7134.
- [78] N. R. Paudel, K. A. Wieland, A. D. Compaan, in *2011 37th IEEE Photovoltaic Specialists Conference*, IEEE, Seattle, WA **2011**, pp. 002784–002786.
- [79] M. Saifullah, S. Ahn, J. Gwak, S. Ahn, K. Kim, J. Cho, J. H. Park, Y. J. Eo, A. Cho, J.-S. Yoo, J. H. Yun, *J. Mater. Chem. A* **2016**, *4*, 10542.
- [80] W. K. Metzger, S. Grover, D. Lu, E. Colegrove, J. Moseley, C. L. Perkins, X. Li, R. Mallick, W. Zhang, R. Malik, J. Kephart, C.-S. Jiang, D. Kuciauskas, D. S. Albin, M. M. Al-Jassim, G. Xiong, M. Gloeckler, *Nat. Energy* **2019**, *4*, 837.
- [81] L. A. Kosyachenko, X. Mathew, V. Ya Roshko, E. V. Grushko, *Sol. Energy Mater. Sol. Cells* **2013**, *114*, 179.
- [82] E. W. Jones, V. Barrioz, S. J. C. Irvine, D. Lamb, *Thin Solid Films* **2009**, *517*, 2226.
- [83] A. Gupta, V. Parikh, A. D. Compaan, *Sol. Energy Mater. Sol. Cells* **2006**, *90*, 2263.
- [84] M. J. Heben, A. B. Phillips, R. R. Khanal, V. V. Plotnikov, A. D. Compaan, *US10043922B2*, **2018**.
- [85] A. Romeo, E. Artagiani, *Energies* **2021**, *14*, 1684.
- [86] V. Fthenakis, *Renewable Sustainable Energy Rev.* **2009**, *13*, 2746.
- [87] W. Meng, P. Jinqing, Y. Hongxing, L. Yimo, *Energy Procedia* **2018**, *152*, 1091.
- [88] T. A. M. Fiducia, B. G. Mendis, K. Li, C. R. M. Grovenor, A. H. Munshi, K. Barth, W. S. Sampath, L. D. Wright, A. Abbas, J. W. Bowers, J. M. Walls, *Nat. Energy* **2019**, *4*, 504.
- [89] N. Kumari, S. K. Singh, S. Kumar, *Mater Today Proc* **2022**, *66*, 3552.
- [90] M. Nakamura, K. Yamaguchi, Y. Kimoto, Y. Yasaki, T. Kato, H. Sugimoto, *IEEE J. Photovoltaics* **2019**, *9*, 1863.
- [91] R. Carron, S. Nishiwaki, T. Feurer, R. Hertwig, E. Avancini, J. Löckinger, S.-C. Yang, S. Buecheler, A. N. Tiwari, *Adv. Energy Mater.* **2019**, *9*, 1900408.
- [92] M. Bär, W. Bohne, J. Röhrich, E. Strub, S. Lindner, M. C. Lux-Steiner, Ch.-H. Fischer, T. P. Niesen, F. Karg, *J. Appl. Phys.* **2004**, *96*, 3857.
- [93] K.-J. Hsiao, J.-D. Liu, H.-H. Hsieh, T.-S. Jiang, *Phys. Chem. Chem. Phys.* **2013**, *15*, 18174.
- [94] J.-H. Yoon, S. Cho, W. M. Kim, J.-K. Park, Y.-J. Baik, T. S. Lee, T.-Y. Seong, J. Jeong, *Sol. Energy Mater. Sol. Cells* **2011**, *95*, 2959.
- [95] K. Orgassa, H. W. Schock, J. H. Werner, *Thin Solid Films* **2003**, *431–432*, 387.
- [96] F. Mollica, M. Jubault, F. Donsanti, A. Loubat, M. Bouttemy, A. Etcheberry, N. Naghavi, *Thin Solid Films* **2017**, *633*, 202.
- [97] C. Zhu, W. Liu, Y. Li, X. Huo, H. Li, K. Guo, B. Qiao, S. Zhao, Z. Xu, H. Zhao, D. Song, *Sol. Energy* **2021**, *228*, 45.

- [98] L. M. Mansfield, R. Noufi, C. P. Muzzillo, C. DeHart, K. Bowers, B. To, J. W. Pankow, R. C. Reedy, K. Ramanathan, *IEEE J. Photovoltaics* **2014**, *4*, 1650.
- [99] T. Nakada, *Thin Solid Films* **2005**, *480–481*, 419.
- [100] W. Li, L. Yao, K. Li, X. Li, B. Yang, S. Xu, S. Shi, C. Yi, M. Chen, Y. Feng, W. Li, Z. Lu, C. Yang, *ACS Appl. Energy Mater.* **2020**, *3*, 4201.
- [101] M. Mazzer, S. Rampino, G. Spaggiari, F. Annoni, D. Bersani, F. Bissoli, M. Bronzoni, M. Calicchio, E. Gombia, A. Kingma, F. Pattini, E. Gilioli, *Sol. Energy Mater. Sol. Cells* **2017**, *166*, 247.
- [102] M. Mazzer, S. Rampino, E. Gombia, M. Bronzoni, F. Bissoli, F. Pattini, M. Calicchio, A. Kingma, F. Annoni, D. Calestani, N. Cavallari, V. Thottapurath Vijayan, M. Lomascolo, A. Cretì, E. Gilioli, *Energies* **2016**, *9*, 207.
- [103] A. Han, Y. Zhang, W. Song, B. Li, W. Liu, Y. Sun, *Semicond. Sci. Technol.* **2012**, *27*, 035022.
- [104] P. Shen, G. Wang, B. Kang, W. Guo, L. Shen, *ACS Appl. Mater. Interfaces* **2018**, *10*, 6513.
- [105] W. Yu, X. Fu, K. Dong, *J. Mater. Sci.: Mater. Electron.* **2021**, *32*, 13409.
- [106] G. M. Kim, T. Tatsuma, *Sci. Rep.* **2017**, *7*, 10699.
- [107] M. Mujahid, C. Chen, J. Zhang, C. Li, Y. Duan, *InfoMat* **2021**, *3*, 101.
- [108] A. Roy, A. Ghosh, S. Bhandari, S. Sundaram, T. K. Mallick, *Buildings* **2020**, *10*, 129.
- [109] S. Rahmany, L. Etgar, *ACS Energy Lett.* **2020**, *5*, 1519.
- [110] H.-C. Kwon, J. Moon, *Curr. Opin. Electrochem.* **2018**, *11*, 114.
- [111] S.-H. Lim, H.-J. Seok, D.-H. Choi, S.-K. Kim, D.-H. Kim, H.-K. Kim, *ACS Appl. Mater. Interfaces* **2021**, *13*, 27353.
- [112] Y. Zhu, L. Shu, Q. Zhang, Y. Zhu, S. Poddar, C. Wang, Z. He, Z. Fan, *EcoMat* **2021**, *3*, e12117.
- [113] M. Wang, F. Cao, M. Wang, K. Deng, L. Li, *Adv. Mater.* **2021**, *33*, 2006745.
- [114] J.-H. Lu, Y.-L. Yu, S.-R. Chuang, C.-H. Yeh, C.-P. Chen, *J. Phys. Chem. C* **2016**, *120*, 4233.
- [115] Y. Jiang, B. Luo, F. Jiang, F. Jiang, C. Fuentes-Hernandez, T. Liu, L. Mao, S. Xiong, Z. Li, T. Wang, B. Kippelen, Y. Zhou, *Nano Lett.* **2016**, *16*, 7829.
- [116] J. Lin, M. Lai, L. Dou, C. S. Kley, H. Chen, F. Peng, J. Sun, D. Lu, S. A. Hawks, C. Xie, F. Cui, A. P. Alivisatos, D. T. Limmer, P. Yang, *Nature Mater* **2018**, *17*, 261.
- [117] H. Kim, H.-S. Kim, J. Ha, N.-G. Park, S. Yoo, *Adv. Energy Mater.* **2016**, *6*, 1502466.
- [118] Y. (Michael) Yang, Q. Chen, Y.-T. Hsieh, T.-B. Song, N. D. Marco, H. Zhou, Y. Yang, *ACS Nano* **2015**, *9*, 7714.
- [119] E. Della Gaspera, Y. Peng, Q. Hou, L. Spiccia, U. Bach, J. J. Jasieniak, Y.-B. Cheng, *Nano Energy* **2015**, *13*, 249.
- [120] S. Han, S. Lim, H. Kim, H. Cho, S. Yoo, *IEEE J. Sel. Top. Quantum Electron.* **2010**, *16*, 1656.
- [121] D. Han, S. Lee, H. Kim, S. Jeong, S. Yoo, *Org. Electron.* **2013**, *14*, 1477.
- [122] S. Guan, Y. Li, K. Yan, W. Fu, L. Zuo, H. Chen, *Adv. Mater.* **2022**, *34*, 2205844.
- [123] L. Lucera, F. Machui, H. D. Schmidt, T. Ahmad, P. Kubis, S. Strohm, J. Hepp, A. Vetter, H.-J. Egelhaaf, C. J. Brabec, *Org. Electron.* **2017**, *45*, 209.
- [124] J. Zhang, G. Xu, F. Tao, G. Zeng, M. Zhang, Y. (Michael) Yang, Y. Li, Y. Li, *Adv. Mater.* **2019**, *31*, 1807159.
- [125] Y. Xie, R. Xia, T. Li, L. Ye, X. Zhan, H.-L. Yip, Y. Sun, *Small Methods* **2019**, *3*, 1900424.
- [126] J. Chen, G. Li, Q. Zhu, X. Guo, Q. Fan, W. Ma, M. Zhang, *J. Mater. Chem. A* **2019**, *7*, 3745.
- [127] X. Ma, Z. Xiao, Q. An, M. Zhang, Z. Hu, J. Wang, L. Ding, F. Zhang, *J. Mater. Chem. A* **2018**, *6*, 21485.
- [128] H. Yao, Y. Cui, R. Yu, B. Gao, H. Zhang, J. Hou, *Angew. Chem., Int. Ed.* **2017**, *56*, 3045.
- [129] D. Wang, R. Qin, G. Zhou, X. Li, R. Xia, Y. Li, L. Zhan, H. Zhu, X. Lu, H.-L. Yip, H. Chen, C.-Z. Li, *Adv. Mater.* **2020**, *32*, 2001621.
- [130] R. Betancur, P. Romero-Gomez, A. Martinez-Otero, X. Elias, M. Maymó, J. Martorell, *Nat. Photonics* **2013**, *7*, 995.
- [131] X. Huang, Y. Cheng, Y. Fang, L. Zhang, X. Hu, S. Y. Jeong, H. Zhang, H. Y. Woo, F. Wu, L. Chen, *Energy Environ. Sci.* **2022**, *15*, 4776.
- [132] G. P. Kini, S. J. Jeon, D. K. Moon, *Adv. Funct. Mater.* **2021**, *31*, 2007931.
- [133] E. Ravishankar, R. E. Booth, C. Saravitz, H. Sederoff, H. W. Ade, B. T. O'Connor, *Joule* **2020**, *4*, 490.
- [134] M.-E. Yeoh, K.-Y. Chan, *IEEE J. Photovoltaics* **2021**, *11*, 354.
- [135] K. Basu, G. S. Selopal, M. Mohammadnezad, R. Akilimali, Z. M. Wang, H. Zhao, F. Vetrone, F. Rosei, *Electrochim. Acta* **2020**, *349*, 136409.
- [136] K. Zhang, C. Qin, X. Yang, A. Islam, S. Zhang, H. Chen, L. Han, *Adv. Energy Mater.* **2014**, *4*, 1301966.
- [137] M. Godfroy, J. Liotier, V. M. Mwalukuku, D. Joly, Q. Huaulmé, L. Cabau, C. Aumaitre, Y. Kervella, S. Narbey, F. Oswald, E. Palomares, C. A. G. Flores, G. Oskam, R. Demadrille, *Sustainable Energy Fuels* **2021**, *5*, 144.
- [138] S. Venkatesan, W.-H. Lin, H. Teng, Y.-L. Lee, *ACS Appl. Mater. Interfaces* **2019**, *11*, 42780.
- [139] M. I. Asghar, K. Miettunen, J. Halme, P. Vahermaa, M. Toivola, K. Aitola, P. Lund, *Energy Environ. Sci.* **2010**, *3*, 418.
- [140] A. Ghosh, P. Selvaraj, S. Sundaram, T. K. Mallick, *Sol. Energy* **2018**, *163*, 537.
- [141] B.-X. Chen, H.-S. Rao, H.-Y. Chen, W.-G. Li, D.-B. Kuang, C.-Y. Su, *J. Mater. Chem. A* **2016**, *4*, 15662.
- [142] A. Jeong, J. M. Choi, H.-J. Lee, G. Y. Kim, J.-K. Park, W. M. Kim, S. Kuk, Z. Wang, D. J. Hwang, H. Yu, J. Jeong, *Prog. Photovoltaics* **2022**, *30*, 713.
- [143] H. J. Lee, J. K. Park, D. S. Lee, S. Choi, S. Y. Hong, J. H. Heo, S. H. Im, *ACS Appl. Energy Mater.* **2022**, *5*, 3660.
- [144] J. Zhao, N. Chai, X. Chen, Y. Yue, Y.-B. Cheng, J. Qiu, X. Wang, *Nanophotonics* **2022**, *11*, 987.
- [145] T. Leijtens, K. A. Bush, R. Prasanna, M. D. McGehee, *Nat. Energy* **2018**, *3*, 828.
- [146] L. Zuo, X. Shi, W. Fu, A. K.-Y. Jen, *Adv. Mater.* **2019**, *31*, 1901683.
- [147] M. Jošt, E. Köhnen, A. Al-Ashouri, T. Bertram, Š. Tomšič, A. Magomedov, E. Kasparavicius, T. Kodalle, B. Lipovšek, V. Getautis, R. Schlattmann, C. A. Kaufmann, S. Albrecht, M. Topič, *ACS Energy Lett.* **2022**, *7*, 1298.
- [148] D. Rossi, K. Forberich, F. Matteocci, M. Auf der Maur, H.-J. Egelhaaf, C. J. Brabec, A. Di Carlo, *Sol. RRL* **2022**, *6*, 2200242.
- [149] H. Li, W. Zhang, *Chem. Rev.* **2020**, *120*, 9835.
- [150] H. Wu, Y. Cheng, J. Ma, J. Zhang, Y. Zhang, Y. Song, S. Peng, *Adv. Mater.* **2023**, *35*, 2206574.
- [151] S. P. Bremner, M. Y. Levy, C. B. Honsberg, *Prog. Photovoltaics* **2008**, *16*, 225.
- [152] W. Chen, Y. Zhu, J. Xiu, G. Chen, H. Liang, S. Liu, H. Xue, E. Birgersson, J. W. Ho, X. Qin, J. Lin, R. Ma, T. Liu, Y. He, A. M.-C. Ng, X. Guo, Z. He, H. Yan, A. B. Djurišić, Y. Hou, *Nat. Energy* **2022**, *7*, 229.
- [153] R. Lin, Y. Wang, Q. Lu, B. Tang, J. Li, H. Gao, Y. Gao, H. Li, C. Ding, J. Wen, P. Wu, C. Liu, S. Zhao, K. Xiao, Z. Liu, C. Ma, Y. Deng, L. Li, F. Fan, H. Tan, *Nature* **2023**, *603*, 73.
- [154] J. Kwon, M. J. Im, C. U. Kim, S. H. Won, S. B. Kang, S. H. Kang, I. T. Choi, H. K. Kim, I. H. Kim, J. H. Park, K. J. Choi, *Energy Environ. Sci.* **2016**, *9*, 3657.
- [155] S. Chen, H. Yao, B. Hu, G. Zhang, L. Arunagiri, L.-K. Ma, J. Huang, J. Zhang, Z. Zhu, F. Bai, W. Ma, H. Yan, *Adv. Energy Mater.* **2018**, *8*, 1800529.
- [156] C.-C. Chen, L. Dou, J. Gao, W.-H. Chang, G. Li, Y. Yang, *Energy Environ. Sci.* **2013**, *6*, 2714.

- [157] X. Xiao, K. Lee, S. R. Forrest, *Appl. Phys. Lett.* **2015**, *107*, 033901.
- [158] T. Jiang, G. Zhang, R. Xia, J. Huang, X. Li, M. Wang, H.-L. Yip, Y. Cao, *Mater. Today Energy* **2021**, *21*, 100807.
- [159] M. W. Rowell, M. D. McGehee, *Energy Environ. Sci.* **2010**, *4*, 131.
- [160] F. Bonaccorso, Z. Sun, T. Hasan, A. C. Ferrari, *Nat. Photonics* **2010**, *4*, 611.
- [161] Y. Zhang, S.-W. Ng, X. Lu, Z. Zheng, *Chem. Rev.* **2020**, *120*, 2049.
- [162] M. Morales-Masis, S. D. Wolf, R. Woods-Robinson, J. W. Ager, C. Ballif, *Adv. Electron. Mater.* **2017**, *3*, 1600529.
- [163] H. H. Park, *Electron. Mater. Lett.* **2021**, *17*, 18.
- [164] H. Kanda, A. Uzum, A. K. Baranwal, T. A. N. Peiris, T. Umeyama, H. Imahori, H. Segawa, T. Miyasaka, S. Ito, *J. Phys. Chem. C* **2016**, *120*, 28441.
- [165] L. Cai, F. Zhu, *Nano Select* **2021**, *2*, 1417.
- [166] Z. Wei, B. Smith, F. D. Rossi, J. R. Searle, D. A. Worsley, T. M. Watson, *J. Mater. Chem. C* **2019**, *7*, 10981.
- [167] Z. Yang, A. Rajagopal, C.-C. Chueh, S. B. Jo, B. Liu, T. Zhao, A. K.-Y. Jen, *Adv. Mater.* **2016**, *28*, 8990.
- [168] S. Zhu, X. Yao, Q. Ren, C. Zheng, S. Li, Y. Tong, B. Shi, S. Guo, L. Fan, H. Ren, C. Wei, B. Li, Y. Ding, Q. Huang, Y. Li, Y. Zhao, X. Zhang, *Nano Energy* **2018**, *45*, 280.
- [169] R. E. I. Schropp, K. Adachi, N. Imajyo, J. A. D. Cueto, P. K. Bhat, A. Madan, *MRS Online Proc. Libr.* **1989**, *149*, 429.
- [170] S.-H. Lim, H.-J. Seok, M.-J. Kwak, D.-H. Choi, S.-K. Kim, D.-H. Kim, H.-K. Kim, *Nano Energy* **2021**, *82*, 105703.
- [171] Y. Bai, C. Zhao, X. Chen, S. Zhang, S. Zhang, T. Hayat, A. Alsaedi, Z. Tan, J. Hou, Y. Li, *J. Mater. Chem. A* **2019**, *7*, 15887.
- [172] Y. Xu, Z. Lin, W. Wei, Y. Hao, S. Liu, J. Ouyang, J. Chang, *Nano-Micro Lett.* **2022**, *14*, 117.
- [173] Y. Xu, J. Wang, L. Sun, H. Huang, J. Han, H. Huang, L. Zhai, C. Zou, *J. Mater. Chem. C* **2021**, *9*, 9102.
- [174] C. Tao, G. Xie, C. Liu, X. Zhang, W. Dong, F. Meng, X. Kong, L. Shen, S. Ruan, W. Chen, *Appl. Phys. Lett.* **2009**, *95*, 053303.
- [175] F. Guo, N. Li, V. V. Radmilović, V. R. Radmilović, M. Turbiez, E. Spiecker, K. Forberich, C. J. Brabec, *Energy Environ. Sci.* **2015**, *8*, 1690.
- [176] T. Tokuno, M. Nogi, M. Karakawa, J. Jiu, T. T. Nge, Y. Aso, K. Suganuma, *Nano Res.* **2011**, *4*, 1215.
- [177] S. A. Abbasi, Z. Chai, A. Busnaina, *Adv. Mater. Interfaces* **2019**, *6*, 1900898.
- [178] Y. Dou, Z. Liu, Z. Wu, Y. Liu, J. Li, C. Leng, D. Fang, G. Liang, J. Xiao, W. Li, X. Wei, F. Huang, Y.-B. Cheng, J. Zhong, *Nano Energy* **2020**, *71*, 104567.
- [179] M. Parente, M. van Helvert, R. F. Hamans, R. Verbroekken, R. Sinha, A. Bieberle-Hütter, A. Baldi, *Nano Lett.* **2020**, *20*, 5759.
- [180] J.-Y. Lee, S. T. Connor, Y. Cui, P. Peumans, *Nano Lett.* **2008**, *8*, 689.
- [181] Z. Niu, F. Cui, E. Kuttner, C. Xie, H. Chen, Y. Sun, A. Dehestani, K. Schierle-Arndt, P. Yang, *Nano Lett.* **2018**, *18*, 5329.
- [182] D. Langley, G. Giusti, C. Mayousse, C. Celle, D. Bellet, J.-P. Simonato, *Nanotechnology* **2013**, *24*, 452001.
- [183] M.-G. Kang, M.-S. Kim, J. Kim, L. J. Guo, *Adv. Mater.* **2008**, *20*, 4408.
- [184] R. Saive, A. M. Borsuk, H. S. Emmer, C. R. Bukowsky, J. V. Lloyd, S. Yalamanchili, H. A. Atwater, *Adv. Opt. Mater.* **2016**, *4*, 1470.
- [185] F. Guo, H. Azimi, Y. Hou, T. Przybilla, M. Hu, C. Bronnbauer, S. Langner, E. Spiecker, K. Forberich, C. J. Brabec, *Nanoscale* **2015**, *7*, 1642.
- [186] T. Gahlmann, K. O. Brinkmann, T. Becker, C. Tüchtmantel, C. Kreuzel, F. van gen Hassend, S. Weber, T. Riedl, *Adv. Energy Mater.* **2020**, *10*, 1903897.
- [187] G. Y. Margulis, M. G. Christoforo, D. Lam, Z. M. Beiley, A. R. Bowring, C. D. Bailie, A. Salleo, M. D. McGehee, *Adv. Energy Mater.* **2013**, *3*, 1657.
- [188] L. Sun, W. Zeng, C. Xie, L. Hu, X. Dong, F. Qin, W. Wang, T. Liu, X. Jiang, Y. Jiang, Y. Zhou, *Adv. Mater.* **2020**, *32*, 1907840.
- [189] J. Jiu, J. Wang, T. Sugahara, S. Nagao, M. Nogi, H. Koga, K. Suganuma, M. Hara, E. Nakazawa, H. Uchida, *RSC Adv.* **2015**, *5*, 27657.
- [190] W. Xiong, H. Liu, Y. Chen, M. Zheng, Y. Zhao, X. Kong, Y. Wang, X. Zhang, X. Kong, P. Wang, L. Jiang, *Adv. Mater.* **2016**, *28*, 7167.
- [191] H. Liu, Y. Li, J. Wu, Y. Fu, H. Tang, X. Yi, Z. Xie, *J. Mater. Chem. C* **2021**, *9*, 9914.
- [192] C.-H. Chung, T.-B. Song, B. Bob, R. Zhu, Y. Yang, *Nano Res.* **2012**, *5*, 805.
- [193] Y. Wang, Q. Chen, G. Zhang, C. Xiao, Y. Wei, W. Li, *ACS Appl. Mater. Interfaces* **2022**, *14*, 5699.
- [194] Y. Yang, B. Xu, J. Hou, *Chin. J. Chem.* **2021**, *39*, 2315.
- [195] W. Chen, R. Zhang, X. Yang, H. Wang, H. Yang, X. Hu, S. Zhang, *J. Mater. Chem. C* **2022**, *10*, 8625.
- [196] P. Wang, M. Jian, C. Zhang, M. Wu, X. Ling, J. Zhang, B. Wei, L. Yang, *Adv. Mater. Interfaces* **2022**, *9*, 2101442.
- [197] T. Sannicola, W. H. Chae, J. Mwaura, V. Bulović, J. C. Grossman, *ACS Appl. Energy Mater.* **2021**, *4*, 1431.
- [198] J. Wang, Z. Zhang, S. Wang, R. Zhang, Y. Guo, G. Cheng, Y. Gu, K. Liu, K. Chen, *Nano Energy* **2020**, *71*, 104638.
- [199] S. Ye, I. E. Stewart, Z. Chen, B. Li, A. R. Rathmell, B. J. Wiley, *Acc. Chem. Res.* **2016**, *49*, 442.
- [200] X. Hu, X. Meng, L. Zhang, Y. Zhang, Z. Cai, Z. Huang, M. Su, Y. Wang, M. Li, F. Li, X. Yao, F. Wang, W. Ma, Y. Chen, Y. Song, *Joule* **2019**, *3*, 2205.
- [201] N. Kim, H. Kang, J.-H. Lee, S. Kee, S. H. Lee, K. Lee, *Adv. Mater.* **2015**, *27*, 2317.
- [202] H. Kang, S. Jung, S. Jeong, G. Kim, K. Lee, *Nat. Commun.* **2015**, *6*, 6503.
- [203] S. Kim, E. Lee, Y. Lee, J. Kim, B. Park, S.-Y. Jang, S. Jeong, J. Oh, M. S. Lee, H. Kang, K. Lee, *ACS Appl. Mater. Interfaces* **2020**, *12*, 26232.
- [204] H. Park, J.-H. Lee, S. Lee, S. Y. Jeong, J. W. Choi, C.-L. Lee, J.-H. Kim, K. Lee, *ACS Appl. Mater. Interfaces* **2020**, *12*, 2276.
- [205] S. Kim, B. Sanyoto, W.-T. Park, S. Kim, S. Mandal, J.-C. Lim, Y.-Y. Noh, J.-H. Kim, *Adv. Mater.* **2016**, *28*, 10149.
- [206] G. Li, F. Wang, Q. Jiang, X. Gao, P. Shen, *Angew. Chem., Int. Ed.* **2010**, *49*, 3653.
- [207] Q. Li, J. Wu, Q. Tang, Z. Lan, P. Li, J. Lin, L. Fan, *Electrochem. Commun.* **2008**, *10*, 1299.
- [208] K.-H. Park, S. J. Kim, R. Gomes, A. Bhaumik, *Chem. Eng. J.* **2015**, *260*, 393.
- [209] H. Wang, Q. Feng, F. Gong, Y. Li, G. Zhou, Z.-S. Wang, *J. Mater. Chem. A* **2012**, *1*, 97.
- [210] Q. Tai, B. Chen, F. Guo, S. Xu, H. Hu, B. Sebo, X.-Z. Zhao, *ACS Nano* **2011**, *5*, 3795.
- [211] N. Kim, S. Kee, S. H. Lee, B. H. Lee, Y. H. Kahng, Y.-R. Jo, B.-J. Kim, K. Lee, *Adv. Mater.* **2014**, *26*, 2268.
- [212] T. Ohta, A. Bostwick, T. Seyller, K. Horn, E. Rotenberg, *Science* **2006**, *313*, 951.
- [213] X. Fu, L. Xu, J. Li, X. Sun, H. Peng, *Carbon* **2018**, *139*, 1063.
- [214] L. Yu, C. Shearer, J. Shapter, *Chem. Rev.* **2016**, *116*, 13413.
- [215] G. Jeong, D. Koo, J.-H. Woo, Y. Choi, E. Son, F. Huang, J.-Y. Kim, H. Park, *ACS Appl. Mater. Interfaces* **2022**, *14*, 33297.
- [216] T. Mahmoudi, Y. Wang, Y.-B. Hahn, *Nano Energy* **2018**, *47*, 51.
- [217] F. Lang, M. A. Gluba, S. Albrecht, J. Rappich, L. Korte, B. Rech, N. H. Nickel, *J. Phys. Chem. Lett.* **2015**, *6*, 2745.
- [218] Y. Song, S. Chang, S. Gradecak, J. Kong, *Adv. Energy Mater.* **2016**, *6*, 1600847.
- [219] Z. Liu, P. You, S. Liu, F. Yan, *ACS Nano* **2015**, *9*, 12026.
- [220] V.-D. Tran, S. V. N. Pammi, B.-J. Park, Y. Han, C. Jeon, S.-G. Yoon, *Nano Energy* **2019**, *65*, 104018.
- [221] P. You, Z. Liu, Q. Tai, S. Liu, F. Yan, *Adv. Mater.* **2015**, *27*, 3632.

- [222] L. Kuhn, N. E. Gorji, *Mater. Lett.* **2016**, *171*, 323.
- [223] H. Bi, F. Huang, J. Liang, X. Xie, M. Jiang, *Adv. Mater.* **2011**, *23*, 3202.
- [224] Z. Shi, A. H. Jayatissa, *Materials* **2018**, *11*, 36.
- [225] Y. Zhou, S. Tanaka, R. Azumi, *Appl. Surf. Sci.* **2020**, *515*, 146027.
- [226] L. Wieland, H. Li, C. Rust, J. Chen, B. S. Flavel, *Adv. Energy Mater.* **2021**, *11*, 2002880.
- [227] T. A. Shastry, M. C. Hersam, *Adv. Energy Mater.* **2017**, *7*, 1601205.
- [228] I. Jeon, C. Delacou, A. Kaskela, E. I. Kauppinen, S. Maruyama, Y. Matsuo, *Sci. Rep.* **2016**, *6*, 31348.
- [229] M. A. Contreras, T. Barnes, J. van de Lagemaat, G. Rumbles, T. J. Coutts, C. Weeks, P. Glatkowski, I. Levitsky, J. Peltola, D. A. Britz, *J. Phys. Chem. C* **2007**, *111*, 14045.
- [230] T. M. Barnes, X. Wu, J. Zhou, A. Duda, J. van de Lagemaat, T. J. Coutts, C. L. Weeks, D. A. Britz, P. Glatkowski, *Appl. Phys. Lett.* **2007**, *90*, 243503.
- [231] D. Kim, S. S. Shin, S. M. Lee, J.-S. Cho, J. H. Yun, H. S. Lee, J. H. Park, *Adv. Funct. Mater.* **2020**, *30*, 2001775.
- [232] M. J. Shin, J. H. Jo, A. Cho, J. Gwak, J. H. Yun, K. Kim, S. K. Ahn, J. H. Park, J. Yoo, I. Jeong, B.-H. Choi, J.-S. Cho, *Sol. Energy Mater. Sol. Cells* **2019**, *181*, 276.
- [233] D. Kim, S. S. Shin, Y. Jo, S. M. Lee, S. K. Ahn, J.-S. Cho, J. H. Yun, H. S. Lee, J. H. Park, *Adv. Sci.* **2022**, *9*, 2105436.
- [234] Z. Chen, Z. Wang, J. Wang, S. Chen, B. Zhang, Y. Li, L. Yuan, Y. Duan, *Nanomaterials* **2023**, *13*, 25.
- [235] X. Xu, H. Wang, J. Wang, M. Muhammad, Z. Wang, P. Chen, W. Zhao, B. Kang, J. Zhang, C. Li, Y. Duan, *ACS Appl. Energy Mater.* **2020**, *3*, 4208.
- [236] M. Filipič, P. Löper, B. Niesen, S. D. Wolf, J. Krč, C. Ballif, M. Topič, *Opt Express* **2015**, *23*, A263.
- [237] S.-W. Choi, J. Yang, J.-H. Park, S.-J. Han, P. Song, D.-W. Kang, J.-D. Kwon, *Curr. Appl. Phys.* **2019**, *19*, 1120.
- [238] J. W. Lim, G. Kim, M. Shin, S. J. Yun, *Sol. Energy Mater. Sol. Cells* **2017**, *163*, 164.
- [239] J. W. Lim, D. J. Lee, S. J. Yun, *ECS Solid State Lett.* **2013**, *2*, Q47.
- [240] A. Gupta, A. D. Compaan, *Appl. Phys. Lett.* **2004**, *85*, 684.
- [241] A. Abbas, D. M. Meysing, M. O. Reese, T. M. Barnes, J. M. Walls, C. A. Wolden, *Sol. Energy* **2018**, *159*, 940.
- [242] T. Ablekim, C. Perkins, X. Zheng, C. Reich, D. Swanson, E. Colegrove, J. N. Duenow, D. Albin, S. Nanayakkara, M. O. Reese, T. Shimpi, W. Sampath, W. K. Metzger, *IEEE J. Photovoltaics* **2019**, *9*, 888.
- [243] J. Li, D. R. Diercks, T. R. Ohno, C. W. Warren, M. C. Lonergan, J. D. Beach, C. A. Wolden, *Sol. Energy Mater. Sol. Cells* **2015**, *133*, 208.
- [244] M. J. Shin, S. Park, A. Lee, S. J. Park, A. Cho, K. Kim, S. K. Ahn, J. Hyung Park, J. Yoo, D. Shin, I. Jeong, J. H. Yun, J. Gwak, J.-S. Cho, *Appl. Surf. Sci.* **2021**, *535*, 147732.
- [245] P. Selvaraj, A. Ghosh, T. K. Mallick, S. Sundaram, *Renewable Energy* **2019**, *141*, 516.
- [246] Q. Hu, Y. Li, F. Huang, Z. Zhang, K. Ding, M. Wei, Z. Lin, *Sci. Rep.* **2015**, *5*, 11499.
- [247] N. Memarian, I. Concina, A. Braga, S. M. Rozati, A. Vomiero, G. Sberveglieri, *Angew. Chem.* **2011**, *123*, 12529.
- [248] X. Liu, R. Yuan, Y. Liu, S. Zhu, J. Lin, X. Chen, *New J. Chem.* **2016**, *40*, 6276.
- [249] A. Birkel, Y.-G. Lee, D. Koll, X. V. Meerbeek, S. Frank, M. J. Choi, Y. S. Kang, K. Char, W. Tremel, *Energy Environ. Sci.* **2012**, *5*, 5392.
- [250] H. Elbohy, K. M. Reza, S. Abdulkarim, Q. Qiao, *Sustainable Energy Fuels* **2018**, *2*, 403.
- [251] N. A. Karim, U. Mehmood, H. F. Zahid, T. Asif, *Sol. Energy* **2019**, *185*, 165.
- [252] I. Benesperi, H. Michaels, M. Freitag, *J. Mater. Chem. C* **2018**, *6*, 11903.
- [253] B.-H. Jiang, H.-E. Lee, J.-H. Lu, T.-H. Tsai, T.-S. Shieh, R.-J. Jeng, C.-P. Chen, *ACS Appl. Mater. Interfaces* **2020**, *12*, 39496.
- [254] Y. Li, C. Ji, Y. Qu, X. Huang, S. Hou, C.-Z. Li, L.-S. Liao, L. J. Guo, S. R. Forrest, *Adv. Mater.* **2019**, *31*, 1903173.
- [255] B. Jia, S. Dai, Z. Ke, C. Yan, W. Ma, X. Zhan, *Chem. Mater.* **2018**, *30*, 239.
- [256] Y.-W. Zhang, P.-P. Cheng, W.-Y. Tan, Y. Min, *Appl. Surf. Sci.* **2021**, *537*, 147908.
- [257] J. C. Yu, J. Sun, N. Chandrasekaran, C. J. Dunn, A. S. R. Chesman, J. J. Jasieniak, *Nano Energy* **2020**, *71*, 104635.
- [258] M. Xie, H. Lu, L. Zhang, J. Wang, Q. Luo, J. Lin, L. Ba, H. Liu, W. Shen, L. Shi, C.-Q. Ma, *Sol. RRL* **2018**, *2*, 1700184.
- [259] J. Zhao, K. O. Brinkmann, T. Hu, N. Pourdavoud, T. Becker, T. Gahlmann, R. Heiderhoff, A. Polywka, P. Görrn, Y. Chen, B. Cheng, T. Riedl, *Adv. Energy Mater.* **2017**, *7*, 1602599.
- [260] G. Yang, H. Tao, P. Qin, W. Ke, G. Fang, *J. Mater. Chem. A* **2016**, *4*, 3970.
- [261] Z. H. Bakr, Q. Wali, A. Fakhruddin, L. Schmidt-Mende, T. M. Brown, R. Jose, *Nano Energy* **2017**, *34*, 271.
- [262] C. Xu, P. Cai, X. Zhang, Z. Zhang, X. Xue, J. Xiong, J. Zhang, *Sol. Energy Mater. Sol. Cells* **2017**, *159*, 136.
- [263] J. J. Jasieniak, J. Seifert, J. Jo, T. Mates, A. J. Heeger, *Adv. Funct. Mater.* **2012**, *22*, 2594.
- [264] Z. Tan, W. Zhang, C. Cui, Y. Ding, D. Qian, Q. Xu, L. Li, S. Li, Y. Li, *Phys. Chem. Chem. Phys.* **2012**, *14*, 14589.
- [265] Z. Tan, L. Li, C. Cui, Y. Ding, Q. Xu, S. Li, D. Qian, Y. Li, *J. Phys. Chem. C* **2012**, *116*, 18626.
- [266] C. Albonetti, V. El Qacemi, S. Limage, C. Versini, L.-D. Kauffmann, M. Muccini, M. Seri, *Phys. Status Solidi A* **2021**, *218*, 2000748.
- [267] D. Ouyang, J. Zheng, Z. Huang, L. Zhu, W. C. H. Choy, *J. Mater. Chem. A* **2021**, *9*, 371.
- [268] C. Bronnbauer, N. Gasparini, C. J. Brabec, K. Forberich, *Adv. Opt. Mater.* **2016**, *4*, 1098.
- [269] H. Yu, J. Wang, Q. Zhou, J. Qin, Y. Wang, X. Lu, P. Cheng, *Chem. Soc. Rev.* **2023**, *52*, 4132.
- [270] L. Xiao, G. Huang, H. Zhang, X. Zhang, Y. Li, S. Li, T. Jiang, B. Han, Y. Zhang, H. Zhou, *Sol. RRL* **2022**, *6*, 2100818.
- [271] P. Lova, G. Manfredi, D. Comoretto, *Adv. Opt. Mater.* **2018**, *6*, 1800730.
- [272] Y. Zhang, Z. Peng, C. Cai, Z. Liu, Y. Lin, W. Zheng, J. Yang, L. Hou, Y. Cao, *J. Mater. Chem. A* **2016**, *4*, 11821.
- [273] K. Khandelwal, S. Biswas, A. Mishra, G. D. Sharma, *J. Mater. Chem. C* **2021**, *10*, 13.
- [274] X. Li, R. Xia, K. Yan, H.-L. Yip, H. Chen, C.-Z. Li, *Chin. Chem. Lett.* **2020**, *31*, 1608.
- [275] *Photonic Crystals: Molding the Flow of Light* (Eds: J. D. Joannopoulos), Princeton University Press, Princeton, NJ **2008**.
- [276] C. Ji, D. Liu, C. Zhang, L. J. Guo, *Nat. Commun.* **2020**, *11*, 3367.
- [277] K. Zilberberg, T. Riedl, *J. Mater. Chem. A* **2016**, *4*, 14481.
- [278] Ç. Çetinkaya, E. Çokduygulular, B. Kinacı, F. Güzelçimen, Y. Özen, H. İ. Efker, İ. Candan, S. Emik, S. Özçelik, *Sci. Rep.* **2021**, *11*, 13079.
- [279] Y. Li, X. Huang, H. K. M. Sheriff, S. R. Forrest, *Nat. Rev. Mater.* **2023**, *8*, 186.
- [280] C. He, J. Wang, S. Chen, Y. Zhou, N. Jiang, J. Zhang, Y. Duan, *Sol. RRL* **2023**, *7*, 2300126.
- [281] J. Zhong, W. Liang, Y. Long, *Optik* **2018**, *171*, 706.
- [282] Y. Long, *Sol. Energy Mater. Sol. Cells* **2011**, *95*, 3400.
- [283] C.-C. Chueh, M. Crump, A. K.-Y. Jen, *Adv. Funct. Mater.* **2016**, *26*, 321.
- [284] D. Han, S. Han, Z. Bu, Y. Deng, C. Liu, W. Guo, *Sol. RRL* **2022**, *6*, 2200441.
- [285] H. Tang, Y. Li, H. Liu, J. Wu, L. Chen, Y. Fu, Z. Xie, *J. Mater. Chem. C* **2022**, *10*, 3720.
- [286] J. Meiss, F. Holzmueller, R. Gresser, K. Leo, M. Riede, *Appl. Phys. Lett.* **2011**, *99*, 193307.
- [287] J. Meiss, T. Menke, K. Leo, C. Urrich, W.-M. Gnehr, S. Sonntag, M. Pfeiffer, M. Riede, *Appl. Phys. Lett.* **2011**, *99*, 043301.

- [288] X. Huang, D. Fan, S. R. Forrest, *Org. Electron.* **2021**, *97*, 106276.
- [289] H. Li, Y. Hu, H. Wang, Q. Tao, Y. Zhu, Y. Yang, *Sol. RRL* **2021**, *5*, 2000524.
- [290] S. Saylan, T. Milakovich, S. A. Hadi, A. Nayfeh, E. A. Fitzgerald, M. S. Dahlem, *Sol. Energy* **2015**, *122*, 76.
- [291] H. A. Macleod, *Thin-Film Optical Filters*, Institute Of Physics Pub, Bristol, PA **2001**.
- [292] F. Pastorelli, P. Romero-Gomez, R. Betancur, A. Martinez-Otero, P. Mantilla-Perez, N. Bonod, J. Martorell, *Adv. Energy Mater.* **2015**, *5*, 1400614.
- [293] G. F. Burkhard, E. T. Hoke, M. D. McGehee, *Adv. Mater.* **2010**, *22*, 3293.
- [294] L. Wen, Q. Chen, F. Sun, S. Song, L. Jin, Y. Yu, *Sci. Rep.* **2014**, *4*, 7036.
- [295] D.-Y. Shin, J. R. Lim, W.-G. Shin, C.-G. Lee, G.-H. Kang, *Sol. Energy Mater. Sol. Cells* **2021**, *221*, 110903.
- [296] A. Fakhruddin, R. Jose, T. M. Brown, F. Fabregat-Santiago, J. Bisquert, *Energy Environ. Sci.* **2014**, *7*, 3952.
- [297] M. Powalla, S. Paetel, E. Ahlswede, R. Wuerz, C. D. Wessendorf, T. Magorian Friedlmeier, *Appl. Phys. Rev.* **2018**, *5*, 041602.
- [298] D. Li, D. Zhang, K.-S. Lim, Y. Hu, Y. Rong, A. Mei, N.-G. Park, H. Han, *Adv. Funct. Mater.* **2021**, *31*, 2008621.
- [299] M. A. Green, E. D. Dunlop, J. Hohl-Ebinger, M. Yoshita, N. Kopidakis, K. Bothe, D. Hinken, M. Rauer, X. Hao, *Prog. Photovoltaics* **2022**, *30*, 687.
- [300] Y. Galagan, E. W. C. Coenen, W. J. H. Verhees, R. Andriessen, *J. Mater. Chem. A* **2016**, *4*, 5700.
- [301] A. Distler, C. J. Brabec, H.-J. Egelhaaf, *Prog. Photovoltaics* **2021**, *29*, 24.
- [302] Y. Deng, C. H. Van Brackle, X. Dai, J. Zhao, B. Chen, J. Huang, *Sci. Adv.* **2019**, *5*, eaax7537.
- [303] J.-Y. Fan, Z.-X. Liu, J. Rao, K. Yan, Z. Chen, Y. Ran, B. Yan, J. Yao, G. Lu, H. Zhu, C.-Z. Li, H. Chen, *Adv. Mater.* **2022**, *34*, 2110569.
- [304] S. Park, S. H. Park, H. Jin, S. Yoon, H. Ahn, S. Shin, K. Kwak, S. Nah, E.-Y. Shin, J. H. Noh, B. K. Min, H. J. Son, *Nano Energy* **2022**, *98*, 107187.
- [305] H. Chen, R. Zhang, X. Chen, G. Zeng, L. Kobera, S. Abbrent, B. Zhang, W. Chen, G. Xu, J. Oh, S.-H. Kang, S. Chen, C. Yang, J. Brus, J. Hou, F. Gao, Y. Li, Y. Li, *Nat. Energy* **2021**, *6*, 1045.
- [306] Z. Jia, Z. Chen, X. Chen, J. Yao, B. Yan, R. Sheng, H. Zhu, Y. (Michael) Yang, *Photon. Res., PRJ* **2021**, *9*, 324.
- [307] S. Yeop Myong, S. Won Jeon, *Sol. Energy Mater. Sol. Cells* **2015**, *143*, 442.
- [308] C. A. Gonzalez-Flores, D. Pourjafari, R. Escalante, E. J. Canto-Aguilar, A. V. Poot, J. M. Andres Castán, Y. Kervella, R. Demadrille, A. J. Riquelme, J. A. Anta, G. Oskam, *ACS Appl. Energy Mater.* **2022**, *5*, 14092.
- [309] Y. W. Han, H. S. Lee, D. K. Moon, *ACS Appl. Mater. Interfaces* **2021**, *13*, 19085.
- [310] D. Wang, Y. Li, G. Zhou, E. Gu, R. Xia, B. Yan, J. Yao, H. Zhu, X. Lu, H.-L. Yip, H. Chen, C.-Z. Li, *Energy Environ. Sci.* **2022**, *15*, 2629.
- [311] L. Vesce, P. Mariani, M. Calamante, A. Dessì, A. Mordini, L. Zani, A. Di Carlo, *Sol. RRL* **2022**, *6*, 2200403.
- [312] F. M. van der Staaij, I. M. van Keulen, E. von Hauff, *Sol. RRL* **2021**, *5*, 2100167.
- [313] Z. Xiong, T. M. Walsh, A. G. Aberle, *Energy Procedia* **2011**, *8*, 384.
- [314] N. Li, X. Niu, Q. Chen, H. Zhou, *Chem. Soc. Rev.* **2020**, *49*, 8235.
- [315] P. Holzhey, M. Saliba, *J. Mater. Chem. A* **2018**, *6*, 21794.
- [316] Onyx Solar—Photovoltaic Glass for Buildings, <https://www.onyx-solar.com/> (accessed: May 2021).
- [317] D. L. Staebler, C. R. Wronski, *Appl. Phys. Lett.* **1977**, *31*, 292.
- [318] H. Sai, T. Matsui, T. Koida, K. Matsubara, M. Kondo, S. Sugiyama, H. Katayama, Y. Takeuchi, I. Yoshida, *Appl. Phys. Lett.* **2015**, *106*, 213902.
- [319] J. Ramanujam, D. M. Bishop, T. K. Todorov, O. Gunawan, J. Rath, R. Nekovei, E. Artegiani, A. Romeo, *Prog. Mater. Sci.* **2020**, *110*, 100619.
- [320] H. Yuan, W. Wang, D. Xu, Q. Xu, J. Xie, X. Chen, T. Zhang, C. Xiong, Y. He, Y. Zhang, Y. Liu, H. Shen, *Sol. Energy* **2018**, *165*, 233.
- [321] L. Peedikakkandy, J. Naduvath, S. Mallick, P. Bhargava, *Mater. Res. Bull.* **2018**, *108*, 113.
- [322] H. Sakamoto, S. Igarashi, M. Uchida, K. Niume, M. Nagai, *Org. Electron.* **2012**, *13*, 514.
- [323] E. Muchuweni, B. S. Martincigh, V. O. Nyamori, *RSC Adv.* **2020**, *10*, 44453.
- [324] Q. He, T. Qian, J. Zai, Q. Qiao, S. Huang, Y. Li, M. Wang, *J. Mater. Chem. A* **2015**, *3*, 20359.
- [325] Q. He, S. Huang, J. Zai, N. Tang, B. Li, Q. Qiao, X. Qian, *Chemistry* **2015**, *21*, 15153.
- [326] D. Devadiga, M. Selvakumar, P. Shetty, M. S. Santosh, *J. Power Sources* **2021**, *493*, 229698.
- [327] H.-C. Kwon, A. Kim, H. Lee, D. Lee, S. Jeong, J. Moon, *Adv. Energy Mater.* **2016**, *6*, 1601055.
- [328] Y. Wu, H. Yang, Y. Zou, Y. Dong, J. Yuan, C. Cui, Y. Li, *Energy Environ. Sci.* **2019**, *12*, 675.
- [329] Y. Zhao, W. Zhou, Z. Han, D. Yu, Q. Zhao, *Phys. Chem. Chem. Phys.* **2021**, *23*, 94.
- [330] L. Xie, P. Song, L. Shen, J. Lu, K. Liu, K. Lin, W. Feng, C. Tian, Z. Wei, *J. Mater. Chem. A* **2020**, *8*, 7653.
- [331] Z. Qiu, N. Li, Z. Huang, Q. Chen, H. Zhou, *Small Methods* **2020**, *4*, 1900877.
- [332] J. Wang, Z. Wang, S. Chen, N. Jiang, L. Yuan, J. Zhang, Y. Duan, *Adv. Mater. Interfaces* **2023**, *10*, 2202266.
- [333] M. Li, H. Li, J. Fu, T. Liang, W. Ma, *J. Phys. Chem. C* **2020**, *124*, 27251.
- [334] W. Xiang, Z. Wang, D. J. Kubicki, W. Tress, J. Luo, D. Prochowicz, S. Akin, L. Emsley, J. Zhou, G. Dietler, M. Grätzel, A. Hagfeldt, *Joule* **2019**, *3*, 205.
- [335] Q. Wali, F. J. Iftikhar, M. E. Khan, A. Ullah, Y. Iqbal, R. Jose, *Org. Electron.* **2020**, *78*, 105590.
- [336] J. Chen, W. C. H. Choy, *Sol. RRL* **2020**, *4*, 2000408.
- [337] T. Wang, J. Yang, Q. Cao, X. Pu, Y. Li, H. Chen, J. Zhao, Y. Zhang, X. Chen, X. Li, *Nat. Commun.* **2023**, *14*, 1342.
- [338] C. C. Boyd, R. Cheacharoen, T. Leijtens, M. D. McGehee, *Chem. Rev.* **2019**, *119*, 3418.
- [339] Z. Wang, J. Wang, Z. Li, Z. Chen, L. Shangguan, S. Fan, Y. Duan, *Nano Energy* **2023**, *109*, 108232.
- [340] S. Ma, G. Yuan, Y. Zhang, N. Yang, Y. Li, Q. Chen, *Energy Environ. Sci.* **2022**, *15*, 13.
- [341] M. Günther, D. Blätte, A. L. Oechsle, S. S. Rivas, A. A. Yousefi Amin, P. Müller-Buschbaum, T. Bein, T. Ameri, *ACS Appl. Mater. Interfaces* **2021**, *13*, 19072.
- [342] K. Wang, Y. Li, Y. Li, *Macromol. Rapid Commun.* **2020**, *41*, 1900437.
- [343] J. Xiao, M. Ren, G. Zhang, J. Wang, D. Zhang, L. Liu, N. Li, C. J. Brabec, H.-L. Yip, Y. Cao, *Sol. RRL* **2019**, *3*, 1900077.
- [344] Q. Burlingame, X. Huang, X. Liu, C. Jeong, C. Coburn, S. R. Forrest, *Nature* **2019**, *573*, 394.
- [345] D. Hu, Q. Yang, H. Chen, F. Wobben, V. M. L. Corre, R. Singh, T. Liu, R. Ma, H. Tang, L. J. A. Koster, T. Duan, H. Yan, Z. Kan, Z. Xiao, S. Lu, *Energy Environ. Sci.* **2020**, *13*, 2134.
- [346] X. Xu, J. Xiao, G. Zhang, L. Wei, X. Jiao, H.-L. Yip, Y. Cao, *Sci. Bull.* **2020**, *65*, 208.
- [347] Z. Song, C. L. McElvany, A. B. Phillips, I. Celik, P. W. Krantz, S. C. Watthage, G. K. Liyanage, D. Apul, M. J. Heben, *Energy Environ. Sci.* **2017**, *10*, 1297.
- [348] B. Smith, M. Woodhouse, K. Horowitz, T. Silverman, J. Zuboy, R. Margolis, *Photovoltaic (PV) Module Technologies: 2020 Benchmark Costs and Technology Evolution Framework Results*, United States **2021**.

- [349] Z. Song, A. B. Phillips, I. Celik, G. K. Liyanage, D. Zhao, D. Apul, Y. Yan, M. J. Heben, in *2018 IEEE 7th World Conf. on Photovoltaic Energy Conversion (WCPEC) (A Joint Conf. of 45th IEEE PVSC, 28th PVSEC & 34th EU PVSEC)*, IEEE, Piscataway **2018**, pp. 1134–1138.
- [350] L. Meng, J. You, Y. Yang, *Nat. Commun.* **2018**, *9*, 5265.
- [351] I. Mathews, S. N. Kantareddy, T. Buonassisi, I. M. Peters, *Joule* **2019**, *3*, 1415.
- [352] C. J. Mulligan, M. Wilson, G. Bryant, B. Vaughan, X. Zhou, W. J. Belcher, P. C. Dastoor, *Sol. Energy Mater. Sol. Cells* **2014**, *120*, 9.
- [353] M. D. Bastiani, V. Larini, R. Montecucco, G. Grancini, *Energy Environ. Sci.* **2023**, *16*, 421.
- [354] Y. Cheng, Y. Peng, A. K.-Y. Jen, H.-L. Yip, *Sol. RRL* **2022**, *6*, 2100545.
- [355] R. Xue, J. Zhang, Y. Li, Y. Li, *Small* **2018**, *14*, 1801793.
- [356] L. Gao, G. Yang, *Sol. RRL* **2020**, *4*, 1900200.
- [357] J. Guo, J. Min, *Adv. Energy Mater.* **2019**, *9*, 1802521.
- [358] H. Liu, M.-H. Yu, C.-C. Lee, X. Yu, Y. Li, Z. Zhu, C.-C. Chueh, Z. Li, A. K.-Y. Jen, *Adv. Mater. Technol.* **2021**, *6*, 2000960.
- [359] B. Azzopardi, C. J. M. Emmott, A. Urbina, F. C. Krebs, J. Mutale, J. Nelson, *Energy Environ. Sci.* **2011**, *4*, 3741.
- [360] P. Čulík, K. Brooks, C. Momblona, M. Adams, S. Kinge, F. Maréchal, P. J. Dyson, M. K. Nazeeruddin, *ACS Energy Lett.* **2022**, *7*, 3039.
- [361] T. H. Syed, W. Wei, *Inorganics* **2022**, *10*, 191.
- [362] H. Sai, T. Matsui, K. Matsubara, *Appl. Phys. Lett.* **2016**, *109*, 183506.
- [363] D. C. Jordan, S. R. Kurtz, *Prog. Photovoltaics* **2013**, *21*, 12.
- [364] M. Saliba, M. Stollerfoht, C. M. Wolff, D. Neher, A. Abate, *Joule* **2018**, *2*, 1019.
- [365] S. A. Gevorgyan, N. Espinosa, L. Ciammaruchi, B. Roth, F. Livi, S. Tsopanidis, S. Züfle, S. Queirós, A. Gregori, G. A. dos R. Benatto, M. Corazza, M. V. Madsen, M. Hösel, M. J. Beliatas, T. T. Larsen-Olsen, F. Pastorelli, A. Castro, A. Mingorance, V. Lenzi, D. Fluhr, R. Roesch, M. Maria Duarte Ramos, A. Savva, H. Hoppe, L. S. A. Marques, I. Burgués, E. Georgiou, L. Serrano-Luján, F. C. Krebs, *Adv. Energy Mater.* **2016**, *6*, 1600910.
- [366] A. Tiitonen, K. Miettunen, J. Halme, S. Lepikko, A. Poskela, P. D. Lund, *Energy Environ. Sci.* **2018**, *11*, 730.
- [367] M. Mrinalini, N. Islavath, S. Prasanthkumar, L. Giribabu, *Chem. Rec.* **2019**, *19*, 661.
- [368] T. Kato, *Jpn. J. Appl. Phys.* **2017**, *56*, 04CA02.
- [369] I. Burgués-Ceballos, L. Lucera, P. Tiwana, K. Ocytko, L. W. Tan, S. Kowalski, J. Snow, A. Pron, H. Bückstümmer, N. Blouin, G. Morse, *Joule* **2021**, *5*, 2261.
- [370] G. Bernardo, T. Lopes, D. G. Lidzey, A. Mendes, *Adv. Energy Mater.* **2021**, *11*, 2100342.
- [371] S. V. Subramaniam, D. Kutsarov, T. Sauermann, S. B. Meier, *Energy Technol.* **2020**, *8*, 2000234.
- [372] Y. Gao, F. T. Si, O. Isabella, R. Santbergen, G. Yang, J. Dong, G. Zhang, M. Zeman, in *2017 IEEE 44th Photovoltaic Specialist Conf. (PVSC)*, IEEE, Piscataway, NJ **2017**, pp. 2605–2609.
- [373] Q. Xue, Y. Bai, M. Liu, R. Xia, Z. Hu, Z. Chen, X.-F. Jiang, F. Huang, S. Yang, Y. Matsuo, H.-L. Yip, Y. Cao, *Adv. Energy Mater.* **2017**, *7*, 1602333.
- [374] Y. Meng, X. Li, S. Wang, C. Lau, H. Hu, Y. Ke, G. Tan, J. Yang, Y. Long, *Nano Energy* **2022**, *91*, 106632.
- [375] Z. Hu, Z. Wang, Q. An, F. Zhang, *Sci. Bull.* **2020**, *65*, 131.
- [376] J. Jing, S. Dong, K. Zhang, Z. Zhou, Q. Xue, Y. Song, Z. Du, M. Ren, F. Huang, *Adv. Energy Mater.* **2022**, *12*, 2200453.



Pankaj Kumar received his Bachelor–Master in Technology (dual) degree in Materials Science and Engineering from Indian Institute of Technology Kanpur (India) and Master of Applied Science degree in Chemical Engineering from University of Waterloo (Canada). Currently, he is pursuing doctoral degree in Experimental Physics under the supervision of Prof. Alberto Vomiero and Dr. Shujie You at Luleå University of Technology (Sweden). His research focuses on the development of emerging thin-film (semitransparent) photovoltaics.



Shujie You is a senior lecturer in Experimental Physics at Luleå University of Technology. Her work focuses on optical characterization of nano materials and their application in renewable energy system. Expertise includes X-ray diffraction, Raman and photoluminescence spectroscopy, high pressure diamond anvil cells (DACs), carbon nanomaterials, and metal oxide structures.



Alberto Vomiero is a chair professor of Experimental Physics at the Department of Engineering Sciences and Mathematics, Luleå University of Technology, Sweden and a professor of Industrial Engineering at the Department of Molecular Sciences and Nanosystems, Ca' Foscari University of Venice, Italy. He is leading a multidisciplinary group focusing on the development of advanced nanomaterials for energy and environmental applications, including solar cells, water splitting, and photocatalysis. He is a former Marie Curie International Outgoing Fellow of the European Commission, Fellow of the Swedish Foundations, of the Royal Society of Chemistry, and several other societies.